WARSAW UNIVERSITY OF TECHNOLOGY

Faculty of Physics

Ph.D. THESIS

Marcin Patecki, M.Sc. Eng.

Optimisation analysis and improvement of the effective beam sizes in Accelerator Test Facility 2

Supervisors
Professor Adam Kisiel, Ph.D.
Rogelio Tomàs, Ph.D.

Warsaw, 2016

Acknowledgements

Bringing my PhD project to a successful end would not have been possible without help of people who supported me over the last three years. I would like to take this occasion to express my gratitude.

Firstly, I would like to express my special appreciation to Rogelio Tomás, my supervisor at CERN. His very special way of supervision motivated me for a continuous effort and his trust helped me in becoming so much independent in my research.

My sincere thanks also go to Adam Kisiel, my supervisor at the at Warsaw University of Technology. After supervising my engineer's and master's theses, he helped me a lot in completing this thesis and removing any obstacles from my way.

Working with the real accelerator at the Accelerator Test Facility in Japan was a great adventure that I will always remember. I would like to thank the ATF and KEK staff for their hospitality. Special thanks go to Toshiyuki Okugi who taught me so much about the beam dynamics and machine operation.

I thank my colleagues from different labs who not only taught me a lot but also shared with me many unforgettable experiences. Many thanks to Doug, Edu, Fabien, Hector, Juergen, Neven, Nuria, Oscar and Talitha.

Most importantly I would like to express my deep thankfulness to my beloved wife for her endless support, infinite encouragement and for believing in me all this time.

Streszczenie

Liniowy zderzacz leptonów jest uznawany za odpowiednie narzędzie do precyzyjnego badania fizyki cząstek i oddziaływań elementarnych przy energiach rzędu TeV. Największą szansę realizacji ma jeden z dwóch istniejących projektów liniowego zderzacza e^+e^-: Compact Linear Collider (CLIC) oraz International Linear Collider (ILC). Oba projekty, rozwijane przez współpracujące ze sobą międzynarodowe kolaboracje, spełniają wymagania środowisk naukowych.

Przy energiach rzędu TeV przekrój czynny wielu interesujących procesów jest mały, w związku z czym świetlność wiązki (luminosity) w punkcie interakcji (IP) musi być odpowiednio duża, żeby dostarczyć wystarczającą liczbę zderzeń (rzędu 10^{34} $\mathrm{cm}^{-2}\mathrm{s}^{-1}$). Świetlność wiązki jest odwrotnie proporcjonalna do jej poprzecznych rozmiarów, zatem osiągnięcie wymaganej świetlności wymaga skupienia wiązki do rozmiarów rzędu nm w IP. Skupianie wiązek odbywa się w ostatnim fragmencie zderzacza przed punktem interakcji (final focus system, FFS) przy użyciu magnetycznych soczewek kwadrupolowych. Efekty chromatyczne związane z niejednorodnością w pędzie cząstek i silnym polem skupiającym powodują zwrost rozmiaru wiązki w punkcie zderzenia.

Lokalna korekcja efektów chromatycznych w miejscu ich wzbudzania została zaproponowana w 2001 roku przez P. Raimondi i A. Seryi i po raz pierwszy zastosowana w akceleratorze badawczym Accelerator Test Facility 2 (ATF2) w laboratorium KEK w Japonii służącym do badania transportu wiązki elektronów do punktu zderzenia. Skuteczność tego rozwiązania została potwierdzona poprzez zmierzenie rozmiaru wiązki blisko 40 nm w IP – o rząd wielkości mniej niż w przypadku gdy aberracje chromatyczne nie są skorygowane. W związku z tym lokalna korekcja efektów chromatycznych została wybrana do zastosowania w przypadku ILC oraz jest rozważana jako jedna z możliwości w przypadku CLIC, gdzie aberracje chromatyczne są szacowane na około pięciokrotnie silniejsze niż w ILC.

Siłę skupienia wiązki opisuje wartość funkcji optycznej β w punkcie zderzenia (β^*). W liniowym przybliżeniu poprzeczny rozmiar wiązki w IP jest proporconalny do pierwiastka z β^* ($\sigma^* \propto \sqrt{\beta^*}$), a siła efektów chromatycznych jest odwrotnie proporcjonalna do β^* ($\zeta \propto \frac{1}{\beta^*}$). W związku z tym zmiejszenie β^* w ATF2 pozwoli zmniejszyć rozmiar wiązki w punkcie zderzenia oraz zwiększyć siłę aberracji chromatycznych. Głównym celem badań opisanych w tej pracy jest zmiejszenie wartości β^* w ATF2 w celu zbadania optyki o wyższym poziomie efektów chromatycznych (bliskich CLIC) oraz identyfikacji potencjalnych przeszkód w zmniejszeniu rozmiaru wiązki. Zrozumienie zależności pomiędzy mniejszą wartością β^* a rosnącymi aberracjami transportu wiązki ma kluczowe znaczenie dla rozważanych zderzaczów liniowych.

Po przypomnieniu Modelu Standardowego, w pierwszym rozdziale opisane zostały również główne różnice pomiędzy zderzaczem liniowym a kołowym oraz podsumowanie potencjału naukowego zderzaczy liniowych.

Zderzacze liniowe zostały szczegółowo opisane w rozdziale drugim, który rozpoczyna się przeglądem podstawowych narzędzi liniowej i nieliniowej dynamiki wiązki. Następnie opisane są poszczególne podzespoły zderzacza ze szczególnym wyróżnieniem FFS. Rozdział kończy się porównaniem CLIC i ILC oraz krótkim opisem liniowych akceleratorów badawczych.

Accelerator Test Facility 2, w którym przeprowadzono część eksperymentalną raportowanych badań, został szczegółowo opisany w rozdziale trzecim.

Badanie wykonalności zmniejszenia wartości β^* w ATF2 przedstawione zostało w rozdziale czwartym. Dotyczą one optymalizacji rozmiaru wiązki w IP, wpływu tzw. fringe fields kwadrupoli magnetycznych na rozmiar wiązki w IP oraz zależności aberracji optycznych na rozmiar wiązki w IP w funkcji jej intensywności. Opisane zostały również opracowane narzędzia komputerowe do symulacji procesu strojenia maszyny uwzględniając jej rzeczywiste niedoskonałości.

W rozdziale piątym opisane są wyniki badań eksperymentalnych dotyczących wdrożenia nowej optyki wiązki w ATF2 z wartością β_y^* pomniejszoną o połowę. Przygotowanie i wykonanie badań wymagało 23 tygodni pracy z akceleratorem ATF2, rozłożone na 11 pobytów w Japonii. Opracowana została nowa metoda implementacji i kontroli optyki wiązki oparta na dokładnych pomiarach rozmiaru wiązki w IP i precyzyjnej kontroli położenia ogniska wiązki. Przeprowadzone zostały dwa pełne cykle strojenia maszyny zakończone pomiarem rozmiarów wiązki w IP. Zmierzone rozmiary wiązki okazały się trzykrotnie większe niż oczekiwano. Dla porównania, dla standardowej optyki osiąga się rozmiary wiązki zgodne z projektem, co sugeruje że niedoskonałości maszyny mają większy wpływ na rozmiar wiązki dla zmiejszonych wartości β_y^* niż oczekiwano. Komputerowe symulacje strojenia maszyny uwzględniające realistyczne niedoskonałości akceleratora prowadzą do uzyskania mniejszych rozmiarów wiązki w IP niż zmierzone w eksperymencie. Pokrycie wyników eksperymentu z symulacjami uzyskuje się dopiero po zwiększeniu poziomu niedoskonałości maszyny. Symulacje również wskazują, że bardziej efektywna korekcja orbity wiązki pozwala osiągnąć mniejsze rozmiary wiązki w IP. Zidentyfikowano następujące czynniki wpływające na zwiększenie rozmiaru wiązki: niewystarczająca kontrola nad orbitą wiązki i jej wrażliwość na fluktuacje stanu maszyny, udział tzw. wakefields w połączeniu z fluktuacjami orbity wiązki, silniejsze składowe multipolowe magnesów, większe błędy pozycjonowania elementów maszyny oraz błedy i niestabilności urządzeń diagnostycznych. Poprawienie tych elementów może mieć kluczowe znaczenie dla skutecznego wdrożenia optyki o niskich wartościach β_y^* w ATF2.

Abstract

A lepton linear collider is considered by the accelerator and particle physics communities as an appropriate machine to perform high precision particle physics research in the TeV energy regime. There are two proposals for the future e^+e^- linear collider: the Compact Linear Collider (CLIC) and the International Linear Collider (ILC), both developed by two wide international collaborations with strong overlap between them. Both designs satisfy the particle physics requirements.

At the TeV energy regime the cross sections of many processes of interest are small, therefore large luminosities on the order of 10^{34} cm^{-2}s^{-1} at the interaction point (IP) are required to deliver the required event rates. The luminosity inversely depends on the transverse size of the colliding beams which restricts the beam sizes at the IP to the nanometer level. The strong focusing of the beams occurs in the final focus system (FFS), the most inner part of a linear collider, where the beams are focused at the IP by means of two strong quadrupole magnets called the final doublet (FD). The efficiency of the beam focusing is deteriorated by the chromatic effects of the FD quadrupoles meaning that off-momentum particles are not exactly focused at the focal point, leading to larger spot sizes at the IP.

A novel design of the final focus system with a local compensation of the chromatic effects has been proposed in 2001 by P. Raimondi and A. Seryi. This design is being tested in the KEK Accelerator Test Facility 2 (ATF2) in Japan, a scaled down implementation of the linear collider beam delivery system. It has already been demonstrated that the IP vertical beam size in ATF2 decreases from some hundreds of nanometers to about 40 nm when the chromaticity is corrected. Therefore, the local chromaticity correction scheme is considered as a baseline for the ILC and a strong candidate for CLIC. However, for CLIC the expected level of chromaticity is higher by about a factor 5.

The parameter describing the focusing strength is the IP value of the optical β function (β^*). In linear approximation, the IP beam size is proportional to the square root of the β^* value ($\sigma^* \propto \sqrt{\beta^*}$) and chromaticity is inversely proportional to the β^* value ($\zeta \propto \frac{1}{\beta^*}$). Therefore, decreasing the β^* value in ATF2 allows to reduce the IP beam size and to increase the level of chromaticity. The main objective of the study described in this thesis is to decrease the β^* value in the ATF2 in order to investigate the performance of more chromatic optics (close to the level of CLIC) and to study the limits of beam focusing at the IP. Understanding the trade-offs between lowering β^* and increasing aberrations is of critical importance for future linear colliders.

In Chapter 1, after a reminder of the Standard Model of elementary particles, the main differences of linear colliders with respect to circular colliders are discussed. The physics potential of linear colliders is also summarized.

Linear colliders are discussed in more detail in Chapter 2. The most important tools of the linear and nonlinear beam dynamics are described first. Afterwards, the linear collider layout is presented with a special emphasis given to the final focus system. Finally, the two existing designs for a future linear collider are described, together with the test facilities.

The Accelerator Test Facility serving for performing the experimental studies of this thesis is described in detail in Chapter 3.

The feasibility studies of the low β_y^* optics in the ATF2 are presented in Chapter 4. The results of the nonlinear beamline optimisation for minimising the IP beam size are presented in the first section of this chapter. The impact of the quadrupole fringe fields on CLIC, the ILC and three lattices of the ATF2 are described in the second section. In the third section the contribution of optical aberrations to spot size increase with bunch intensity is investigated. Finally, the developed computer tools for performing the tuning simulations are described in the last section of this chapter.

The experimental studies of the new ATF2 optics with the β_y^* value decreased by a factor 2 are described in Chapter 5. Completing this research required 11 visits in the High Energy Accelerator Research Organization (KEK) in Japan and spending 23 weeks working with the ATF2 accelerator. The optics control and implementation was achieved by introducing a new method of beam diagnostics at the IP based on precise beam size measurements and fine, well-controlled changes of the vertical beam waist position. The beam sizes measured after two complete tuning sessions were almost a factor three larger than the design values. Comparison with the nominal β_y^* optics suggests that the beam size growth due to machine imperfections for lower β_y^* values is much stronger than expected in the design. The experimental results are also compared with the tuning simulations. The realistic errors applied to the machine model are not sufficient to reproduce the experimental results. Simulation results get closer to the experiment for larger machine errors. Simulations also show that an accurate orbit correction can help in lowering the IP beam size. The main reasons for observing larger beam sizes than expected are identified: insufficient orbit control and sensitivity to machine drifts, contribution of wakefields combined with the beam orbit jitter, larger multipolar fields, larger magnet alignment errors, instrumentation errors and stability (especially Shintake monitor and beam position monitors). Addressing these issues is recommended for future experiments with low β_y^* optics in the ATF2.

Contents

Chapter 1

Introduction

1.1. Standard Model and beyond

All known elementary particles and their interactions are very well described within the Standard Model (SM) [1]. It specifies that matter is composed of the half-integer spin particles called fermions and the integer spin particles called bosons which mediate the forces. The SM particles have associated antiparticles of the same mass but opposite quantum numbers.

Fermions are classified into leptons and quarks. There are three known leptons of charge -1 (in units of elementary electric charge): the electron e^-, the muon μ^- and the taon τ^-; and the three corresponding neutrinos ν_e, ν_μ and ν_τ of no charge. The six known quarks can be classified into up-type of electric charge $+\frac{2}{3}$: up (u), charm (c) and top (t); and down-type of electric charge $-\frac{1}{3}$: down (d), strange (s) and bottom (b). Quarks have an additional quantum number, the color, which can be of three types. Quarks are confined into colorness particles called hadrons: mesons made of quark and antiquark and baryons made of three quarks. Most of the observed ordinary matter is built of atoms: the nuclei composed of protons (baryons with uud quarks) and neutrons (baryons with ddu quarks) surrounded by the electrons.

The Standard Model describes three fundamental forces that occur between leptons and quarks: the strong, the weak and the electromagnetic force. Quarks interact via all three forces, charged leptons are not sensitive to the strong force and neutrinos are subject only to the weak force. These interactions are mediated by bosons. There are eight gluons $\mathrm{g}_\alpha,\ \alpha = 1,..8$ that mediate the strong interactions among quarks, photon γ is the exchanged particle in the electromagnetic interaction and the three weak bosons $\mathrm{W}^\pm$, Z are exchanged in the weak interactions. Figure 1.1 summarizes the known SM particles and their main parameters grouped into families and generations.

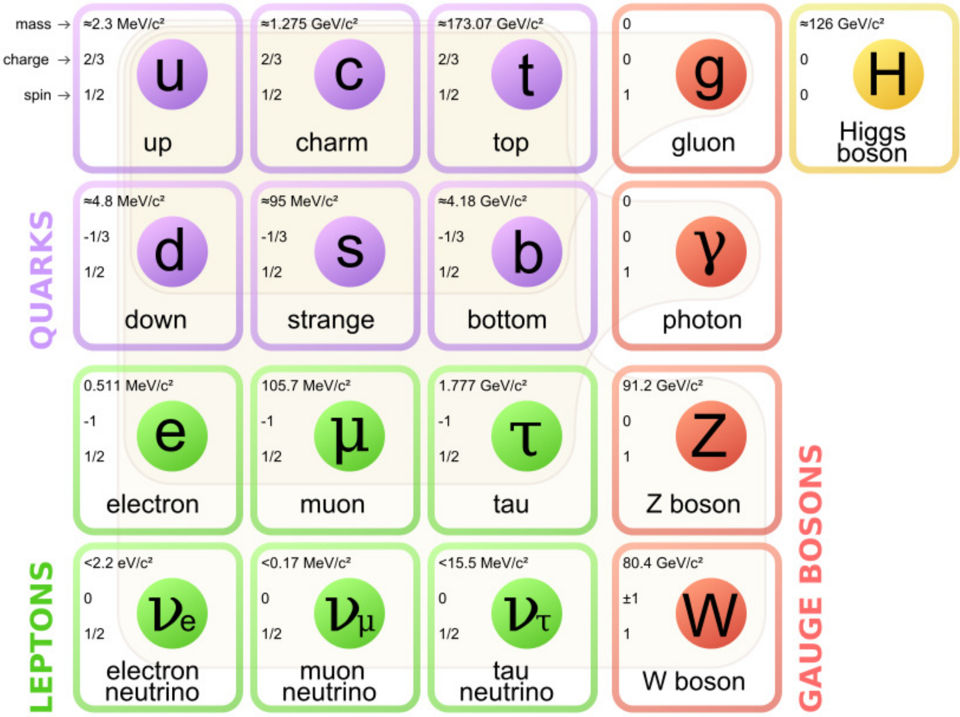

Figure 1.1: The known SM particles with their main parameters (graphics from [2]).

The SM is a quantum field theory based on the gauge symmetry $SU(3)_C \times SU(2)_L \times U(1)_Y$. The strong interaction is defined by the symmetry group $SU(3)_C$. The symmetry group of the electromagnetic interaction $U(1)_{EM}$ appears in the SM as a subgroup of $SU(2)_L \times U(1)_Y$, the symmetry group of electroweak interactions. In this sense the electromagnetic and weak interactions are unified. The fact that the weak gauge bosons are massive particles (see Fig. 1.1) indicates that $SU(2)_L \times U(1)_Y$ is not a symmetry group of vacuum. On the other hand, the photon being massless reflects that $U(1)_{EM}$ is a symmetry of the vacuum. Therefore, the Spontaneous Symmetry Breaking pattern in the SM must be:

$$SU(3)_C \times SU(2)_L \times U(1)_Y \longrightarrow SU(3)_C \times U(1)_{EM}. \tag{1.1}$$

Such a pattern is included in the SM by the Brout-Englert-Higgs Mechanism [3, 4] which provides the proper masses to the $W^{\pm}$, Z bosons and to the fermions and leaves as a consequence the prediction of a new particle: the Higgs boson. This particle was finally observed in 2012 at the Large Hadron Collider (LHC) at CERN [5, 6] with a mass of 125.7 ± 0.4 Gev [7] making the SM complete.

Beyond the Standard Model (BSM)

According to [8], the Standard Model is a complete theory both from an experimental and a theoretical point of view. It explains all observations at the LHC and at preceding experiments and shows no inconsistencies between theory and experiments [9]. However, there are several phenomena that are not described by the SM, e.g.: quantum gravity [10], dark matter [11], the matter-antimater asymmetry of the universe [12], neutrino oscillations [13]. A leading candidate for a theory that can solve some of these problems is Supersymmetry [8]. Supersymmetry is an extension of the symmetry structure of the SM that relates fermions and bosons [14]. The simplest supersymmetric extension of the SM is the Minimal Supersymmetric Standard Model (MSSM) [8]. It assumes that the known SM particles are associated with a superpartner particle, the spin of which differs by a half-integer. These new fundamental particles should appear in a TeV particle collider if the theory is correct. Searches for such particles are being carried out at the Large Hadron Collider (LHC) [15]; however, no particles beyond the SM have been observed yet [8]. A new, more precise particle collider will be needed to study the properties of the BSM particles once they are discovered.

1.2. Linear and circular colliders

The purpose of a particle collider is to deliver the maximum rate of useful particle events ($\frac{\mathrm{R}}{\mathrm{T}}$) at the minimum cost. The first quantity is defined by the product the luminosity ($\mathscr{L}$) and the cross section of the process (σ_{p}):

$$\frac{\mathrm{R}}{\mathrm{T}} = \mathscr{L}\sigma_{\mathrm{p}}. \tag{1.2}$$

The luminosity of two colliding beams is expressed by

$$\mathscr{L} = \frac{\mathrm{N_p^2 n_b f_{rep}}}{\mathrm{A}}\mathrm{H_D}, \tag{1.3}$$

where $\mathrm{N_p}$ is the number of particles per bunch, $\mathrm{n_b}$ is the number of bunches per train, $\mathrm{f_{rep}}$ is the repetition frequency of the trains, A is the effective overlap area of the colliding beams at the interaction point (IP) and $\mathrm{H_D}$ is the luminosity enhancement factor [16]. Assuming Gaussian bunch distributions and head-on collisions, Eq. (1.3) becomes

$$\mathscr{L} = \frac{\mathrm{N_p^2 n_b f_{rep}}}{4\pi\sigma_{\mathrm{x}}^{*}\sigma_{\mathrm{y}}^{*}}\mathrm{H_D}, \tag{1.4}$$

where σ_x^* and σ_y^* are the horizontal and vertical beam sizes of the bunch and * denotes the parameters at the IP[1]. One can see that the luminosity can be increased by reducing the transverse beam sizes at the IP.

A high centre-of-mass energy is required in the particle physics experiments in order to produce heavy particles of the SM and to search for new particles. With the currently available technology, the highest achievable beam energy is on the order of TeV or tens of TeV depending on the design. At this energy regime the cross sections of many processes of interest are small and they generally decrease quadratically with the centre-of-mass energy [17]. Therefore large luminosities on the order of 10^{34} $\mathrm{cm}^{-2}\mathrm{s}^{-1}$ are required to deliver a high event rate.

Particle colliders are designed such that they fulfill the experimental requirements at the minimum possible cost. There are two main types of particle colliders in terms of shape: linear and circular. The main advantage of a circular collider is that it is generally more compact and its integrated accelerating gradient can be lower as the acceleration acts on particles at every turn. On the other hand, each time the charged particle trajectory is bent to close the loop synchrotron light is emitted. The power emitted by a single particle is:

$$P_\gamma = \frac{2}{3}\frac{e^2 c}{4\pi\varepsilon_0}\frac{\beta^4\gamma^4}{\rho_r^2}, \tag{1.5}$$

where e is the electron charge, ε_0 is the electric permittivity of vacuum, β is the relativistic velocity defined as a ratio between the particle velocity v and the speed of light c, γ is the Lorentz factor (E/m_0c^2) and ρ_r is the bending radius of the particle trajectory. The energy loss due to the synchrotron radiation grows with the fourth power of the particle energy which limits the maximum beam energy. Therefore, use of heavy particles with large m_0 and machines with large bending radii is preferred to minimise the energy loss by the synchrotron radiation. As described in Section 1.1, hadrons are not elementary particles as they are composed of quarks and gluons with some internal momentum. In consequence, the collision energy cannot be accurately defined which affects the measurement precision of the collision products. In contrast, in a lepton collider the collision energy is very well defined and the collision products are cleaner and easier to analyse as leptons are not subject to the strong force. However, because of the synchrotron radiation, reaching TeV energies by a lepton collider is practically feasible only if it is linear [18].

To summarize, the circular collider is preferred for colliding hadrons as it gives relatively easy access to TeV energies but hadron collision measurements are less precise and more difficult to analyse. The lepton collider has a higher physics potential (that will be described in the Section 1.3) but accessing TeV energies is much more difficult and practically only possible in a

---

[1] in the whole document

linear implementation. In practice these two types of high energy colliders are complementary: the results from the circular collider give general information of physics at TeV energies and allow us to make a design of an efficient linear collider. This is exactly the current situation in high energy physics: the LHC colliding protons with a centre-of-mass energy up to 14 TeV searches for new physics and specifies the requirements for the linear collider to be used for very precise measurements of the phenomena discovered at the LHC.

1.3. Physics potential of linear colliders

Colliding leptons of a well defined interaction state is the main advantage of linear colliders over hadron colliders. The high measurement precision is achievable because of the high detector resolution due to background processes being well understood and measured, a clean experimental environment, ability to scan the centre-of-mass energy systematically and the possibility of beam polarisation.

The physics potential strongly depends on the centre-of-mass energy [19]. Energies of less than 1 TeV are favorable for precise measurements of Higgs and top quark properties. Higher energies open the energy frontier, allowing for the discovery of new physics phenomena, while also giving access to additional Higgs and top quark properties. 3 TeV is the maximum energy that is currently seen as feasible by the existing linear collider designs (described in detail in Section 2.5). Such energy gives an access for the discovery and accurate measurement of pair-produced particles with a mass up to 1.5 TeV or single particles up to 3 TeV which is of special interest for the BSM theories.

Higgs production

The cross sections of the main Higgs production processes at an $\mathrm{e}^+\mathrm{e}^-$ are depicted on Fig. 1.2 as a function of the centre-of-mass energy. The Feynman diagrams of these processes are presented in Fig. 1.3 and 1.4. At centre-of-mass energies below 1 TeV the Higgsstrahlung ($e^+e^- \to ZH$, Fig. 1.3) is the dominant process, but the WW-fusion process ($e^+e^- \to H\nu_e\overline{\nu_e}$, Fig. 1.3) is also significant. The combined study of these two processes probes the Higgs boson properties (width and branching ratios) in a model-independent manner [19]. For higher energies, Higgs production is dominated by the WW-fusion process, with the ZZ-fusion process ($e^+e^- \to He^+e^-$, Fig. 1.3) also becoming significant. This allows for precise measurements of the coupling of the Higgs boson to both fermions and gauge bosons [19]. Additionally, the rarer processes such as $e^+e^- \to t\bar{t}H$ and $e^+e^- \to HH\nu_e\overline{\nu_e}$ (see Fig. 1.4) provide access to the top Yukawa coupling and the Higgs trilinear self-coupling.

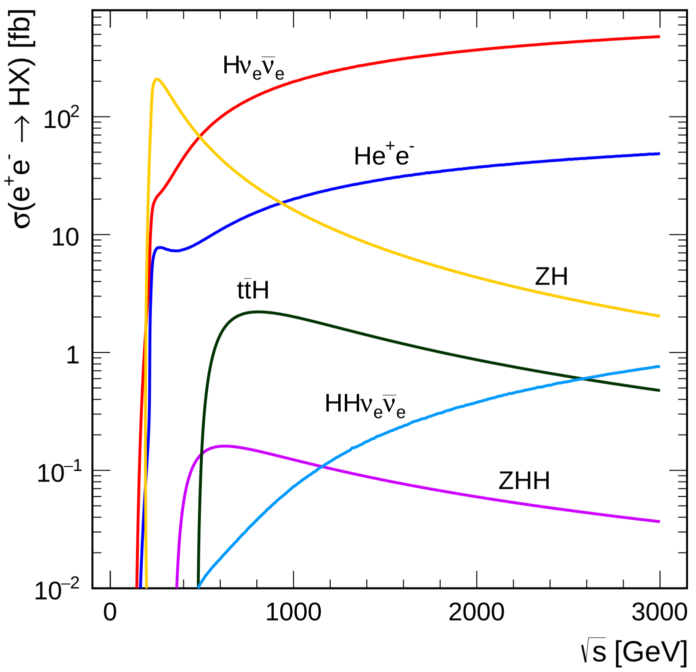

Figure 1.2: Cross sections of the main Higgs production processes at an e^+e^- *collider as a function of the centre-of-mass energy (graphics from [19]).*

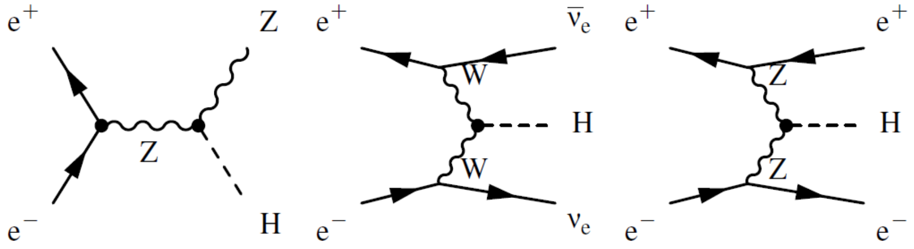

Figure 1.3: The three highest cross section Higgs production processes at an e^+e^- *collider. From the left: Higgsstrahlung, WW-fusion, ZZ-fusion (graphics from [19]).*

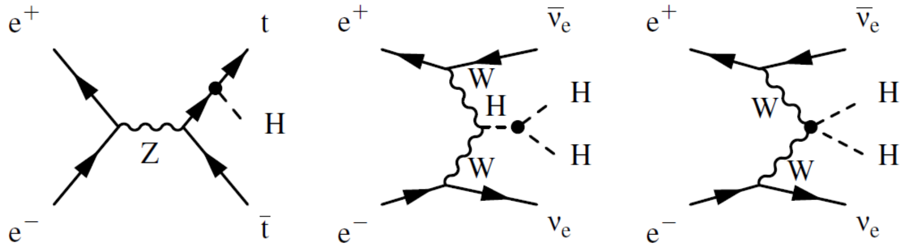

Figure 1.4: The main processes at an e^+e^- *collider involving the top Yukawa coupling* g_{Htt}*, the Higgs boson trilinear self-coupling* λ *and the quartic coupling* g_{HHWW} *(graphics from [19]).*

Top quark production

The top quark is the heaviest particle of the SM and therefore the most strongly coupled to the Higgs field. For this reason it plays a major role in the calculation of higher order corrections for many SM processes, and it has an important role in many BSM models. The uncertainty of the top quark mass [20, 21, 22] is currently (together with the Higgs mass) the leading uncertainty in tests of the SM vacuum stability [23, 24]. The future linear collider will measure the mass of the top quark in a direct way which is not possible at hadron collider, fixing an important parameter for particle physics calculations. An example of a top mass measurement in an e^+e^- collider using a threshold scan technique is visualized in Fig. 1.5 [25]. This method is based on measuring the $t\bar{t}$ production cross section around the centre-of-mass energy of 350 GeV. In this energy range, the $t\bar{t}$ cross section rises from 50 fb to about 500 fb. Such a study cannot be performed at hadron colliders, where the parton-parton centre-of-mass energy is not known.

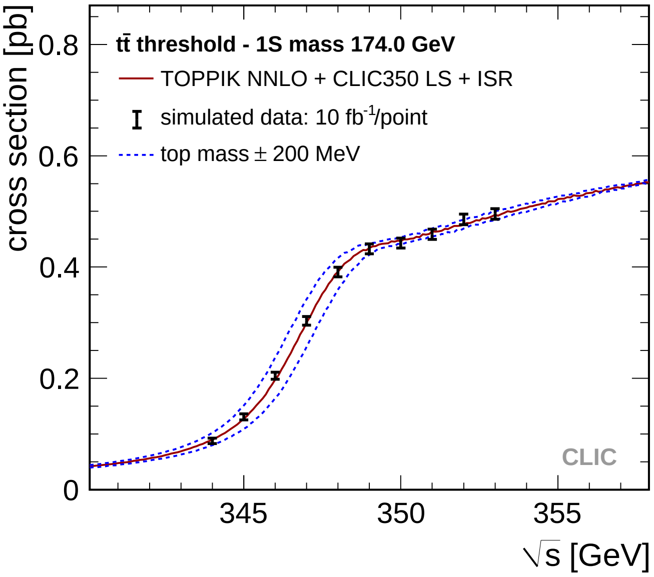

Figure 1.5: Simulated $t\bar{t}$ *cross section as a function of centre-of-mass energy for* $t\bar{t}$ *(graphics from [19]).*

New Physics

A possible new physics beyond the Standard Model, if it exists, should be discovered at the LHC. However, the LHC does not have the required precision to deeply study the properties of these new particles. Therefore it is important to start examining how this sensitivity can be further extended at the future linear collider.

BSM physics is expected to be of a supersymmetric nature. Study of an example supersymmetric model (model III) performed in the frame of CLIC (described in Section 2.5) can be found in [26]. This scenario is consistent with all known constraints on supersymmetry and its lightest supersymmetric particle is a good candidate to be the cold dark matter of the universe [27]. The cross sections of new particles predicted by this model are presented in Fig. 1.6 as a function of centre-of-mass energy.

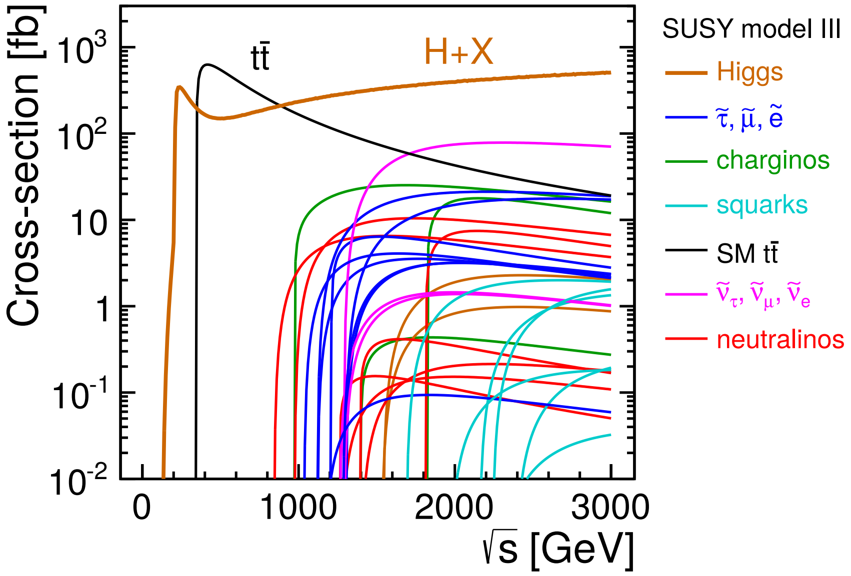

Figure 1.6: Cross sections for pairs of superpartners in model III [26] as a function of e^+e^- *centre-of-mass energy (graphics from [27]).*

Chapter 2

Linear colliders

Linear colliders are described in more detail in this Chapter. Firstly, selected beam dynamics subjects useful in the scope of this thesis are introduced. Later, the main parts of a linear collider are described with a special emphasis given to the final focus system, which is of main interest in my study. Finally, two existing designs for a future linear collider will be compared and a brief summary of linear collider test facilities will be given.

2.1. Concepts in beam dynamics

A set of $\mathrm{N_p}$ particles traveling in the collider is referred to as a beam. The behavior of beams can be studied by tracing the individual particles or by analyzing the transfer properties of the optical functions that bound the particles contained in the beam. A special coordinate system so-called Frenet-Serret (Fig. 2.1) is commonly used for describing the particle's motion. This system follows the beam design trajectory. The longitudinal position along the trajectory is denoted by s. The particle position deviation from the design trajectory is denoted by z in the longitudinal direction, x in the transverse horizontal direction and y in the transverse vertical direction. The set of following variables is used to describe the particle's phase-space: $(\mathrm{x}, \mathrm{x}', \mathrm{y}, \mathrm{y}', \mathrm{z}, \delta_\mathrm{p})$, where $'$ denotes a derivative over the s variable ($\mathrm{x}' = \frac{\mathrm{dx}}{\mathrm{ds}}$, $\mathrm{y}' = \frac{\mathrm{dy}}{\mathrm{ds}}$), and $\delta_\mathrm{p} = \frac{\Delta \mathrm{p}}{\mathrm{p_0}}$ is the relative momentum deviation from the design momentum. In some cases it is more convenient to use the transverse momenta $\mathrm{p_x}$, $\mathrm{p_y}$ instead of the angular variables x', y'. The relation between them is the following: $\mathrm{x}' = \frac{\mathrm{p_x}}{\mathrm{p_s}}$, $\mathrm{y}' = \frac{\mathrm{p_y}}{\mathrm{p_s}}$, where $\mathrm{p_s}$ is the particle momentum along the s direction. Both conventions are used in the scope of this thesis.

Here, only the transverse beam dynamics are described, as the longitudinal beam dynamics are less important in the parts of machine without acceleration that are considered in this thesis.

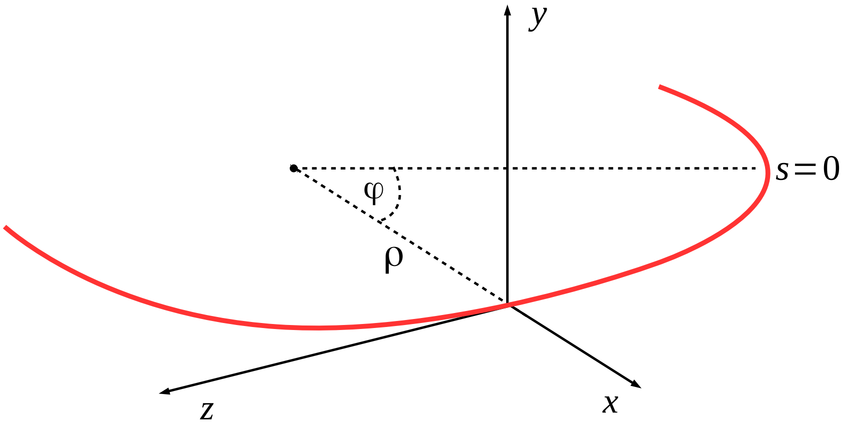

Figure 2.1: Frenet-Serret reference system (in black) along the design trajectory (in red).

2.1.1. Linear beam dynamics

In a linear regime, the transverse motion of a single particle can be written as [28]:

$$\mathrm{u}(\mathrm{s}) = \mathrm{u}_\beta(\mathrm{s}) + \eta_\mathrm{u}(\mathrm{s})\delta_\mathrm{p}, \tag{2.1}$$

where u stands for x or y, $\mathrm{u}_\beta(\mathrm{s})$ is the trajectory variation due to betatron motion (transverse oscillations), $\eta_u(s)\delta_p$ is the trajectory change resulting from an energy offset and $\eta_\mathrm{u}(\mathrm{s})$ is a dispersion function.

The betatron motion can be characterized by a pseudo-harmonic oscillation of the form [28]:

$$\mathrm{u}_\beta(\mathrm{s}) = \sqrt{2\mathrm{I}_\mathrm{u}\beta_\mathrm{u}(\mathrm{s})}\cos\left(\mu_\mathrm{u}(\mathrm{s}) + \mu_0\right), \tag{2.2}$$

where $\beta_\mathrm{u}(\mathrm{s})$ is the beta function, $\mu_\mathrm{u}(\mathrm{s}) = \int_0^\mathrm{s}\beta_\mathrm{u}^{-1}(\mathrm{s}')\mathrm{d}\mathrm{s}'$ the betatron phase and I_u is an action variable. The action I_u and initial phase μ_0 are constants of motion and the functions $\beta_\mathrm{u}(\mathrm{s})$ and $\mu_\mathrm{u}(\mathrm{s})$ depend on s.

Two other important functions, related to the β function, are α and γ functions defined as:

$$\alpha_\mathrm{u} \equiv -\frac{1}{2}\frac{d\beta_u}{ds}, \tag{2.3a}$$

$$\gamma_u \equiv \frac{1+\alpha_u^2}{\beta_u}. \tag{2.3b}$$

The set of these six functions $(\beta_{\mathrm{x,y}}, \alpha_{\mathrm{x,y}}, \gamma_{\mathrm{x,y}})$, called the Courant-Snyder functions [28], together with the phase function $\mu_\mathrm{u}(\mathrm{s})$ describe the complete linear motion for on-momentum particles.

It is often said that these functions define the optics of the machine.

Another important quantity describing the beam is the beam emittance. It is defined as the averaged value of I_u over all particles of a beam:

$$\varepsilon_u^{rms} = \langle I_u \rangle . \tag{2.4}$$

The three optical functions can be also defined in a statistical approach as they are proportional to the three second moments of the beam distribution, with the beam emittance being a constant of proportionality. Assuming no offset between the beam and the centre of the coordinate system:

$$\begin{aligned} \left\langle u^2 \right\rangle_s &= \varepsilon_u^{rms} \beta_u(s), && \text{(2.5a)} \\ \left\langle uu' \right\rangle_s &= -\varepsilon_u^{rms} \alpha_u(s), && \text{(2.5b)} \\ \left\langle u'^2 \right\rangle_s &= \varepsilon_u^{rms} \gamma_u(s), && \text{(2.5c)} \end{aligned}$$

where $\langle ... \rangle_s$ denotes an average over the beam distribution at the location s. The linear transverse rms beam size at the given location s is therefore defined as:

$$\sigma_u^{rms}(s) = \sqrt{\langle u^2 \rangle_s - \langle u \rangle_s^2} = \sqrt{\langle u^2 \rangle_s} = \sqrt{\varepsilon_u^{rms} \beta_u(s)}. \tag{2.6}$$

Beam emittance defined by Eq. 2.4 varies when beam energy changes. One can define an invartiant under acceleration, the normalized emittance, given by:

$$\varepsilon_N = \gamma \varepsilon, \tag{2.7}$$

where $\gamma = E/m_0c^2$ is the relativistic factor.

The motion of a single particle can be also represented in terms of a transport matrix [29]. In such cases, the trajectory of every particle is given by a point in phase space (u,u') which is transformed from the initial location i to a final location f through a linear transformation:

$$\begin{bmatrix} u \\ u' \end{bmatrix}_f = \begin{bmatrix} R_{11} & R_{12} \\ R_{11} & R_{12} \end{bmatrix}_{fi} \begin{bmatrix} u \\ u' \end{bmatrix}_i . \tag{2.8}$$

The basic elements in particle transport lines are drift spaces, bending magnets (dipoles) and focusing magnets (quadrupoles). The transport matrix of a drift space of length L is given by:

$$\mathrm{R_{drift}} = \begin{bmatrix} 1 & L \\ 0 & 1 \end{bmatrix}. \tag{2.9}$$

The transport matrix of a rectangular dipole in a bending plane is given by:

$$\mathrm{R_{dipole}} = \begin{bmatrix} \cos\left(\frac{\mathrm{l_d}}{\rho_\mathrm{d}}\right) & \rho_d \sin\frac{l_d}{\rho_d} \\ -\frac{1}{\rho_\mathrm{d}}\sin\frac{\mathrm{l_d}}{\rho_\mathrm{d}} & \cos\left(\frac{l_d}{\rho_d}\right) \end{bmatrix}, \tag{2.10}$$

where ρ_d is a bending radius and $\mathrm{l_d}$ is magnet length. For a quadrupole of a gradient $\mathrm{K} = (\partial \mathrm{B_T}/\partial \mathrm{u})/(\mathrm{B}\rho)$ and length $\mathrm{L_q}$, where $\mathrm{B_T}$ is pole-tip field and $\mathrm{B}\rho$ is the magnetic rigidity, the transfer matrix is given by:

$$\mathrm{R_{quadrupole,focusing}} = \begin{bmatrix} \cos\left(\mathrm{L_q}\sqrt{|\mathrm{K}|}\right) & \sin\left(L_q\sqrt{|K|}\right)/\sqrt{|K|} \\ -\sqrt{|\mathrm{K}|}\sin\left(\mathrm{L_q}\sqrt{|\mathrm{K}|}\right) & \cos\left(L_q\sqrt{|K|}\right) \end{bmatrix}, \tag{2.11}$$

for a focusing quadrupole, and

$$\mathrm{R_{quadrupole,defocusing}} = \begin{bmatrix} \cosh\left(\mathrm{L_q}\sqrt{|\mathrm{K}|}\right) & \sinh\left(L_q\sqrt{|K|}\right)/\sqrt{|K|} \\ -\sqrt{|\mathrm{K}|}\sinh\left(\mathrm{L_q}\sqrt{|\mathrm{K}|}\right) & \cosh\left(L_q\sqrt{|K|}\right) \end{bmatrix}, \tag{2.12}$$

for a defocusing quadrupole.

In the thin-lens approximation ($\mathrm{L_q} \to 0$) and for a constant integrated gradient $\mathrm{k} = |\mathrm{K}|\,\mathrm{L_q}$, the quadrupole transport matrices simplify to:

$$\mathrm{R_{quad,thin-lens,focusing}} = \begin{bmatrix} 1 & 0 \\ -\mathrm{k} & 1 \end{bmatrix}, \tag{2.13}$$

$$\mathrm{R_{quad,thin-lens,defocusing}} = \begin{bmatrix} 1 & 0 \\ \mathrm{k} & 1 \end{bmatrix}. \tag{2.14}$$

Thus, the focal length of the thin quadrupole is given by $\pm 1/\mathrm{k}$. The transport matrix for a sequence of drift spaces, dipoles and quadrupoles is the product of the transport matrices for the individual elements.

Both approaches, tracing the individual particles or analyzing the optical functions are equivalent and complementary. The optical functions can be transformed from one location to another using the elements of the transport matrix R:

$$\begin{bmatrix}\beta\\ \alpha\\ \gamma\end{bmatrix}_{\mathrm{f}} = \begin{bmatrix}\mathrm{R}_{11}^2 & -2R_{11}R_{12} & R_{12}^2\\ -\mathrm{R}_{11}\mathrm{R}_{21} & 1+2R_{12}R_{21} & -R_{12}R_{22}\\ \mathrm{R}_{21}^2 & -2R_{21}R_{22} & R_{22}^2\end{bmatrix}_{\mathrm{fi}} \begin{bmatrix}\beta\\ \alpha\\ \gamma\end{bmatrix}_{\mathrm{i}} . \tag{2.15}$$

Alternatively, the elements of the R matrix from an initial location i to a final location f can be expressed in terms of the optical functions at the initial and final locations:

$$\mathrm{R}_{\mathrm{fi}} = \begin{bmatrix}\sqrt{\frac{\beta_{\mathrm{f}}}{\beta_{\mathrm{i}}}}(\cos(\mu_{\mathrm{fi}})+\alpha_{\mathrm{i}}\sin(\mu_{\mathrm{fi}})) & \sqrt{\beta_f\beta_i}\sin(\mu_{fi})\\ -\frac{1+\alpha_{\mathrm{f}}\alpha_{\mathrm{i}}}{\sqrt{\beta_{\mathrm{f}}\beta_{\mathrm{i}}}}\sin(\mu_{\mathrm{fi}})+\frac{\alpha_{\mathrm{i}}-\alpha_{\mathrm{f}}}{\sqrt{\beta_{\mathrm{f}}\beta_{\mathrm{i}}}}\cos(\mu_{\mathrm{fi}}) & \sqrt{\frac{\beta_f}{\beta_i}}(\cos(\mu_{fi})-\alpha_f\sin(\mu_{fi}))\end{bmatrix}, \tag{2.16}$$

where $\mu_{\mathrm{fi}} = (\mu_{\mathrm{f}} - \mu_{\mathrm{i}})$ is the betatron phase advance between the two locations.

2.1.2. Nonlinear beam dynamics

The linear beam dynamics provide an approximated description of the particle transport in accelerators. Due to the presence of the nonlinear fields coming from the multipole magnets of multipolar field errors, or due to the very high strength of some magnets, a treatment of the beam dynamics beyond the linear regime is required. For this reason, two methods of describing the nonlinear beam dynamics are introduced in this section: the Taylor maps and the Lie algebra formalism. An extensive overview of nonlinear beam dynamics can be found in [30] and [31].

Taylor Maps

The transfer maps, similar to the transfer matrices, transform the initial set of particle coordinates (z_0) to the final state (z_{f}):

$$\mathscr{M} : \mathrm{z}_0 \mapsto \mathrm{z}_{\mathrm{f}}, \mathrm{z}_{\mathrm{f}} = \mathscr{M}\mathrm{z}_0, \tag{2.17}$$

where $\mathrm{z} = (\mathrm{x}, \mathrm{p}_{\mathrm{x}}, \mathrm{y}, \mathrm{p}_{\mathrm{y}}, \delta)$ is the five-dimensional vector in the Frenet-Serret reference system. The difference is that here $\mathscr{M}$ represents a symplectic mapping that contains the nonlinear terms. Such a transformation can be written in the following form:

$$\mathrm{z}_{\mathrm{f}} = \mathscr{M}\mathrm{z}_0 = \sum_{\mathrm{ijklm}} \mathrm{X}_{\mathrm{ijklm}}\mathrm{x}^{\mathrm{i}}\mathrm{p}_{\mathrm{x}}^{\mathrm{j}}\mathrm{y}^{\mathrm{k}}\mathrm{p}_{\mathrm{y}}^{\mathrm{l}}\delta^{\mathrm{m}}. \tag{2.18}$$

The order of the coefficients is given by $\mathrm{q} = \mathrm{i}+\mathrm{j}+\mathrm{k}+\mathrm{l}+\mathrm{m}$. It simplifies to a linear transformation for $\mathrm{q} = 1$.

Let us consider an example of calculating the rms beam size at the final state ($\mathrm{z_f}$) given that the initial state ($\mathrm{z_0}$) is known [32]. Assuming the symplectic beam line transport ($\rho_\mathrm{f} \mathrm{d}\nu_\mathrm{f} = \rho_0 \mathrm{d}\nu_0$) the first moment of particle distribution is given by:

$$
\begin{aligned}
\langle \mathrm{z_f} \rangle = \int_{-\infty}^{\infty} \mathrm{z_f} \rho_\mathrm{f} \mathrm{d}\nu_\mathrm{f} = \int_{-\infty}^{\infty} \sum_{\mathrm{ijklm}} \mathrm{X_{ijklm}} \mathrm{x_0^i p_{x,0}^j y_0^k p_{y,0}^l} \delta_0^\mathrm{m} \rho_\mathrm{f} \mathrm{d}\nu_\mathrm{f} = \\
= \sum_{\mathrm{ijklm}} \mathrm{X_{ijklm}} \int_{-\infty}^{\infty} \mathrm{x_0^i p_{x,0}^j y_0^k p_{y,0}^l} \delta_0^\mathrm{m} \rho_0 \mathrm{d}\nu_0
\end{aligned}
\tag{2.19}
$$

The rms beam size can be then calculated according to the rms definition:

$$
\begin{aligned}
\sigma_{\mathrm{z,f}}^2 = \left\langle \mathrm{z_f^2} \right\rangle - \langle \mathrm{z_f} \rangle^2 = \sum_{\substack{ijklm \\ i'j'k'l'm'}} \mathrm{X_{ijklm} X_{i'j'k'l'm'}} \int_{-\infty}^{\infty} \mathrm{x_0^{i+i'} \, p_{x,0}^{j+j'} \, y_0^{k+k'} \, p_{y,0}^{l+l'}} \, \delta_0^{\mathrm{m+m'}} \rho_0 \mathrm{d}\nu_0 \\
- \left(\sum_{\mathrm{ijklm}} \mathrm{X_{ijklm}} \int_{-\infty}^{\infty} \mathrm{x_0^i p_{x,0}^j y_0^k p_{y,0}^l} \delta_0^\mathrm{m} \rho_0 \mathrm{d}\nu_0 \right)^2 .
\end{aligned}
\tag{2.20}
$$

Such a way of calculating the beam size was widely used in the studies described in Chapter 4.

Lie algebra methods

The Lie algebra formalism [31, 33, 34] is a robust and powerful method to analytically solve a wide range of beam dynamics problems with a high degree of nonlinearity. It preserves symplecticity in the solution and avoids nonphysical errors of the numerical algorithms. The basic formalism and applications for accelerator physics will be introduced in this section.

We start with a reminder of the basis of Hamiltonian mechanics. Consider a particle of generalized coordinates $(\vec{x}, \vec{p}) = (\mathrm{x_i}, \mathrm{p_i})$ in 6-D phase space (i=1,2,3). The evolution of the coordinates can be described using the Hamiltonian equations of motion:

$$
\frac{\mathrm{dx_i}}{\mathrm{dt}} = \frac{\partial \mathrm{H}}{\partial \mathrm{p_i}}; \ \frac{\mathrm{dp_i}}{\mathrm{dt}} = -\frac{\partial \mathrm{H}}{\partial \mathrm{x_i}},
\tag{2.21}
$$

where H is the Hamiltonian of the system. For a relativistic particle in an electromagnetic field the Hamiltonian reads

$$
\mathrm{H}(\vec{x}, \vec{p}, \mathrm{t}) = \mathrm{c} \sqrt{\left(\vec{p} - \mathrm{e} \vec{A} \left(\vec{x}, \mathrm{t} \right) \right)^2 + \mathrm{m_0^2 c^2}} + \mathrm{e} \Phi \left(\vec{x}, \mathrm{t} \right),
\tag{2.22}
$$

where $\overrightarrow{A}(\overrightarrow{x},t)$, $\Phi(\overrightarrow{x},t)$ are the vector and scalar potentials of an electromagnetic field, m_0 is the electron rest mass, e is the electron charge, and c is the speed of light. Using canonical variables and the design path length s as an independent variable (bending with radius ρ in x-plane) the Hamiltonian can be rewritten as:

$$H = -\left(1+\frac{x}{\rho}\right)\sqrt{\left(1+\delta_p\right)^2 - p_x^2 - p_y^2} + \frac{x}{\rho} + \frac{x^2}{2\rho^2} - \frac{A_s(x,y)}{B_0\rho}, \tag{2.23}$$

where δ_p is the relative momentum deviation and $A_s(x,y)$ the longitudinal component of the vector potential.

We describe the magnetic field with the multipole expansion:

$$B_y + iB_x = \sum_{n=1} (b_n + ia_n)(x+iy)^{n-1} \tag{2.24}$$

and, since $\overrightarrow{B} = \nabla \times \overrightarrow{A}$,

$$A_s(x,y) = \sum_{n=1} \frac{1}{n}\left[(b_n + ia_n)(x+iy)^n\right]. \tag{2.25}$$

Here $n = 1$ refers to dipolar fields. For a usual case of $x \ll \rho$ the Hamilton can be written as:

$$H = \frac{p_x^2 + p_y^2}{2\left(1+\delta_p\right)} - \frac{x\delta_p}{\rho} + \frac{x^2}{2\rho^2} + \frac{k_q}{2}\left(x^2 - y^2\right) + \frac{k_s}{6}\left(x^3 - 3xy^2\right) + \ldots, \tag{2.26}$$

where $k_q = \frac{1}{B\rho}\frac{\partial B_y}{\partial x}$ and $k_s = \frac{1}{B\rho}\frac{\partial^2 B_y}{\partial x^2}$. The first term in Eq. (2.26) is the kinematic term, second and third are dipolar terms, fourth is the quadrupolar term, fifth is the sextupolar term and so on.

Knowing the Hamiltonian, the particle coordinate's evolution can be calculated using the Hamiltonian equations. The evolution of a dynamical variable f can be calculated using the Poisson bracket. The Poisson bracket $[f,g]$ of any two functions f and g is defined as:

$$[f,g] = \sum_i \left(\frac{\partial f}{\partial x_i}\frac{\partial g}{\partial p_i} - \frac{\partial f}{\partial p_i}\frac{\partial g}{\partial x_i}\right). \tag{2.27}$$

Therefore, the time evolution of a dynamical variable f, where f is any smooth function of x_i and p_i along a trajectory, is given by:

$$\frac{df}{dt} = \frac{\partial f}{\partial t} + \sum_i \left(\frac{\partial f}{\partial x_i}\frac{dx_i}{dt} + \frac{\partial f}{\partial p_i}\frac{dp_i}{dt}\right) = \frac{\partial f}{\partial t} + [f,H]. \tag{2.28}$$

Particularly, for $f = H$ one gets $\frac{dH}{dt} = \frac{\partial H}{\partial t}$ and if H does not explicitly depend on time then $\frac{dH}{dt} = 0$

which expresses the conservation of the quantity H, usually the energy of the system.

Definition 2.1.1. A Lie operator : f : acting on function g, where g is any function of (x_i, p_i), is defined as:

$$:f:g \equiv [f,g] \tag{2.29}$$

Definition 2.1.2. A Lie transformation is the exponential adjoint Lie operator:

$$\mathfrak{L} \equiv e^{:f:} = \sum_{i=0}^{\infty} \frac{1}{i!}(:f:)^i = 1 + :f: + \frac{1}{2!}(:f:)^2 + \frac{1}{3!}(:f:)^3 + ... \tag{2.30}$$

that acts on a function g as:

$$\mathfrak{L}g = e^{:f:}g = g + [f,g] + \frac{1}{2!}[f,[f,g]] + \dots \,. \tag{2.31}$$

We can choose the function g to represent the particle coordinates at a given location s: $g(s) = (x_i, p_i)_s$. A Lie transformation acting on the phase-space coordinates (x_i, p_i) at a location s_1 propagates them to another location s_2:

$$e^{:f:}(x_i, p_i)_{s1} = (x_i, p_i)_{s2}. \tag{2.32}$$

The motion from a location s_1 to a location s_2 is fully described by the function f. Given a beamline element of length L and the Hamiltonian H, the generator $f = -LH$ [35].

An accelerator beamline consist of a series of elements, usually drifts, dipoles, quadrupoles, etc. For each element a Hamiltonian can be defined along with the corresponding Lie transformation. The exponential operators for the sequence of elements can be concatenated using the Baker-Campbell-Hausdorff (BCH) formula:

$$e^{:f:}e^{:g:} = e^{:h:}, \tag{2.33}$$

where f and g are fully differentiable functions of the dynamic variables and h reads:

$$h = f + g + \frac{1}{2}[f,g] + \frac{1}{12}[f-g,[f,g]] + ... \tag{2.34}$$

Using the BCH formula, the whole sequence of elements can be expressed in one unique term that contains the whole information of the system:

$$\prod_i \exp(:-l_i H_i:) = \exp(:-L_{eff}H_{eff}:)\,, \tag{2.35}$$

where L_{eff} is the total length of the system and H_{eff} is the effective Hamiltonian that represents the complete series of elements. The Hamiltonians in the 6–D phase space $(\mathrm{x},\mathrm{p_x},\mathrm{y},\mathrm{p_y},\mathrm{z},\delta_\mathrm{p})$ describing the dynamics of a particle in a dipole magnet, a quadrupole magnet, a sextupole magnet and an octupole magnet are given in Eqs. (2.36) [35].

$$\mathrm{H_{dipole}} = \frac{\mathrm{p_x^2+p_y^2}}{2\left(1+\delta_\mathrm{p}\right)} - \frac{\mathrm{x}\delta_\mathrm{p}}{\rho} + \frac{\mathrm{x}^2}{2\rho^2}, \tag{2.36a}$$

$$\mathrm{H_{quadrupole}} = \frac{\mathrm{p_x^2+p_y^2}}{2\left(1+\delta_\mathrm{p}\right)} + \frac{\mathrm{k_q}}{2}\left(\mathrm{x}^2-\mathrm{y}^2\right), \tag{2.36b}$$

$$\mathrm{H_{sextupole}} = \frac{\mathrm{p_x^2+p_y^2}}{2\left(1+\delta_\mathrm{p}\right)} + \frac{k_s}{6}\left(x^3-3xy^2\right), \tag{2.36c}$$

$$\mathrm{H_{octupole}} = \frac{\mathrm{p_x^2+p_y^2}}{2\left(1+\delta_\mathrm{p}\right)} + \frac{k_o}{24}\left(x^4-6x^2y^2+y^4\right). \tag{2.36d}$$

For the beamline elements without the electric fields it is often more convenient to ignore the longitudinal dynamics and use the 4–D transverse phase space (x, x', y, y'), with the momentum variables ($\mathrm{p_x}$, $\mathrm{p_y}$) being replaced by the angular variables (x', y') and δ_p being a numerical constant. In such cases the Hamiltonian equations of motion hold for the Hamiltonians given in Eqs. 2.37 [35].

$$\mathrm{H_{dipole,\ 4-D}} = \frac{1}{2}\left(\mathrm{x}'^2+\mathrm{y}'^2\right) + \frac{1}{1+\delta_\mathrm{p}}\left(-\frac{\mathrm{x}\delta_\mathrm{p}}{\rho}+\frac{\mathrm{x}^2}{2\rho^2}\right), \tag{2.37a}$$

$$\mathrm{H_{quadrupole,\ 4-D}} = \frac{1}{2}\left(\mathrm{x}'^2+\mathrm{y}'^2\right) + \frac{\mathrm{k_q}}{2(1+\delta_\mathrm{p})}\left(\mathrm{x}^2-\mathrm{y}^2\right), \tag{2.37b}$$

$$\mathrm{H_{sextupole,\ 4-D}} = \frac{1}{2}\left(\mathrm{x}'^2+\mathrm{y}'^2\right) + \frac{k_s}{6(1+\delta_p)}\left(x^3-3xy^2\right), \tag{2.37c}$$

$$\mathrm{H_{octupole,\ 4-D}} = \frac{1}{2}\left(\mathrm{x}'^2+\mathrm{y}'^2\right) + \frac{k_o}{24(1+\delta_p)}\left(x^4-6x^2y^2+y^4\right). \tag{2.37d}$$

With the Lie algebra methods, the exact transfer map for each beamline element can be defined based on its Hamiltonian. Afterwards, the transfer maps of individual elements can be combined into a global transfer map for a whole beamline and the exact particle tracking can be performed.

2.2. Linear collider layout

The main parts of a linear collider will be discussed using the schematic layout of the International Linear Collider (ILC, see Section 2.5.2 for details) [36] shown in Figure 2.2.

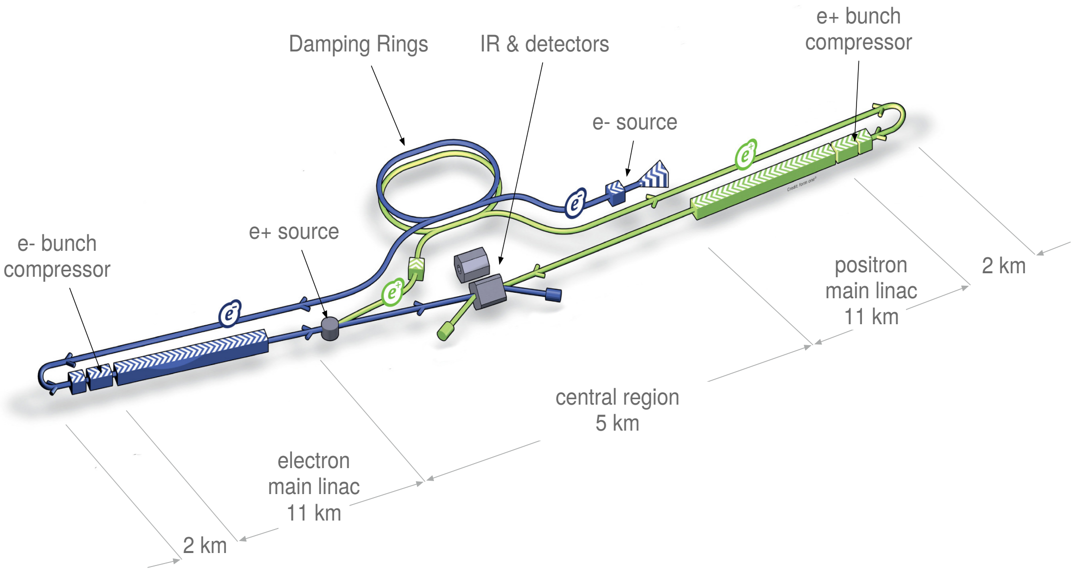

Figure 2.2: Main parts of a linear collider marked on the schematic layout of the ILC (graphics from [36]).

In general, a linear collider consists of the following subsystems:

- **Source:** produces the beam of particles, generates the particle bunches, provides initial acceleration and polarizes the beam if required. The electrons are usually generated by a laser illuminating a strained photocathode in a DC gun (see Fig. 2.3). The positrons are created using an electron beam colliding with a target to form a photon beam. The photon beam then hits another target where the electron-positron pairs are generated. Positrons are then separated from the electrons, bunched and pre-accelerated.

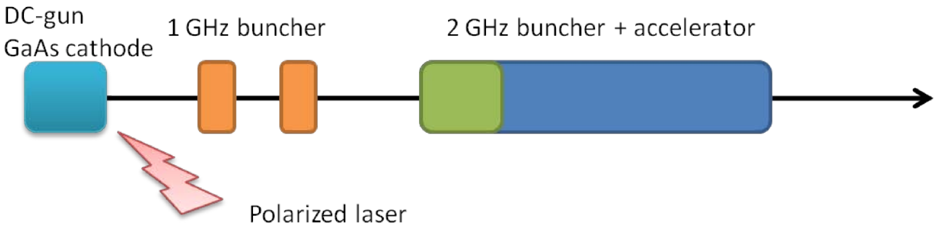

Figure 2.3: Schematic of the CLIC (see Section 2.5.1 for details) polarized electron source and bunching system (graphics from [37]).

- **Damping ring (DR):** accepts e^- and e^+ beams with large transverse emittance, which are then damped by a few orders of magnitude in order to fulfill the tight requirements of beam sizes (see Eq. 2.6). The transverse emittance damping occurs because of the synchrotron radiation (see Eq. 1.5) being emitted by the beam in the arcs and in the damping wigglers located in the straight sections of the ring. The straight sections also accommodate the accelerating cavities that compensate for the radiated energy, the injection and extraction sections and other sections used to adjust the beam phase and the ring circumference (see Fig. 2.4).

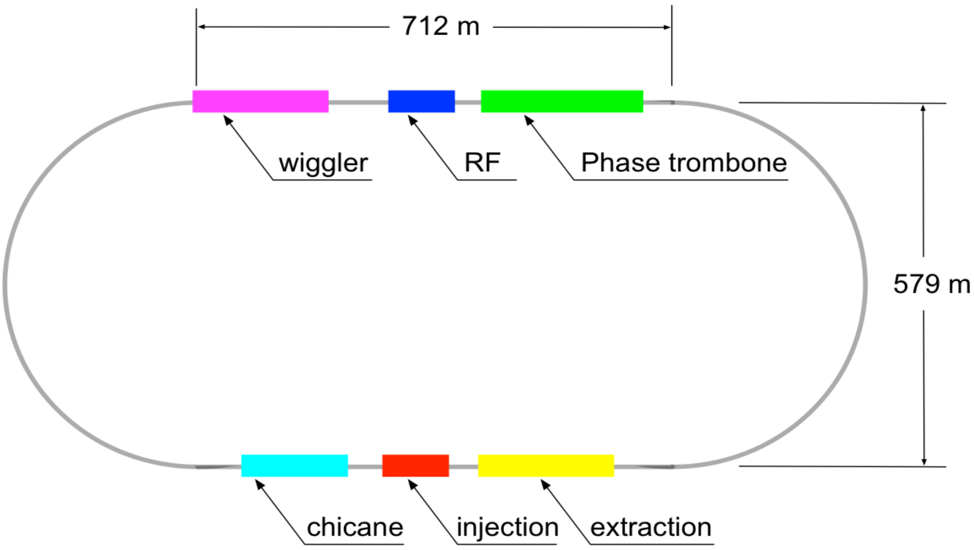

Figure 2.4: Schematic of the ILC damping ring layout (graphics from [36]).

- **Ring to main linac transport (RTML):** connects the damping rings and the main linacs. It matches bunch length and energy from the values given by the damping rings to the values required by the main linacs. It includes sections for longitudinal bunch compression, acceleration, spin rotation and collimation (see Fig. 2.5).

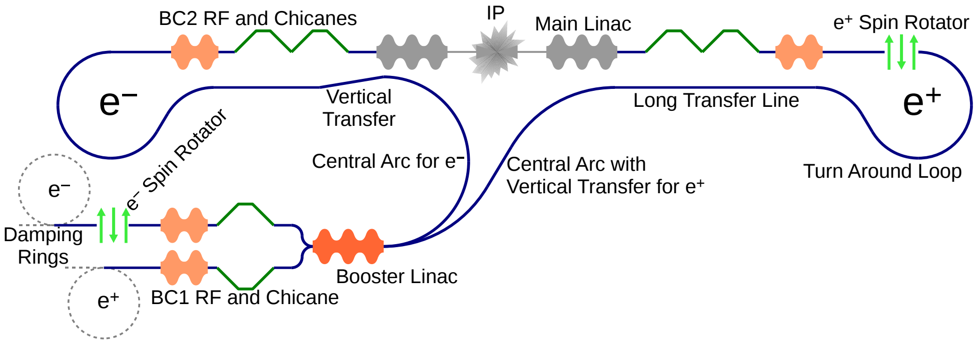

Figure 2.5: Schematic of the CLIC RTML (graphics from [38]).

- **Main linac:** accelerates the beam to the collision energy. It consists of many successive arrays of coupled radio-frequency (RF) cavities used for beam acceleration, interleaved by quadrupoles used to center the beam on axis. A very high accelerating gradient is required in order to keep the linac length short. In the case of the ILC the cavities are superconducting (see Fig. 2.6) providing an average gradient of 31.5 MV/m [36]. For CLIC the accelerating structures are normal conducting (see Fig. 2.6) and a high gradient of 100 MV/m [37] is achieved by extracting the power from the drive beams [37]. In the case of the ILC main beams and CLIC drive beams the RF energy is produced in devices called klystrons, which are powered by other devices called modulators. A klystron uses the bunching of a low energy electron beam in response to a weak input RF signal to amplify the RF energy.

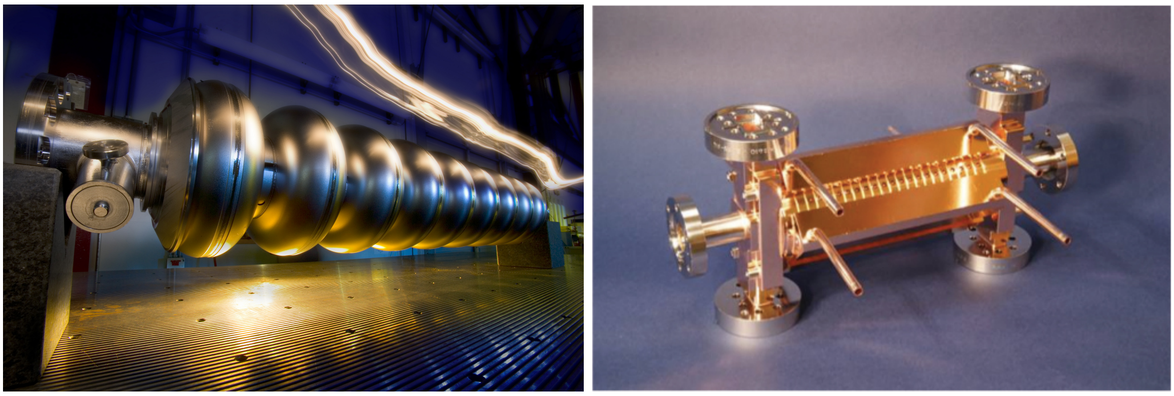

Figure 2.6: Superconducting RF cavity (left) and CLIC accelerating structure prototype (right) (graphics from [39]).

- **Beam delivery system (BDS):** transports the beam from the main linac to the interaction point (IP) and prepares the beams for collisions (see Fig. 2.7). The BDS measures the parameters of the linac beam and matches it into the final focus section. Using the collimators the BDS protects the beamline and detector against mis-steered beams from the main linacs and removes any large amplitude or off-energy particles (beam halo). It also measures and monitors the key physics parameters such as energy and polarisation. The final focus section provides the beam size demagnification typically by a factor of several hundreds to fulfill the luminosity requirements (see Eq. 1.4). The final focus system is of most interest in my study and will be described in more detail in the next section.

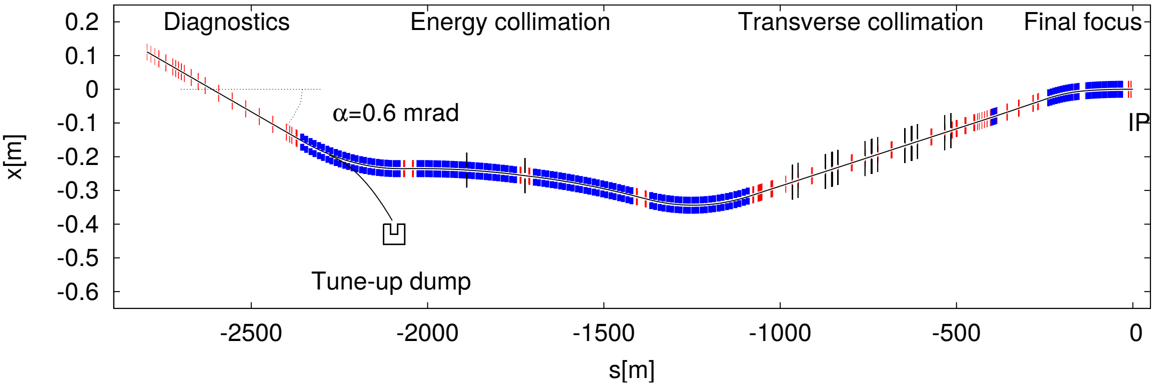

Figure 2.7: Schematic of CLIC 3 TeV BDS. Dipoles, quadrupoles and collimators are shown in blue, red and black, respectively (graphics from [37]).

2.3. Final Focus System

The final focus system (FFS) is the last part of the beam delivery system of a linear collider. Its main task [40, 41] is to demagnify the beam to the small sizes required at the interaction point (IP). This is achieved by forming a large and almost parallel beam at the entrance of the final doublet (FD), which consist of two strong quadrupole lenses. The beam is then focused by the FD, where the demagnification factor is usually on the order of several hundreds. However, for strong focusing even a small deviation in the particle's momentum causes a smearing of the focal point and therefore an effective beam size growth at the IP. This effect, by analogy to the conventional optics, is called chromaticity and requires correction.

The main part of this thesis is devoted to studying the FFS performance in the case of strong beam focusing and large chromaticity values. Therefore the chromaticity will be described in more detail including the two most common correction methods. Other effects associated with the FFS will be also discussed.

2.3.1. Chromaticity

As presented in Fig. 2.8 only the on-momentum particles are focused exactly at the focal point, while the off-momentum particles with higher or lower momentum are under-focused or over-focused, respectively. This effect, called chromaticity, produces a variation in the transverse position at the focal point increasing the beam size.

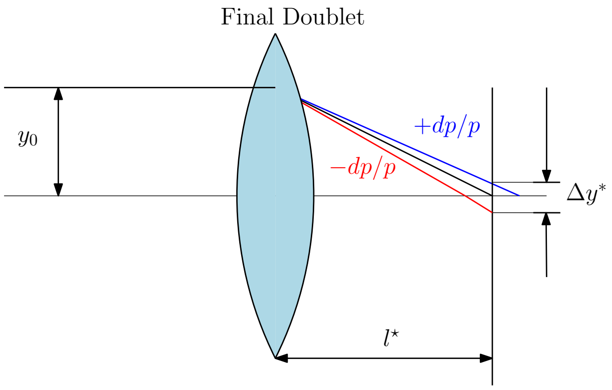

Figure 2.8: Chromaticity. Particles with off-momentum energy are focused at different longitudinal locations increasing the beam size (graphics from [34]).

The chromaticity effect on the particle position can be approximated as:

$$\frac{\Delta y^*}{\sigma^*_{y,0}} \approx \frac{l^*}{\beta^*_y}\sigma_\delta \approx \xi_y \sigma_\delta, \tag{2.38}$$

where ξ_y stands for the chromaticity, σ_δ is the second moment of the beam energy, β_y^* is the optical vertical beta function at the IP and $\sigma_{y,0}^*$ is the transverse beam size at the IP in the case of zero energy spread. Chromaticity created by a single quadrupole can be expressed as:

$$\xi_{x,y} = \int \beta_{x,y}(s)K(s)ds, \tag{2.39}$$

where K(s) is the strength of the quadrupole and $\beta_{\mathrm{x,y}}$ are the horizontal or vertical beta function at the quadrupole location. The chromatic dilution of the vertical beam size can be approximated as:

$$\sigma_y^* \approx \sigma_{y,0}^* \sqrt{1+\xi_y^2\sigma_\delta^2}, \tag{2.40}$$

which for strong focusing can be very large, even several hundred times the nominal beam size. The chromaticity can be also expressed using the transfer map formalism. For a Gaussian energy distribution of the beam:

$$\xi_y^2 = \frac{1}{\beta_y^*}\left(X_{y,00101}^2\beta_{y,0} + X_{y,00011}^2\frac{1}{\beta_{y,0}}\right), \tag{2.41}$$

where X_y are the coefficients of the transfer map given by Eq. 2.18 between the beginning of the beamline and the IP and $\beta_{y,0}$ and β_y^* are the vertical beta functions at the starting point and at the IP.

2.3.2. Chromaticity correction

The most common concept of the chromaticity correction is presented in Fig. 2.9. It is based on segregating the particles spatially according to their momentum using the dispersion created by a dipole magnet. A beam prepared this way can then be focused at the focal point using the nonlinear field of the sextupole magnet.

Let us consider an example with one quadrupole and one sextupole. We assume the thin lens approximation is valid, i.e. the particle position does not change within the element. Therefore, by neglecting the terms with x' and y', and for small values of δ_p we get the following expressions for the Hamiltonians (see Eqs. (2.37)):

$$\mathrm{H_q} = \frac{1}{2}\mathrm{k_q}(\mathrm{x}^2-\mathrm{y}^2) - \frac{1}{2}\mathrm{k_q}\delta_\mathrm{p}\left(\mathrm{x}^2-\mathrm{y}^2\right), \tag{2.42a}$$

$$\mathrm{H_s} = \frac{1}{3!}\mathrm{k_s}\left(\mathrm{x}^3-3\mathrm{xy}^2\right). \tag{2.42b}$$

The spatial segregation of the particles with different momentum using the dispersion created

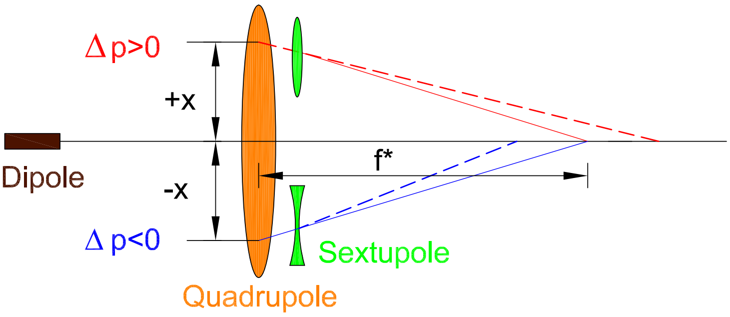

Figure 2.9: Scheme of the chromaticity correction using a sextupole magnet (represented by green lenses) located at a region of non-zero dispersion created by a dipole magnet (brown). The particles are sorted according to their momentum such that they experience the focusing or defocusing effect of a sextupole, depending on their momentum. Dashed lines represent particle trajectories without chromaticity correction while continuous lines represent particle trajectories corrected for chromaticity (graphics from [18]).

by the bending magnet can be interpreted as a change of coordinates:

$$x \to x + \eta_x \delta_p, \tag{2.43a}$$

$$y \to y, \tag{2.43b}$$

where η_x is the horizontal dispersion at the sextupole location.

First, we consider a case with a single sextupole in a dispersive region, and a quadrupole in a zero-dispersion region. The Hamiltonians from Eq. (2.42) can be rewritten:

$$H_q = \frac{1}{2}k_q(x^2 - y^2) - \frac{1}{2}k_q\delta_p\left(x^2 - y^2\right), \tag{2.44a}$$

$$H_s = \frac{1}{3!}k_s\left(x^3 - 3xy^2\right) + \frac{1}{2}k_s\eta_x\delta_p\left(x^2 - y^2\right) + \frac{1}{2}\eta_x^2\delta_p^2 x + \frac{1}{3!}\eta_x^3\delta_p^3. \tag{2.44b}$$

The expressions (2.44a) and (2.44b) can be merged in one single Hamiltonian using the BCH formula. Since we have assumed no dependence on the momentum the terms $\left[H_q, H_s\right]$ vanish and the single Hamiltonian is just the sum of the quadrupole and the sextupole Hamiltonian $H = H_q + H_s$. The chromatic term in Eq. (2.44a) is canceled by the second term in Eq. (2.44b) if we take $k_q = k_s\eta_x$. What remains are the focusing term from the quadrupole $\frac{1}{2}k_q\left(x^2 - y^2\right)$, a geometric term from the sextupole $\frac{1}{3!}k_s\left(x^3 - 3xy^2\right)$ that can be compensated using another sextupole with opposite phase in non-dispersive location, a second order dispersion term $\frac{1}{2}\eta_x^2\delta_p^2 x$ and a purely chromatic term $\frac{1}{3!}\eta_x^3\delta_p^3$ that has no effect on the dynamics of the particles.

We can now also consider the case with a quadrupole in the dispersive location. For the dispersion value η_x the quadrupole Hamiltonian is:

$$H_q = \frac{1}{2}k_q(x^2 - y^2) - \frac{1}{2}k_q\delta_p\left(x^2 - y^2\right) + k_q\eta_x\delta_p x - k_q\eta_x\delta^2 x + \frac{1}{2}k_q\eta_x^2\delta_p^2 - \frac{1}{2}k_q\eta_x^2\delta_p^3. \quad (2.45)$$

The last two terms can be neglected as they have no dependence on the coordinates and therefore they do not affect the particle dynamics. The second order dispersion term $-k_q\eta_x\delta^2 x$ appears, which is half compensated with the second order dispersion term coming from the sextupole. This term can be fully compensated if the sextupoles double their strength but then an overcompensation of the chromaticity appears. Therefore, the entire chromaticity of the FFS must be generated upstream of the FD in a non-dispersive location.

The two considered cases of chromaticity compensation are reflected in two different layouts of the FFS. One, called dedicated (or traditional), has two dedicated chromaticity correction sections, one for each plane. The second scheme is called local, because the chromaticity is corrected close to its origin by the sextupoles adjacent to the FD quadrupoles. Both approaches are described in the next two sections.

Dedicated chromaticity correction

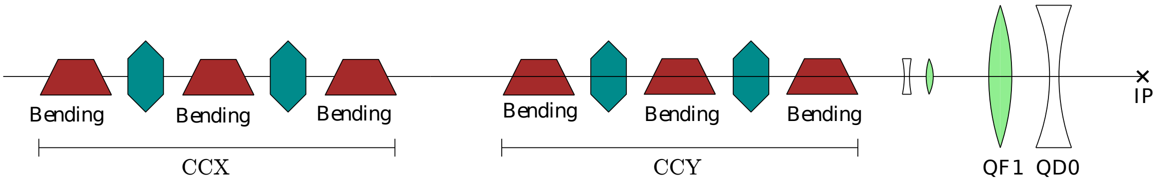

Figure 2.10: Schematic layout of the dedicated chromaticity correction scheme (graphics from [34]).

The dedicated chromaticity correction scheme of the FFS consists of two sections for chromaticity compensation, one for the horizontal (CCX) and one for the vertical (CCY) plane, located upstream from the final doublet (see Fig. 2.10). Both chromaticity correction sections have symmetric optics with large beta function and a maximum of the dispersion function in the location of the sextupoles. The geometric aberrations generated by the sextupoles are canceled by using the $-I$ transfer matrix between the sextupoles.

The simplicity of the dedicated chromaticity correction scheme is its main advantage. The correction for each plane are separated and can be better controlled which makes such FFS easier to operate [34]. However, such a design is rather long which increases its cost. Moreover, the chromatic compensation is done far away from the final doublet which is the main chromaticity source. Additionally, numerous bending magnets can lead to a larger rate of synchrotron radiation which affects the correction efficiency. Such chromaticity compensation was implemented in the Final Focus Test Beam (FFTB, details in Section 2.5.3) at SLAC [42]. It is also considered as a possible solution for CLIC.

Local chromaticity correction

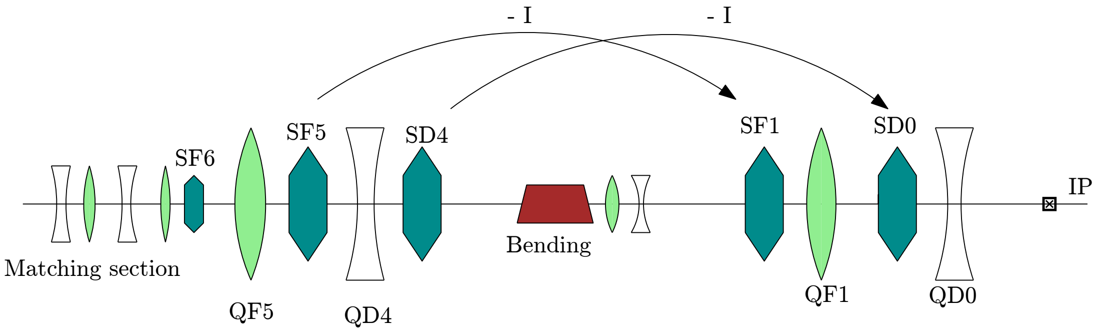

Figure 2.11: Schematic layout of the local chromaticity correction scheme (graphics from [34]).

A new design based on a local correction of chromaticity was proposed in 2001 [43]. In this case chromaticity is corrected by two sextupole magnets adjacent to the FD quadrupoles (see Fig. 2.11). The required dispersion is created only once using a bending magnet located upstream from the FD and serves for correcting both horizontal and vertical planes. The parasitic second order dispersion is canceled locally assuming half of the horizontal chromaticity arriving from upstream of the FD. Two more sextupoles located upstream from the bending magnet cancel the geometric aberrations introduced by the FD sextupoles. The higher order aberrations are corrected by optimizing the transfer matrices between the sextupoles.

The local chromaticity correction scheme is much shorter than the dedicated scheme [43] and therefore cheaper. Moreover, the energy bandwidth of the local compensation was found to be better compared to the non-local method. On the other hand, the local scheme is more complex as it performs the correction in two planes at the same time and requires good quality first order optics to cancel the high order aberrations. A recipe for designing the final focus system based on the local chromaticity correction scheme is described in [44]. This scheme was implemented in the Accelerator Test Facility 2 (ATF2, details in Chapter 3) and is considered as a baseline for the ILC and a possible solution for CLIC.

2.3.3. Final Focus System limitations

Beam-beam effects

There is a significant electromagnetic interaction between the two beams crossing at the IP which modifies the dynamics of the particles [45]. The magnitude of the beam-beam effects is characterized by the disruption parameter $\mathrm{D_{x,y}}$ defined as a ratio between the rms bunch length σ_z and the effective focal length $\mathrm{f_{x,y}}$ [46]:

$$\mathrm{D_{x,y}} \equiv \frac{\sigma_\mathrm{z}}{\mathrm{f_{x,y}}} = \frac{2\mathrm{N_p r_e}\sigma_\mathrm{z}}{\gamma\sigma^*_\mathrm{x,y}\left(\sigma^*_\mathrm{x}+\sigma^*_\mathrm{y}\right)}, \tag{2.46}$$

where $\mathrm{N_p}$ stands for the number of particles per bunch, γ is the relativistic Lorentz factor and $\mathrm{r_e}$ denotes the classical electron radius. For a small value of the disruption parameter the beam acts like a thin lens but for the focal length being shorter than the bunch length there is a pinch enhancement leading to instabilities that can reduce the luminosity in the presence of beam offsets.

The focusing effect of the opposite beam causes an emission of synchrotron radiation called beamstrahlung. The number of emitted photons is given by the following approximation:

$$N_\Upsilon \approx 2\frac{\alpha r_e N_p}{(\sigma_x+\sigma_y)}, \tag{2.47}$$

where $\alpha \approx 1/137$ is the fine structure constant. The beamstrahlung effect can be minimized by keeping the term $\left(\sigma^*_\mathrm{x}+\sigma^*_\mathrm{y}\right)$ large. On the other hand, the product $\left(\sigma^*_\mathrm{x}\sigma^*_\mathrm{y}\right)$ has to be kept low to achieve the required luminosity (Eq. 1.3). The common solution is that the beams in a linear collider are flat ($\sigma^*_\mathrm{x} \gg \sigma^*_\mathrm{y}$) so that the number of beamstrahlung photons depends mainly on the horizontal beam size.

Hourglass effect

The transverse beam size is usually considered without including the longitudinal properties of the beam. However, because of the high beam divergence in a low β region near the IP, the transverse beam size depends on the longitudinal position s:

$$\sigma_\mathrm{x,y}(\mathrm{s}) = \sigma^*_\mathrm{x,y}\sqrt{1+\left(\frac{\mathrm{s}}{\beta^*_\mathrm{x,y}}\right)^2}. \tag{2.48}$$

For this reason the bunch length should not be larger than β^*_y value ($\sigma_\mathrm{z} \lesssim \beta^*_\mathrm{y}$) in order to avoid luminosity loss [47].

Oide effect

The focusing strength of quadrupole magnets, especially the final doublet, is limited by the synchrotron radiation emitted when the particle's trajectory is bent within a quadrupole [48, 49].

Such phenomenon is called the Oide effect. The minimum vertical beam size at the IP assuming the Oide effect is given by a following expression:

$$\sigma_{\mathrm{y}}^{*2} = \beta_{\mathrm{y}}^{*}\varepsilon_{\mathrm{y}} + \frac{110}{3\sqrt{6\pi}}\mathrm{r_e}\lambda_{\mathrm{e}}\gamma^5\mathrm{F}\left(\sqrt{\mathrm{K}}\mathrm{L},\sqrt{\mathrm{K}}\mathrm{l}^*\right)\left(\frac{\varepsilon_{\mathrm{y}}}{\beta_{\mathrm{y}}^{*}}\right)^{5/2}, \tag{2.49}$$

where the function $\mathrm{F}\left(\sqrt{\mathrm{K}}\mathrm{L},\sqrt{\mathrm{K}}\mathrm{l}^*\right)$ is defined by:

$$\begin{aligned} &\mathrm{F}\left(\sqrt{\mathrm{K}}\mathrm{L},\sqrt{\mathrm{K}}\mathrm{l}^*\right) \equiv \\ &\equiv \int_0^{\sqrt{\mathrm{K}}\mathrm{L}} \left|\sin\phi + \sqrt{\mathrm{K}}\mathrm{l}^*\cos\phi\right|^3 \left[\int_0^{\phi}\left(\sin\phi' + \sqrt{\mathrm{K}}\mathrm{l}^*\cos\phi'\right)^2 \mathrm{d}\phi'\right]^2 \mathrm{d}\phi \end{aligned} \tag{2.50}$$

and L stands for the quadrupole length, l^* for the last drift length, K for the quadrupole strength, $\mathrm{r_e}$ for the electron classical radius, λ_e for the Compton wavelength of the electron and γ is the relativistic factor. The Oide effect can be minimized by making the FD quadrupoles longer.

Crossing angle

The head-on collisions of bunches are desired in a linear collider but it is necessary to introduce some crossing angle between the beams to clearly extract the spent beam and to avoid interactions between the in-going and out-going bunches. For beams without pinch effect the luminosity loss for a crossing angle α is given by [50]:

$$\frac{\mathrm{L}}{\mathrm{L_0}} = \frac{1}{\sqrt{1+\left(\frac{\sigma_{\mathrm{z}}}{\sigma_{\mathrm{x}}}\tan\frac{\alpha}{2}\right)}}, \tag{2.51}$$

where σ_{z} and σ_{x} are the longitudinal and horizontal beam sizes. Crab cavities can be used to rotate the bunches and therefore restore the luminosity [51].

2.4. Beam size at the interaction point

One of the main roles of the final focus system is to demagnify the beam such that it reaches a small size at the interaction point. In an ideal case the IP beam size (see Eq. 2.6) depends only on the $\beta^*_{\mathrm{x,y}}$ and $\varepsilon^*_{\mathrm{x,y}}$ values. In practice, the beam dynamic's imperfections (e.g. non-zero dispersion, chromaticity, stability, etc.) make the actual IP beam size larger. Assuming the Gaussian particle distribution of the beam in all 6 coordinates, the contribution of the beam size from different sources add in quadrature, i.e.:

$$\sigma^{*}_{\mathrm{x,y}} = \sqrt{\varepsilon_{\mathrm{x,y}}\beta^{*}_{\mathrm{x,y}} + \eta^{*2}_{\mathrm{x,y}}\sigma^{2}_{\delta} + \xi^{2*}_{\mathrm{x,y}}\sigma^{2}_{\delta} + \sigma^{*2}_{\mathrm{x,y;err}}}\,, \tag{2.52}$$

where $\sigma^{*2}_{\mathrm{x,y;err}}$ represents other independent sources of the IP beam size growth and the rest of the symbols were already defined. During the process of the FFS design and optimisation the IP beam size is often calculated using the particle distribution at the IP obtained e.g. from the numerical computations. In the scope of this thesis, three following definitions of beam size were used:

- core (σ_{core}): Defined as a spread of the Gaussian distribution fitted to the histogram of particle positions. The beam size error is given by the error of the fit. This definition has a special relevance to the calculation of the luminosity.
- Shintake (σ_{Shi}): Calculated from the convolution between the distribution of beam particles and the distribution of photons in the interference pattern created by the Shintake monitor [52, 53]. The Shintake monitor (details in Section 3.5) is currently the only device capable of measuring the electron beam size with a nanometre precision. The algorithm for calculating the beam size according to the Shintake definition is described in [18]. This definition was used in the studies described in the Chapter 5.
- rms (σ_{rms}): The beam size is calculated according to the rms definition (see Eq. 2.6 and Section 2.1.2). This definition was used in the studies described in Chapter 4.

The usual relation between the three definitions is the following:

$$\sigma_{\mathrm{core}} \leq \sigma_{\mathrm{Shi}} \leq \sigma_{\mathrm{rms}}. \tag{2.53}$$

It comes from the fact that the σ_{core} definition almost neglects the tails of the particle distribution, while the σ_{rms} is strongly affected by the tails. The equalities in the above relation hold when the beam is represented by a Gaussian distribution for all coordinates.

2.5. Linear collider projects

There are two main proposals for a linear $\mathrm{e}^{+}\mathrm{e}^{-}$ collider: the Compact Linear Collider (CLIC) and the International Linear Collider (ILC), both described in more detail in the next two sections.

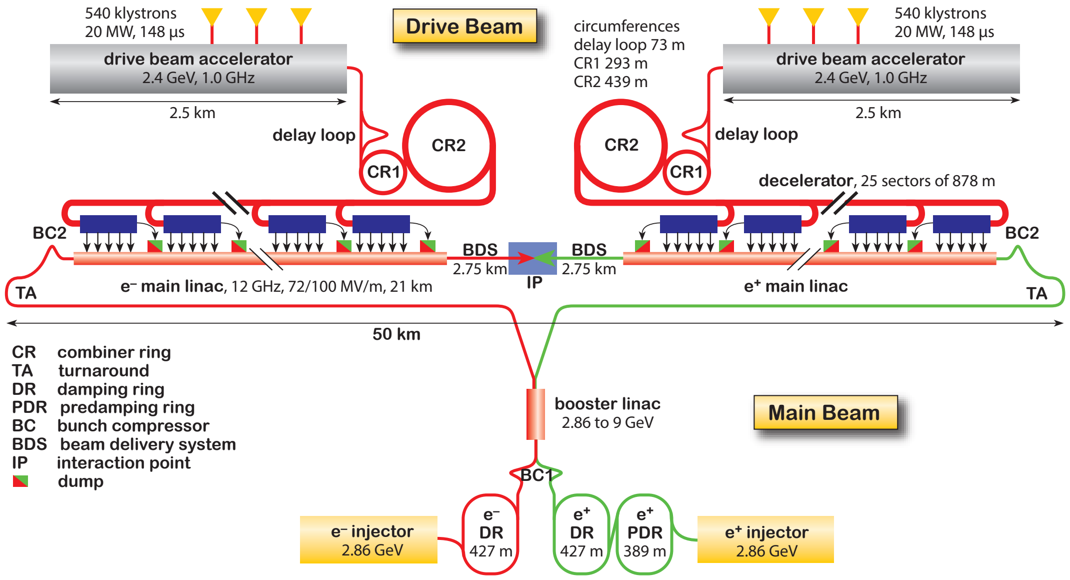

Figure 2.12: Schematic of the CLIC layout at $\sqrt{s} = 3$ TeV (graphics from [19]).

2.5.1. The Compact Linear Collider (CLIC)

The Compact Linear Collider (CLIC) [19, 37, 54, 55] is a design of a linear collider developed at CERN aiming to collide electrons with positrons at a centre-of-mass energy of $\sqrt{s} = 3$ TeV with a luminosity of about $6 \cdot 10^{34} \mathrm{cm}^{-2}\mathrm{s}^{-1}$. The main novelty of CLIC is a two beam acceleration scheme featuring an unprecedentedly high accelerating gradient of about 100 MV/m. The RF power for acceleration is extracted from a low energy and high intensity drive beam and fed into the main beam using the Power Extraction and Transfer Structures (PETS, see Fig. 2.6). Such a high accelerating gradient allows us to reach large collision energies while keeping a reasonable length of the machine.

CLIC is foreseen to be built in three stages [19] in terms of the centre-of-mass energy. The first stage with $\sqrt{s} = 380$ GeV and the second stage with $\sqrt{s} = 1.5$ TeV can be realized using only one drive beam complex. For the third stage with $\sqrt{s} = 3$ TeV the two drive beam complexes are needed. The schematic layouts of the CLIC accelerator complex at 3 TeV is shown in Figure 2.12. The main parameters of all the three stages are given in Table 2.1. The physics potential of a machine like CLIC was discussed in the Section 1.3.

2.5.2. The International Linear Collider (ILC)

The International Linear Collider (ILC) [36] is a linear collider design proposed to be built in Japan with a centre-of-mass energy tunable from 200 to 500 GeV and possible upgrade up to 1 TeV. The ILC is based on 1.3 GHz superconducting RF cavities (see Fig. 2.6) with

Table 2.1: Parameters for the CLIC energy stages [19].

Parameter	Symbol	Stage 1	Stage 2	Stage 3
Centre-of-mass energy	$\sqrt{s}$ [GeV]	380	1500	3000
Repetition frequency	f_{rep} [Hz]	50	50	50
Number of bunches per train	n_b	352	312	312
Bunch separation	Δt [ns]	0.5	0.5	0.5
Accelerating gradient	G [MV/m]	72	72/100	72/100
Total luminosity	$\mathscr{L}$ $[10^{34}\frac{1}{cm^2 s}]$	1.5	3.7	5.9
Main tunnel length	[km]	11.4	29.0	50.1
Number of particles per bunch	N $[10^9]$	5.2	3.7	3.7
Bunch length	σ_z [μm]	70	44	44
IP beam size	σ_x/σ_y [nm]	149/2.9	$\sim$ 60/1.5	$\sim$ 40/1
Norm. emitt. (at IP)	$\varepsilon_x/\varepsilon_y$ [nm]	950/30	—	—
Estimated power consumption	P_{wall} [MW]	252	364	589

an accelerating gradient of 31.5 MV/m. The main advantage of the ILC is that it provides the electron beam with 80% polarisation and the positron beam with 60% polarisation which improves its physics potential. Furthermore, alternative options for photon-photon and electron-electron collisions are under consideration. The schematic layout of the ILC is presented in Figure 2.2 and Table 2.2 shows the main ILC parameters.

Table 2.2: ILC design parameters for the 500 GeV centre-of-mass energy program [36].

Parameter	Symbol	ILC
Centre-of-mass energy	$\sqrt{s}$ [GeV]	500
Repetition frequency	f_{rep} [Hz]	5
Number of bunches per train	n_b	1312
Bunch separation	Δt [ns]	554
Accelerating gradient	G [MV/m]	31.5
Total luminosity	$\mathscr{L}$ $[10^{34}\frac{1}{cm^2 s}]$	1.8
Site length	[km]	31
Number of particles per bunch	N $[10^9]$	20
Bunch length	σ_z [μm]	300
IP beam size	σ_x/σ_y [nm]	474/5.9
Norm. emitt. (at IP)	$\varepsilon_x/\varepsilon_y$ [nm]	10000/35

2.5.3. Test Facilities

Several test facilities have been built to study the feasibility of the linear colliders. The following is a brief description of the most important test facilities.

Final Focus Test Beam

The Final Focus Test Beam (FFTB) [42, 56, 57] was built and operated during the 90's at SLAC. It was an experimental final focus line based on the dedicated chromaticity correction scheme. The FFTB was located at the end of the SLAC linac delivering the electron and positron beams with an energy of 46.6 GeV. The smallest vertical beam size in FFTB of 70 ± 7 nm was measured after relaxing the horizontal focusing to reduce the background signal in May 1994 [56, 57].

CLIC Test Facility 3 (CTF3)

The CLIC Test Facility 3 (CTF3) was built at CERN to demonstrate the generation of a high intensity beam and to test the two-beam acceleration concept [58, 59]. The required intensity of a drive beam is obtained by combining the beam trains in a delay loop (intensity multiplied by a factor 2) and afterwards in a combiner ring (intensity multiplied by a factor 4). After the recombination the beam is sent to two different experiments: the Two-Beam Test Stand (TBTS) where the two-beam acceleration system is tested and a second experiment designed to show the stable and efficient transport of a decelerated beam.

Accelerator Test Facility (ATF)

The Accelerator Test Facility (ATF) is a linear collider test facility located at KEK, Japan. The whole of Chapter 3 is devoted to describing the ATF, where all experimental studies included in this thesis were performed.

Chapter 3

The Accelerator Test Facility

The Accelerator Test Facility (ATF) [60] is an accelerator at the High Energy Accelerator Research Organisation (KEK) [61] in Tsukuba, Japan. The ATF is designed as an R&D platform for future linear accelerators, in particular the ILC. With beam operation starting in 1997, the original goal of the facility was to achieve the extremely low vertical emittance beam required for linear colliders. The design parameters were achieved in 2001 [62, 63].

The ATF accelerator facility is composed of a photocathode giving electrons to a linac accelerating the particles to 1.3 GeV followed by a damping ring (see Fig. 3.1).

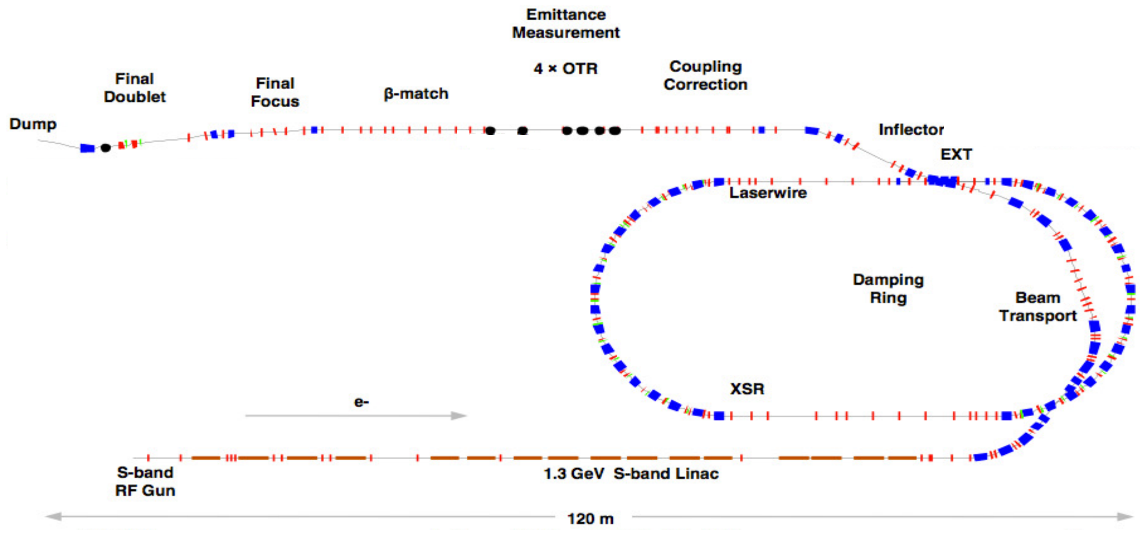

Figure 3.1: Schematic layout of the Accelerator Test Facility.

In 2008 the facility was upgraded to the ATF2 project [64]. The existing machine was extended with a 100 m beam delivery system consisting of an extraction line and final focus line which are an energy-scaled version of the FFS designed for the ILC (see Fig. 3.2). The goals of the ATF2 project are to achieve a 37 nm vertical beam size at the IP (**goal 1**) and to stabilize the IP beam position at the level of few nanometers (**goal 2**) [64]. The main ATF2 design parameters are given in Table 3.1.

The ATF subsystems are described in detail in the next sections. A special emphasis is given to the ATF2 line where the experimental part of my work was conducted.

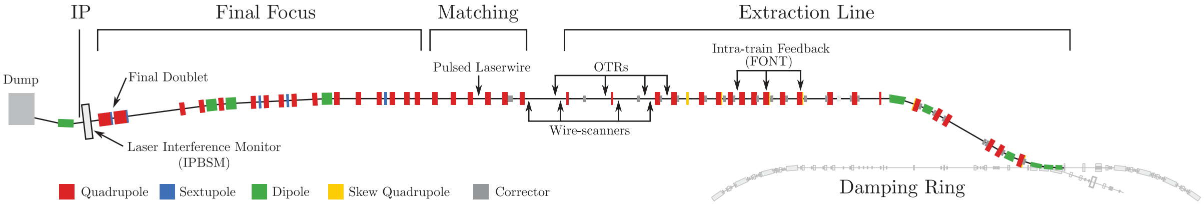

Figure 3.2: Schematic layout of the ATF2 section.

Table 3.1: ATF2 design parameters.

Parameter	**Symbol**	**ATF2 design**
Beam energy	$\sqrt{s}$ [GeV]	1.3
Energy spread	σ_δ [%]	[0.06,0.08]
Final quad to IP distance	L^* [m]	1
Normalized horizontal emittance	$\varepsilon_{x,N}$ [μm]	2.8
Normalized vertical emittance	$\varepsilon_{y,N}$ [nm]	31
Horizontal emittance	ε_x [nm]	2
Vertical emittance	ε_y [pm]	12
Horizontal β function at the IP	β_x^* [mm]	4
Vertical β function at the IP	β_y^* [μm]	100
Horizontal beam size at the IP	σ_x^* [μm]	2.8
Vertical beam size at the IP	σ_y^* [nm]	37
Natural vertical chromaticity	ξ_y	10000

3.1. Source and linac

The 88 m long ATF linac consists of an 18 m long 80 MeV pre-injector section and a 70 m long regular accelerator section with energy compensation structures. The RF gun with a 1.6 cell S-Band CsTe photocathode driven by a multi-bunch UV laser generates an electron beam with intensities up to 3.2 nC per bunch. Eight RF units of accelerating gradient of 35.2 MeV/m are used to accelerate the particle trains containing up to 20 bunches of up to 2×10^{10} particles per bunch. The beam energy at the linac exit is tunable up to a maximum energy of 1.54 GeV, while 1.3 GeV is the usual beam energy in recent operation. The linac is operated at a repetition rate of 25 pps (pulses per second) to accommodate 5 circulating bunch trains in the damping ring. The main parameters of the ATF injector linac are shown in Table 3.2 [60].

Beam energy, E_{beam}	≤ 1.54GeV
Bunch population, N	$\leq 2\times10^{10}$
Bunches per train, N_b	≤ 20
Bunch spacing, Δt_{bunch}	2.8 ns
Energy spread Full Width, σ_δ	$<1.0\%$ (90% beam)
Normalized emittance, $\varepsilon_{\text{Nx,y}}$	$<3\times10^{-4}$ m

Table 3.2: Basic design parameters of the ATF injector linac.

3.2. Damping ring

The ATF damping ring (DR) is a race-track shaped storage ring with an 138.6 m circumference. The ring arcs are based on the FOBO type cells, where B stands for a combined function bending magnet with horizontal defocusing. The dispersion function is minimised in the bending magnet (see Fig. 3.3) which helps in reaching a small equilibrium emittance [65]. The beam energy loss due to the synchrotron radiation is compensated by the 714 MHz RF cavity giving 330 harmonic numbers and 165 buckets with 2.8 ns spacing.

According to the results reported in [63], a vertical normalized emittance of 1.5×10^{-8} m (6 pm of geometrical emittance) was measured in 2004 for a bunch intensity of 10^{10} particles. It was achieved by a precise alignment of components and beam control. The usual values of the horizontal and vertical DR geometrical emittance in recent beam operation periods are <2 nm and <10 pm, respectively. The X-ray Synchrotron Radiation (XSR) monitor [66] is used in the damping ring to measure the beam size and therefore reconstruct the emittance. The selected parameters of the ATF damping ring are summarized in the Table 3.3.

Circumference	138.6 m
RF frequency	714 MHz
Momentum compaction factor	0.00214
Tune (x/y)	15.17/8.56
Damping time (x/y/z)	17/27/20 ms
Normalized emittance (x/y)	2.8×10^{-6} / 1.0×10^{-8} m
Geometrical emittance (x/y)	1.1×10^{-9} / 4.0×10^{-12} m

Table 3.3: Parameters and achieved performance of the ATF damping ring [65]

3.3. Extraction line

The beam is horizontally extracted from the damping ring straight section using a pulsed kicker (KEX1) and a current-sheet septum magnet (BS1X). The septum magnet is followed by two

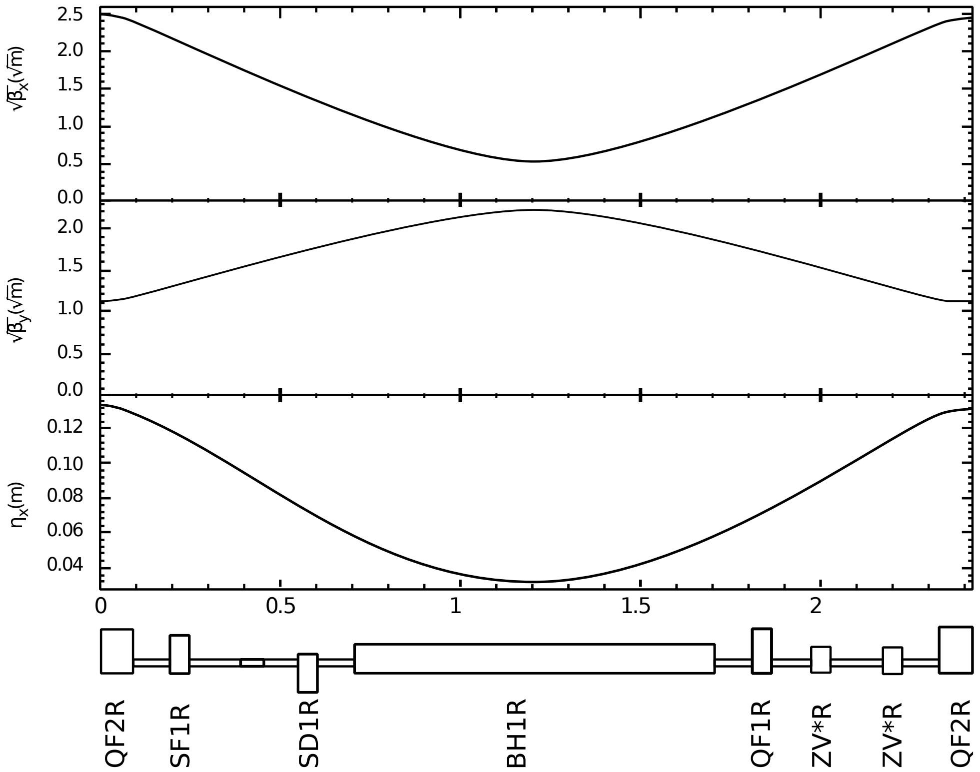

Figure 3.3: Optical functions of a damping ring cell (graphics from [60]).

strong dipole magnets (BS2X and BS3X) that bend the extracted beam at an angle of about 20°. Due to undesired magnetic components in the kicker and two DR quadrupoles (QM6R and QM7R) that the extracting beam passes through with a large offset, an x-y beam coupling occurs leading to vertical emittance growth at the extraction location [65].

A *dogleg* inflector is located downstream from the septum dipoles comprising two approximately 10° bends (BH1X and BH2X) that offset the beam by 6 m from the damping ring. The beam is brought parallel to the damping ring straight section by a mirror image of the kicker-septum system composed of two dipole magnets (BH3X and BKX). The BKX dipole replaces the KEX2 kicker that was initially installed in the extraction line. The layout of the inflector system is depicted in Fig. 3.4.

The optics of the inflector (see Fig. 3.4) provide a "pseudo -I" transformation ($\Delta\mu_x = 180°, R_{21} \neq 0$) between the DR extraction kicker and BKX dipole magnet at the end of the inflector. The inflector optics is symmetric about its midpoint in order to minimize the dispersion controlled by two strong quadrupole magnets (QF1X and QF6X). In addition, the midpoint-symmetric optics allows us to place two skew-quadrupoles (QS1X and QS2X) in two locations (near QF1X and QF6X) with the largest dispersion, equal in magnitude and opposite in sign, and with $\beta_x = \beta_y$. Such a configuration allows the two skew-quadrupoles to generate pure vertical dispersion without x-y coupling when they are powered with equal amplitude and polarity (the Σ-knob) and pure x-y coupling without vertical dispersion when they are powered

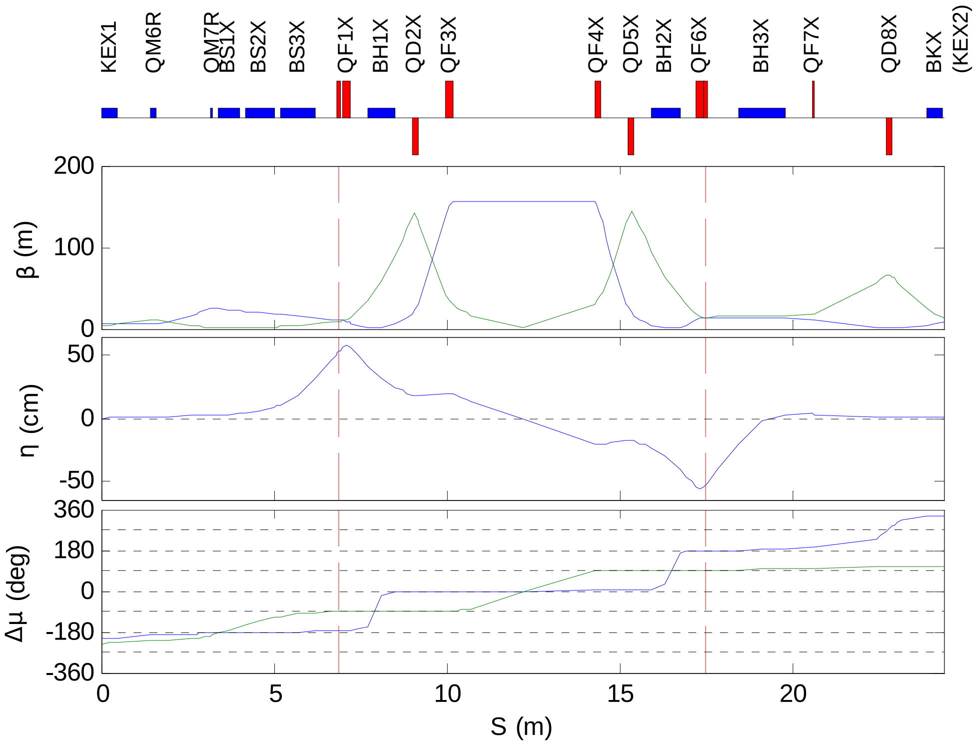

Figure 3.4: Optics of the inflector, horizontal functions are in blue and vertical functions are in green. Upper plot: β function; middle plot: dispersion function; lower plot: phase advance relative to the center of the inflector. Red vertical lines indicate the position of the skew-quadrupoles QS1X and QS2X (graphics from [65]).

with equal amplitude and opposite polarity (the Δ-knob). Almost all inflector quadrupoles are at a common betatron phase (modulo 180°) so any anomalous vertical dispersion created by quadrupole rotational errors in the inflector can be corrected using the Σ-knob. However, any anomalous vertical dispersion that originates at a different phase (i.e. coming from the DR) cannot be corrected by the inflector and requires additional correction.

Downstream from the inflector is the x-y coupling correction section consisting of four skew-quadrupoles with appropriate betatron phase advance to make the effects of the skew-quadrupoles orthogonal. The required conditions are that the first and second and also the third and fourth skew-quadrupoles are separated by 90° of phase advance in both planes, and the second and third skew-quadrupoles are separated by 180° in a horizontal plane and 90° in a vertical plane. In consequence, the first skew-quadrupole controls the x-y phase, the second controls the x'-y' phase, the third the x'-y phase, and the fourth the x-y' phase. The inflector optics are depicted in Fig. 3.5.

The coupling correction section is followed by the emittance diagnostic section. Because of tight space constraints, the optics for this system is a short, modified FODO structure. The transverse beam emittances are reconstructed by measuring the transverse beam sizes using four Optical Transition Radiation (OTR) monitors [67]. These monitors provide fast single-shot

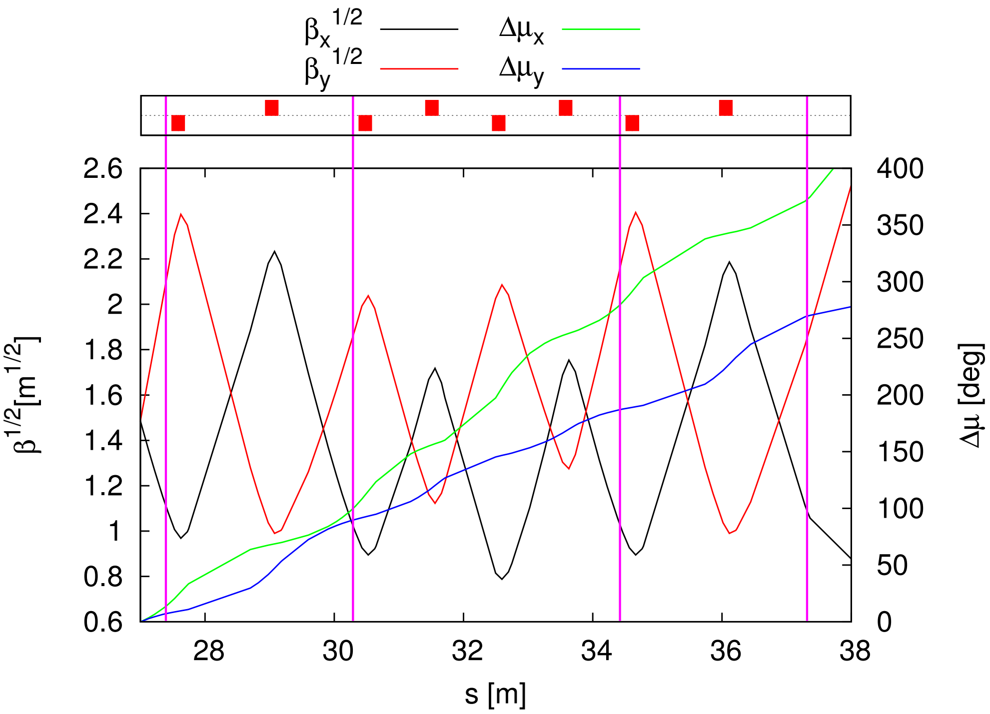

Figure 3.5: Optics of the coupling correction section. Skew-quadrupoles locations are indicated by vertical magenta lines. The red boxes at the top indicate the locations of the normal quadrupoles.

measurements with full ellipse-fitting, allowing simultaneous measurement of the projected x and y spot sizes and the x-y tilt of the beam. Beam sizes at the measurement locations for the ATF2 nominal emittances ($\varepsilon_x = 2$ nm, $\varepsilon_y = 12$ pm) range from 75 to 155 μm in x, and from 7 to 20 μm in y [65]. However, as will be shown in Section 5.1.3, the OTRs often overestimate the vertical emittance mainly because of the hardware alignment issues and the ambiguity of fitting the beam profile.

The beam orbit diagnostic in the extraction line is handled by 23 beam position monitors (BPMs). There are 12 stripline BPMs, located mainly in the inflector, with a single-shot resolution of about 10 μm, 9 C-band cavity BPMs [68], with sub-micron single-shot resolution and 2 button-type BPMs located near the septum.

3.4. Final focus system

The final focus system (FFS) starts with a matching section that adjusts the β functions of the beam coming from the extraction line. It consists of 6 strong bipolar quadrupole magnets that blow the β functions from average values of less than 10 m in the emittance diagnostic section to several kilometers in the final focus section. The usual practice is that the FFS magnet strengths are kept at their design values and the FFS optics are modified only by changing the setting of the matching quadrupoles. The nominal ATF2 optics, referred to as $1\beta_x^* 1\beta_y^*$, has $\beta_x^* = 4$ mm and $\beta_y^* = 100\ \mu$m. Different optics are referred to with respect to the nominal, for instance $10\beta_x^* 1\beta_y^*$ optics (see Fig. 3.6) has 10 times larger β_x^* value. The $10\beta_x^* 1\beta_y^*$ optics is the most used in recent beam operations.

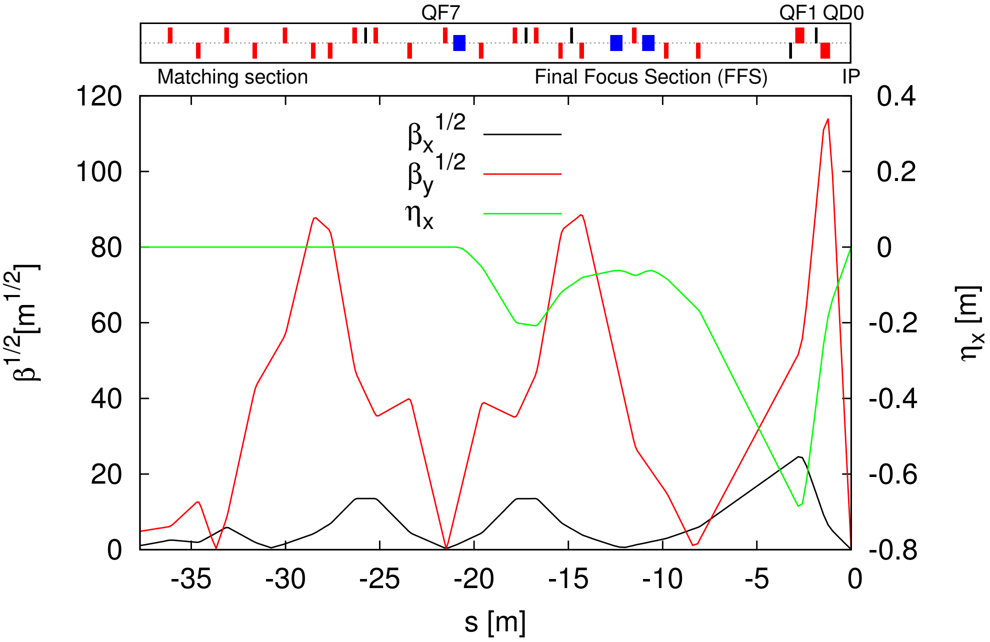

Figure 3.6: Optical functions in the final focus section for $10\beta_x^* 1\beta_y^*$ optics. On top is the layout of the ATF2 lattice: dipoles in blue, quadrupoles in red and sextupoles in black.

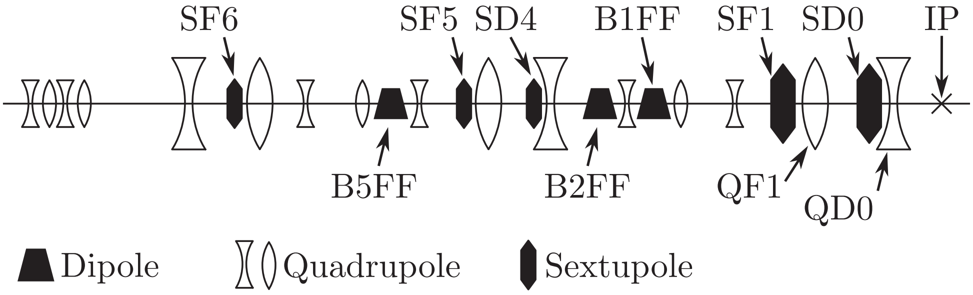

Figure 3.7: Schematic layout of the ATF2 final focus system (graphics from [69]).

The lattice elements of the ATF2 final focus system are shown in Fig. 3.7. The ATF2 FFS follows the telescope design with a local chromaticity correction. The final doublet (FD) quadrupoles (QD0 and QF1) provide the vertical and horizontal focusing, that squeezes the beam to the small size at the IP. The adjacent sextupole magnets (SD0 and SF1) placed in a high-dispersion location correct the chromatic aberrations of the FD quadrupoles. The dispersion is created by the three bending magnets (B1FF, B2FF and B3FF). The second pair of sextupoles (SD4 and SF5) are used to cancel the geometrical aberrations generated by the FD sextupoles. Additional chromaticity required by the local compensation scheme is created by a sextupole magnet located furthest upstream (SF6). Four skew-sextupole magnets (not marked on the figures) were also added to the initial design to control second-order terms and loosen the tolerances on high-order field terms in the quadrupole magnets [69]. Altogether, the FFS contains a total of 3 dipole, 4 dipole correctors, 28 quadrupoles, 5 sextupoles and 4 skew-sextupoles.

All quadrupoles and sextupoles are placed on individual movers to allow the beam steering and adjustment of relative alignment in the transverse plane. Adjacent to these magnets, the C-band cavity BPMs [68] with sub-micron single-shot resolution are installed.

Octupole magnets for the ATF2

Two octupole magnets will be added to the ATF2 beamline in autumn 2016 in order to correct the multipolar field errors [70] and quadrupolar fringe fields [71] in the case of the ultra-low β^* optics (details in Chapter 4). The octupole magnet's design and manufacturing was done at CERN [72, 73], see Fig.3.8 for the OCT1 magnet picture and Table 3.4 for the main parameters. One of the octupoles will be installed in a dispersive location and the other in a non-dispersive location, with a phase advance of 180° between them. The proposed locations for the octupole magnets are: OCT1FF between QD2AFF and SK1FF and OCT2FF between QD6FF and SK3FF.

Table 3.4: Main parameters of the octupole magnets design [73].

	G [T/m^3]	magnetic length [mm]	ampere-turns per coil [A]	# of turns per coil	I [A]	power max. [W]
OCT1	6820	300	1800	60	36	210
OCT2	708	300	180	6	30	19

Final focus system tuning

Beamline imperfections, mainly the magnet misalignments, mispowering and multipolar errors, create the beam transport aberrations that increase the IP vertical beam size. The process of adjusting the machine parameters in order to bring the machine as close as possible to the design performance is called a machine tuning. It consists of matching the dispersion and β function, steering the orbit, correcting the coupling and minimising the residual aberrations. A detailed description of the machine tuning procedures used at the ATF2 together with definitions of the knobs can be found in [69] and [74]. The vertical beam size measured at the IP is used as a figure of merit for the tuning. After the initial tuning, the vertical beam size is dominated

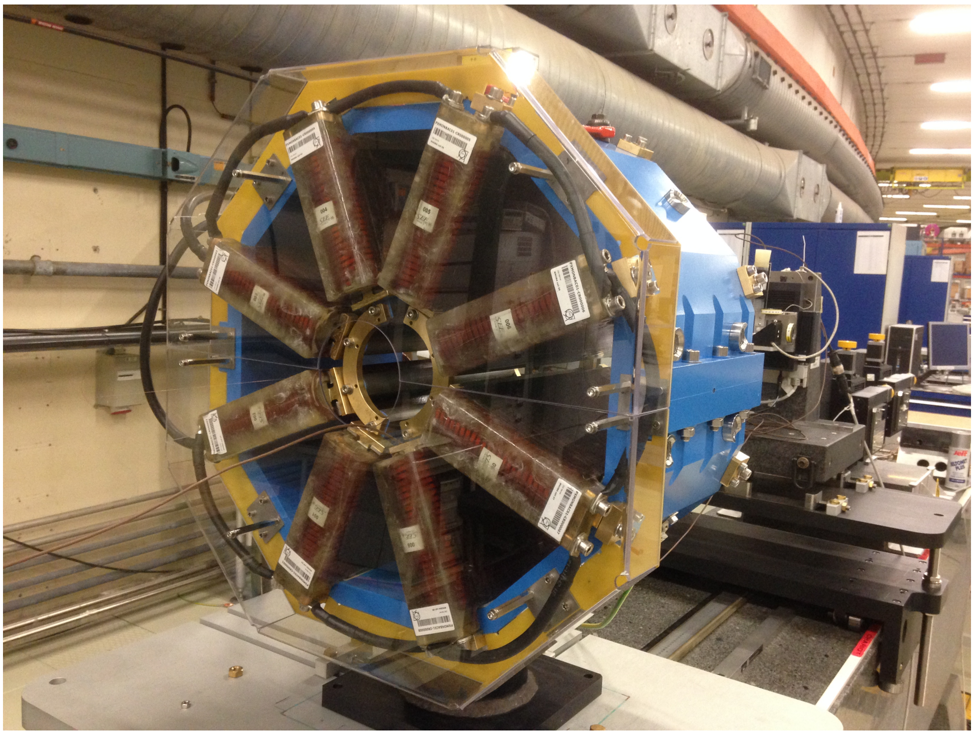

Figure 3.8: OCT1 picture. For operation simplicity the magnet is air cooled and the yoke is composed of two halves which can be easily mounted on the beam line [73].

by the linear aberrations of beam waist longitudinal position shift, vertical dispersion and $x'y$ coupling. For each of these aberrations there is a dedicated knob, respectively Ay, Ey and C_2, constructed to be orthogonal by using deliberate horizontal and vertical displacements of the normal sextupole magnets. The nonlinear beam aberrations are corrected with the second order tuning knobs (Y22, Y24, Y26, Y44, Y46, Y66) by changing the strength of the normal and skew sextupole magnets. The digits relate to coordinate indexes (x, x', y, y', ct, δ) of the corresponding correlation, e.g.:

$$\mathrm{Y26} = \frac{\langle (\mathrm{y} - \langle \mathrm{y} \rangle)\,(\mathrm{x}' - \langle \mathrm{x}' \rangle)\,(\delta - \langle \delta \rangle) \rangle}{\sqrt{\langle (\mathrm{x}' - \langle \mathrm{x}' \rangle)^2\,(\delta - \langle \delta \rangle)^2 \rangle}} \tag{3.1}$$

is the aberration coming from the correlation between vertical position (y), horizontal angle (x') and relative momentum deviation (δ) of the electrons at the IP.

3.5. The interaction point

The ATF2 focal point is called an interaction point (IP) by analogy with particle colliders. In fact, the ATF2 provides just one particle beam, so no high-energy collisions occur there. Instead, the ATF2 performance is verified by measuring the IP beam sizes using the so-called

Shintake monitor [52, 53]. It is an interference monitor where two laser beams cross in the plane transverse to the electron beam in order to form a vertical interference pattern, see Fig. 3.9.

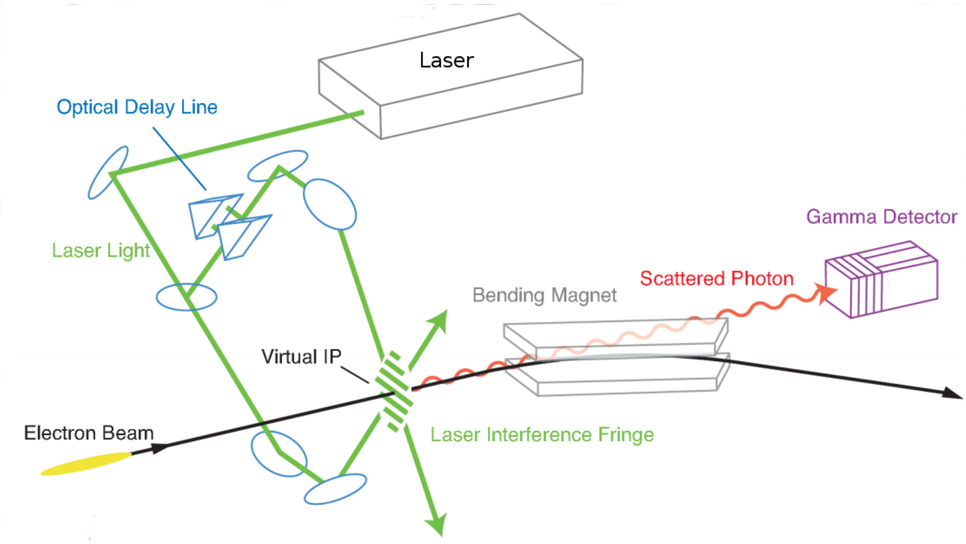

Figure 3.9: Shintake monitor schematic design. The electron beam interacts with a transverse interference pattern generated by two crossing laser beams. The number of scattered photons varies with the fringe size and the particle beam size.

The fringe pattern vertical distribution is modified by changing the phase of one laser-path in the optical delay line. The beam size is inferred from the modulation of the resulting Compton scattered photon signal detected by a downstream photon detector, see Eq. (3.2):

$$\begin{aligned} \mathrm{M} &= C\,|\cos\theta|\exp\left[-2\left(k_y\sigma_y\right)^2\right], \\ k_y &= \pi/d,\ d = \frac{\lambda}{2\sin\left(\theta/2\right)}, \end{aligned} \tag{3.2}$$

where C is the modulation reduction factor which represents the overall systematic effect causing a decrease of the observed modulation due to the monitor imperfections, θ is the crossing angle and $\lambda = 532$ nm is the laser wavelength. Three laser crossing angle modes (2-8 degree, 30 degree, 174 degree) extend the dynamic range from 5 μm to 20 nm, see Fig. 3.10.

Larger beam sizes are measured by a wire scanner installed at the IP. It consists of a carbon wire 5 μm in diameter that when moved across the beam generates bremsstrahlung gamma rays. The number of photons is proportional to the charge of the slice interacting with the wire at each position setting. Profiles are constructed from the number of photons as a function of wire position [75].

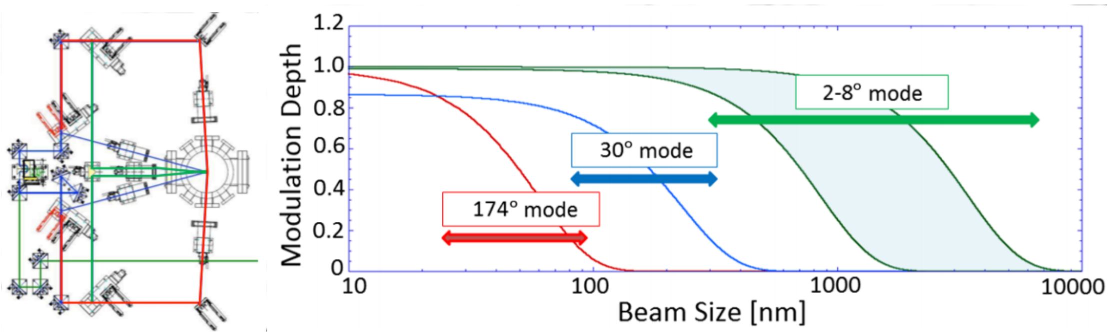

Figure 3.10: (Left) IPBSM laser path over the optical table perpendicular to the beam propagation. (Right) Beam size resolution for the angle modes : 2° ∼ 8° *in green, 30° in blue and 174° in red.*

3.6. Computer model of the ATF2

The ATF2 computer model in the MAD-X [76] environment was created to simulate the machine performance. All the physical elements (magnets, drifts, monitors, correctors, etc.) of the ATF2 line are present in the model including their known imperfections. Especially important are the measured multipolar errors [77, 78] of the ATF2 magnets, because of their large effect on the beam dynamics. The MAD-X environment is very useful for optics design as it calculates the linear optical functions. The nonlinear beam dynamics are handled by the *polymorphic tracking code* (PTC) [79] (built-in into MAD-X) which calculates the transfer map coefficients and performs the particle tracking. The IP vertical beam size is a figure of merit in many analyses. It is usually calculated using the transfer map provided by the PTC and *MAPCLASS2* code [80] which performs the operations described in Section 2.1.2 and in [32].

Chapter 4

Nonlinear beamline optimisation for nominal and low β_y^* optics

Feasibility and performance of the ATF2 final focus system with lowered β_y^* values has been studied in order to investigate the limits of beam focusing at the IP and the behavior of more chromatic optics. The three sets of optics were designed in terms of β_y^* value: nominal β_y^* (100 μm), half β_y^* (50 μm) and ultra-low β_y^* (25 μm). Each optics was optimised for delivering the minimum possible vertical beam size at the IP which requires an efficient correction of the nonlinear transport aberrations. The two proposed methods for lowering the IP vertical beam size are described in Section 4.1. The results presented in this Section were also published in [81].

In Section 4.2 we investigate the effect of the quadrupole fringe fields on the IP vertical beam size in the ATF2 nominal β_y^* and ultra-low β_y^* case. The same analysis is also performed for the design optics of CLIC and the ILC. The results presented in this section were also published in [71].

The IP beam size growth with increasing bunch intensity, mainly due to wakefields [82], force us to operate the ATF2 beam at the lowest possible intensity of about 10^9 electrons per bunch (a factor 5 lower than nominal [64]). The contribution of optical aberrations to spot size increase with bunch intensity for the ATF2 nominal β_y^* and ultra-low β_y^* optics is described in Section 4.3. The results presented in this section were also published in [83].

In Section 4.4 we describe the developed tools for studying the ATF2 nominal β_y^* optics performance with the realistic machine imperfections.

4.1. Beam size optimisation for low β_y^* optics in the ATF2

There are two reasons for lowering the β_y^* value in the ATF2. Firstly, it allows us to decrease the ideal minimum beam size at the IP (see Eq. (2.6)) and therefore study the focusing limits of the ATF2 final focus system. The second reason is that it increases the strength of chromatic aberrations (see Eq. (2.38)), so a certain level of chromaticity can be studied. This is especially important for developing the FFS for CLIC. Currently, the level of chromaticity in the ATF2 is comparable with the ILC design, but a factor 5 lower than in the case of CLIC (see the last column of Table 4.1). Decreasing the β_y^* value in the ATF2 will raise its chromaticity close to the level of CLIC.

Three sets of optics with decreased β_y^* value were designed for the ATF2 final focus line: nominal β_y^* (100 μm), half β_y^* (50 μm) and ultra-low β_y^* (25 μm). Their important parameters, compared with CLIC and the ILC, are presented in the Table 4.1.

Table 4.1: Some of the FFS parameters for ATF2, CLIC and ILC.

	ε_y	β_x^*	β_y^*	$\sigma_{y,\mathrm{design}}^*$	L*	ζ_y
	[pm]	[mm]	[μm]	[nm]	[m]	$\sim (L^*/\beta_y^*)$
ILC	0.07	11	480	5.9	3.5/4.5	7300/9400
CLIC	0.003	4	70	1	3.5	50000
ATF2 nominal	12	4	100	37	1	10000
ATF2 nominal, $10\beta_x^*$	12	40	100	37	1	10000
ATF2 half β_y^*	12	4	50	30.5, 25[a]	1	20000
ATF2 half β_y^*, $10\beta_x^*$	12	40	50	26	1	20000
ATF2 ultra-low β_y^*	12	4	25	27, 20[a]	1	40000
ATF2 ultra-low $\beta_y^*, 10\beta_x^*$	12	40	25	21	1	40000

---

[a] using octupole magnets

The decrease of the β_y^* value causes an increase of the β_y function in the final focus region as is shown in Fig. 4.1. In consequence, the beam is more sensitive to any beamline imperfections like for instance alignment errors, magnet mispowering, additional dispersion, multipolar field errors, ground motion, wakefields and others. These effects, if not corrected, can cause a significant vertical beam size growth at the IP.

One considered solution is to increase the β_x^* value in order to lower the β_x function along the FFS and therefore decrease the beam sensitivity to the beamline imperfections in the horizontal plane. However, it causes a horizontal IP beam size increase and therefore it is not a favorable solution for linear colliders as it may reduce the luminosity. The nominal value of β_x^* in the ATF2 is 4 mm, but in recent operation $10\beta_x^* = 40$ mm has been used as it better corresponds to the expected strength of the optical aberrations in the ILC [84]. In this study both nominal β_x^* (4 mm) and $10\beta_x^*$ (40 mm) are considered. An optics with $25\beta_x^* = (100\text{ mm})$ was also investigated for the experimental studies described in Chapter 5.

The second considered method is the installation of two octupole magnets in the ATF2 beamline. Some optical aberrations are corrected with the use of sextupole magnets, but detailed analysis of the multipole components at the ATF2 [70] revealed the strong third order contribution coming from the QD0 magnet (last quadrupole before the IP). Also the FD fringe fields give mainly third order kicks which justifies the use of octupole magnets (details in Section 4.2).

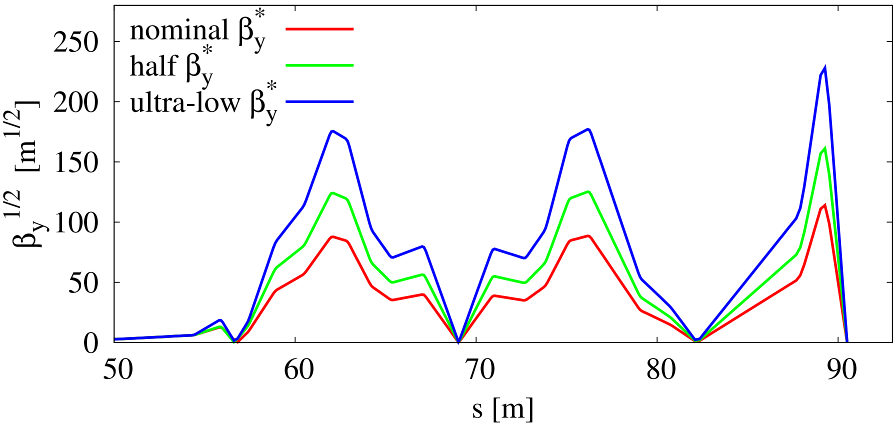

Figure 4.1: β_y function along the ATF2 beamline in case of nominal β_y^*, half β_y^* and ultra-low β_y^* optics.

For all considered sets of optics the IP vertical beam size was minimised using the proposed mitigation methods and the MAD-X model of the machine (see Section 3.6). The results are presented in Fig. 4.2. One can see that for the nominal β_x^* value (blue curve) the IP vertical beam sizes are much larger than the ideal minimum beam sizes (black curve) especially for half β_y^* and ultra-low β_y^* optics. Both increasing the β_x^* value by a factor 10 (orange curve) and installing the octupole magnets (red curve) helps in bringing the IP vertical beam sizes close to their limits. The second solution is preferred as it does not cause the horizontal beam size growth at the IP. As a result of this study, the installation of two octupole magnets in the ATF2 is scheduled for autumn 2016 in order to support the ultra-low β_y^* experiment.

4.2. Quadrupole fringe fields effect on the IP beam size

The final part of the FFS is usually formed by a final doublet (FD), which is a pair of strong quadrupole magnets located upstream from the IP. As those magnets are in a high β function

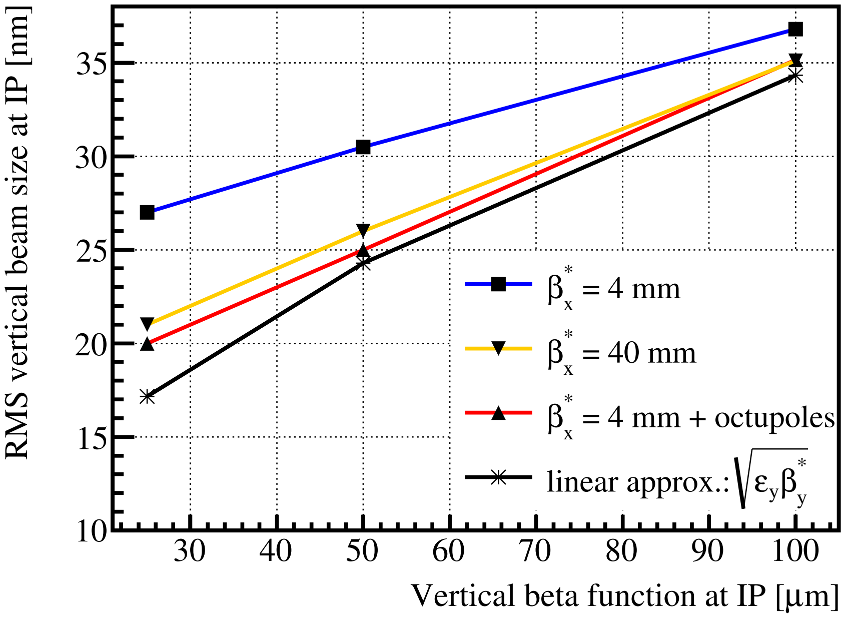

Figure 4.2: Expected vertical beam size in the ATF2 for three considered β_y^* values and proposed mitigation methods.

region, the magnetic field imperfections including the fringe fields can significantly affect the beam size.

The lattices considered in this study are the Final Focus Systems (FFS) of CLIC, the ILC and 3 versions of the Accelerator Test Facility 2 (ATF2). See Table 4.2 for a comparison of their design parameters important for this study. The IP vertical beam size is calculated order by order as it was described in Section 3.6. Magnet imperfections other than fringe fields are neglected throughout this section. A detailed study of the magnetic imperfection's impact on the beam size for the ATF2 can be found in [70].

Project	E [GeV]	L* [m]	β_x^* [mm]	β_y^* [mm]	σ_x^* [nm]	σ_y^* [nm]	QD0 k_1 [m^{-2}]
CLIC 500 GeV	250	3.5	8	0.1	207	2.4	-0.0772
ILC	250	3.5	11	0.48	481	6.1	-0.1379
ATF2 nominal	1.3	1	4	0.1	2910	37	-2.8715
ATF2 ultra-low β^*	1.3	1	4	0.025	3300	23	-2.8751
ATF2 ultra-low β^*, $10\beta_x^*$	1.3	1	40	0.025	9000	23	-2.8667

Table 4.2: Comparison between relevant parameters of the considered beam lines.

4.2.1. Linear effects of the fringe fields

The hard-edge model, widely used in beam lines modeling, assumes that the magnetic field changes step-like at the border of the magnet, while in reality it changes smoothly and fringes outside the magnet. A more accurate modeling of the magnetic field along the longitudinal axis can be achieved by adding a series of shorter magnets (50 in this study) at each side with progressively lower values of normalized strength k_1, as done e.g. in [85]. The magnet strengths k_1 have to be modified in a way so that the integrated strength $\int k_1 ds$ of the magnet assembly remains the same as $k_1 L$ of the hard-edge magnet.

The comparison of the hard-edge and fringed magnet models for CLIC, the ILC and the ATF2 is given in Figure 4.3. The Enge function [86], see Eq. (4.1), fitted to simulated magnet strength data is used to model the fringe field shape.

$$F(z) = \frac{1}{1 + \exp\left[a_0 + a_1(z/D) + a_2(z/D)^2 + ... + a_5(z/D)^5\right]}, \tag{4.1}$$

where $a_0, ..., a_5$ are fitting parameters and D is the magnet aperture diameter, see Table 4.3.

The magnet gradient of the CLIC final doublet normal conducting QD0 quadrupole is obtained from magnetic simulation [87] and fitted with two Enge functions (ensuring continuity), one for the region inside the magnet and a second for the outside region. This provides a good fringe shape description, as it turns out that using just one Enge function for the whole fringe region is not sufficient. The fit parameters and magnet apertures are given in Table 4.3. Magnetic measurements or simulations of the ATF2 quadrupoles were not available so the fringe region was modeled with the CLIC quadrupole parameters scaled with the aperture according to Eq. (4.1). The ILC quadrupoles are planned to be superconducting so the fitting parameters of superconducting magnets are needed. As the ILC magnetic simulation was not available, the HL-LHC MQXF magnet's [88] data were used applying the corresponding aperture scaling. The apertures for the final doublet quadrupoles are 20 mm for CLIC and the ILC, and 50 mm for the ATF2.

Parameter	CLIC QD0 ($z < 0$)	CLIC QD0 ($z > 0$)	MQXF
a_0	0.166	0.205	-0.283
a_1	-4.313	-4.127	-3.836
a_2	1.170	-1.830	1.948
a_3	0.030	-0.340	-2.697
a_4	-0.003	0.057	1.289
a_5	-0.007	0.029	-0.186
D [mm]	20	20	150

Table 4.3: Parameters of the fringe field model.

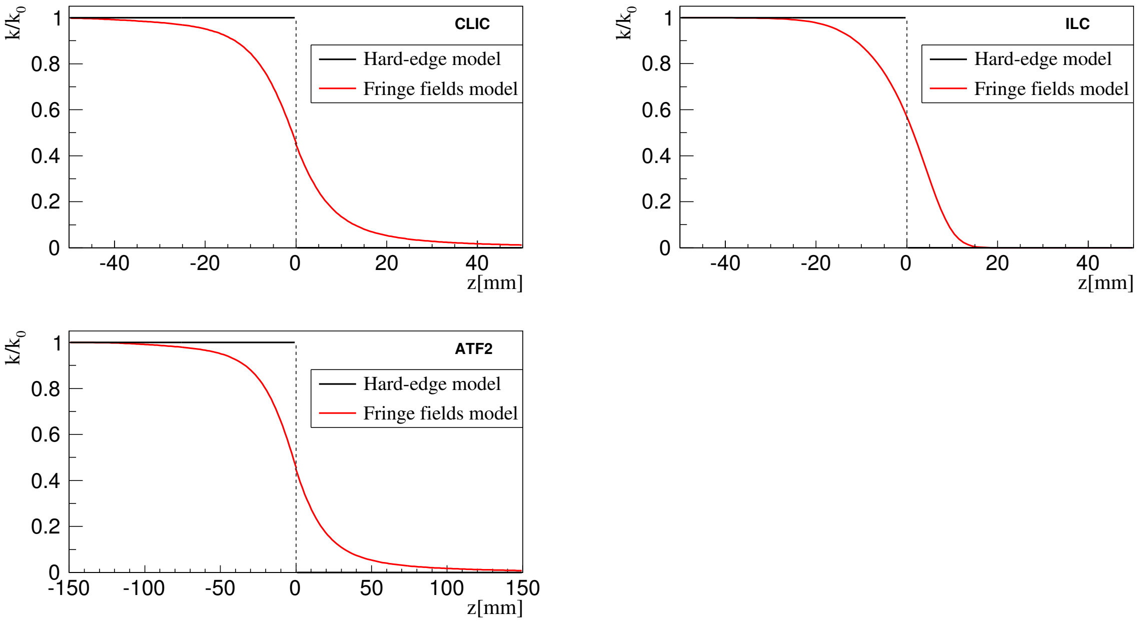

Figure 4.3: Hard-edge and fringe fields models. Note the different longitudinal scale for each case, which depends on the aperture.

CLIC and ILC BDS lattices

Figures 4.4 and 4.5 present the impact of the linear fringe fields of the final doublet magnets on the transverse beam size for CLIC and the ILC. The change of the IP transverse beam size due to the liner fringe field model is small (maximum beam size change is about 2%) and can be easily corrected by adjusting the FD quadrupole strengths.

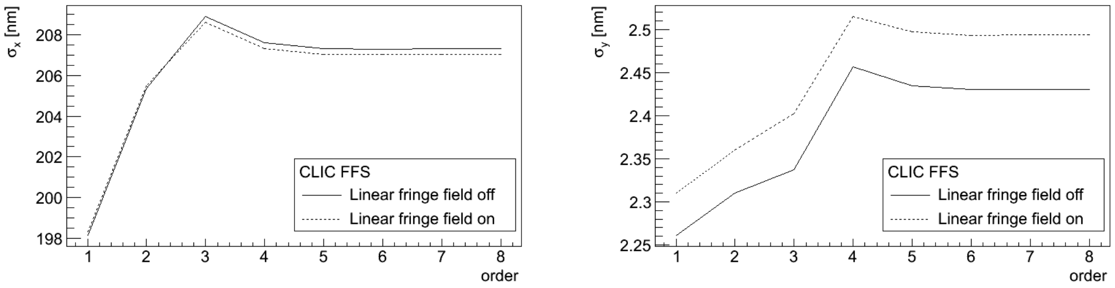

Figure 4.4: Linear fringe field impact on the horizontal (left) and vertical (right) beam size in the CLIC BDS lattice. The horizontal axis stands for the polynomial order of the transfer map.

ATF2 lattices

For ATF2 lattices, the beam size is more sensitive to the linear fringe fields which is probably caused by two factors. Firstly, the ATF2 FD fringe fields region is larger, because of the larger magnet apertures. The second reason is that the normalized gradient of the ATF2 FD magnets

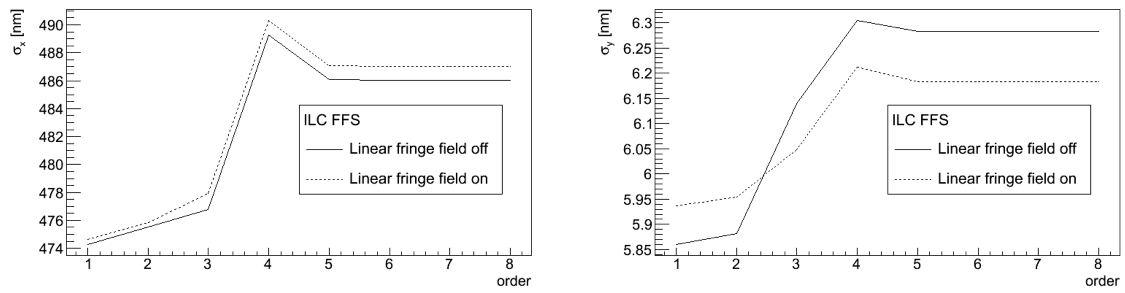

Figure 4.5: Linear fringe field impact on the horizontal (left) and vertical (right) beam size in the ILC BDS lattice.

is significantly higher than in the case of CLIC and the ILC (see Table 4.2), which enhances the fringe field effects. As it is shown in Figures 4.6 and 4.7, one order of magnitude increase of the IP transverse beam size is observed due to the linear fringe fields model. However, it is possible to recover the original beam sizes, as also shown in the Figures 4.6 and 4.7, by changing the FD quadrupole gradients. The new gradients are compared to the design values in Table 4.4. The experimental verification of the linear fringe fields mitigation due to FD quadrupoles tuning is difficult to perform. The reason is that in experiment the fringe fields are not split into the linear and non-linear parts. Also tuning is a rather empirical procedure where many aberrations are mixed together and difficult to distinguish. Finally, the ATF2 is currently running with the $10\beta_x^*$ optics which is less sensitive to the fringe field's impact.

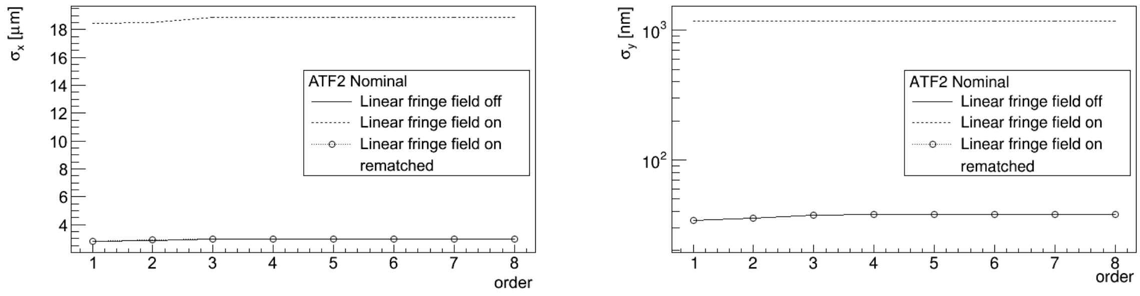

Figure 4.6: Linear fringe field impact on the horizontal (left) and vertical (right) beam size in the ATF2 nominal lattice, together with a correction of the fringe field effect using the FD quadrupoles as reported in Table 4.4.

Magnet	Design $k_1\,[m^{-2}]$	New $k_1\,[m^{-2}]$	Change in %
QF1 nominal	1.561659	1.568471	0.436
QD0 nominal	-2.871512	-2.886853	0.534
QF1 ultra-low β^*	1.566149	1.574011	0.502
QD0 ultra-low β^*	-2.875086	-2.892758	0.615

Table 4.4: Change of the ATF2 FD magnets strength needed to correct the linear effect of the fringe fields.

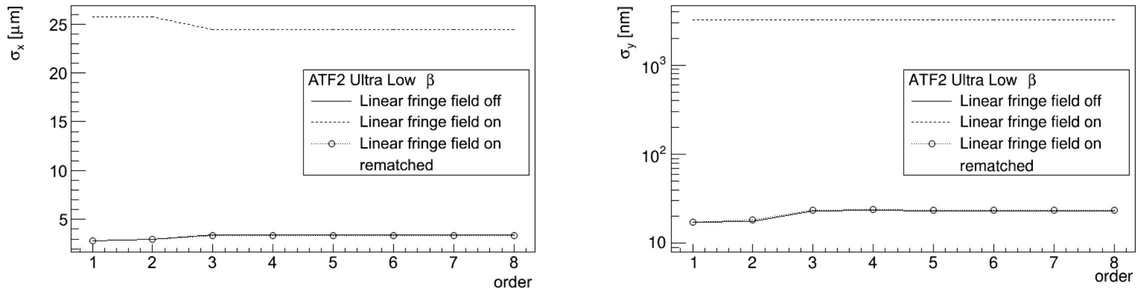

Figure 4.7: Linear fringe field impact on the horizontal (left) and vertical (right) beam size in the ATF2 ultra-low β^* lattice, together with a correction of the fringe field effect using the FD quadrupoles as reported in Table 4.4.

4.2.2. Nonlinear effects of the fringe fields

The dynamics of the beam in the presence of nonlinear fringe field components was already studied in analytical ways [89, 90, 91, 92] and by numerical simulations based on the magnetic field data e.g. [93]. We approximate the fringe fields by symplectic kicks (see Eqs. (4.2)) applied to a particle when it enters and leaves a magnet [94, 95]. The transfer map of the beam line including the fringe fields is computed with the use of PTC [79], and the IP vertical beam size is calculated as described in Section 3.6. The kicks at the magnet entrance are given by:

$$\begin{aligned} \Delta x &= \frac{k_1}{12}\left(x^3+3xy^2\right) \\ \Delta p_x &= -\frac{k_1}{4}\left[\left(x^2+y^2\right)p_x-2xyp_y\right] \\ \Delta y &= -\frac{k_1}{12}\left(3x^2y+y^3\right) \\ \Delta p_y &= \frac{k_1}{4}\left[\left(x^2+y^2\right)p_y-2xyp_x\right], \end{aligned} \tag{4.2}$$

where $\mathrm{k_1, x, y, p_x, p_y}$ are the quadrupole strength, horizontal and vertical particle transverse positions and momenta, respectively. The kicks at the exit are opposite in sign.

For CLIC and the ILC FFS the non-linear fringe fields do not affect the beam size, see Figures 4.11 and 4.12. However, a significant effect is observed for the ATF2 lattices, see Figures 4.13 and 4.14. The reason is that, as seen in Eqs. (4.2), the fringe field kicks scale with the normalized magnet gradient which has larger value for the ATF2 than for CLIC and the ILC, see Table 4.2. In the case of the nominal lattice, fringe fields decrease the beam size at the IP by a few percent, which shows the focusing impact of the fringe fields in this particular case. However, we consider an error free lattice, so this can change after applying the magnetic errors. On the other hand, for the ultra-low β^* the IP beam size increases significantly (σ_y^* by 47%) with the third order aberrations being the main source, as expected from Eqs. (4.2).

The insertion of the two octupole magnets is a proposed solution for the mitigation of the fringe field's impact on the IP beam size as they give the third order contribution to the beam dynamics. It has already been demonstrated in [70] that the octupoles can be used for the suppression of the aberrations coming from the magnetic imperfections in the ATF2 beam line. The choice of the octupole's location depends on the optical functions and it is desired to install the octupoles in the region of high β function. The two possible locations were investigated, marked in Fig. 4.9. Location A assumes the octupoles to be installed in the regions of the maximum β_y function. However, this location suffers from space limitations. Therefore, location B was proposed which is less effective, but without the space constraints. The considered locations together with the ATF2 optics are given in Figure 4.8. From the simulations it turns out that location A is better as it significantly reduces the fringe field aberrations (see Figure 4.14) even for relatively low strength, see Table 4.5. The octupoles in the location B need to be much stronger, but they are feasible and sufficiently suppress the fringe field aberrations. The vertical phase space distributions at the IP for the case of the ultra-low β^* lattice are depicted in Figure 4.10. It is clear that the phase space suffers from aberrations in the case when fringe fields are included, but without the octupoles. These aberrations can be suppressed with the use of octupoles.

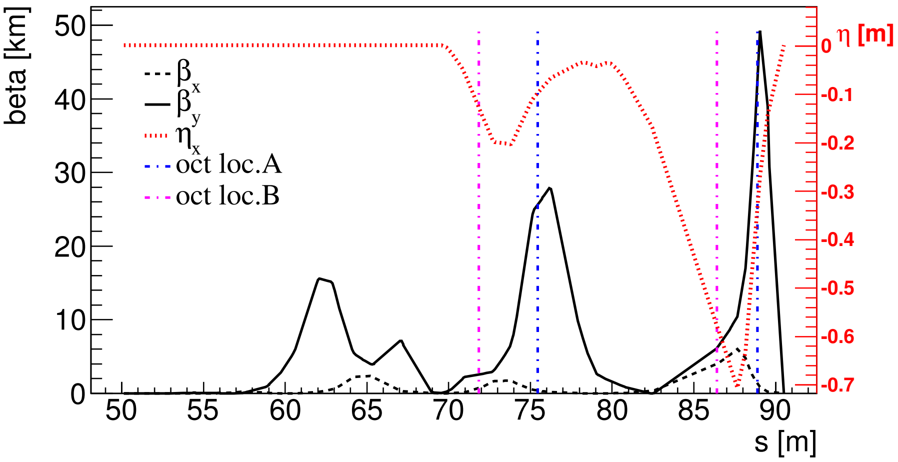

Figure 4.8: β functions and dispersion along the FF line with the two octupoles locations under consideration.

	Location A	Location B
OCT1FF $k_3L[m^{-3}]$	-20.6	-3.7
OCT2FF $k_3L[m^{-3}]$	145.4	393.2
$\sigma_y^{*(5)}$[nm]	19	23

Table 4.5: Integrated strengths of the octupole magnets in locations A and B and corresponding vertical beam size at the IP of 5th order.

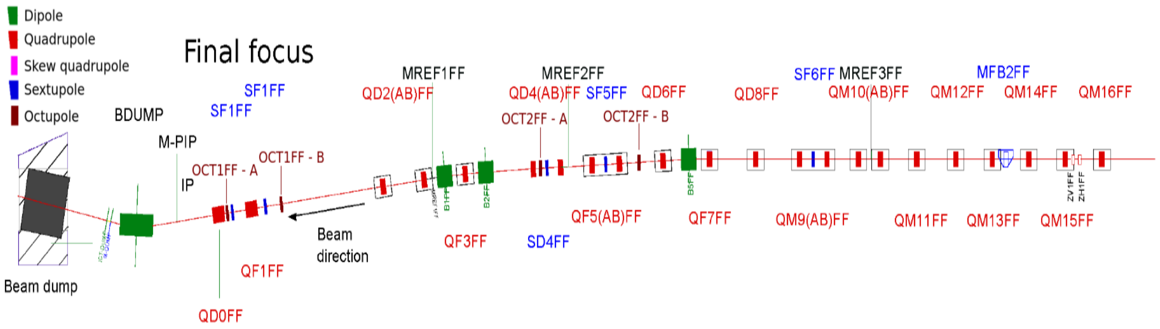

Figure 4.9: Layout of the ATF2 Final Focus line, with the two octupole locations under consideration.

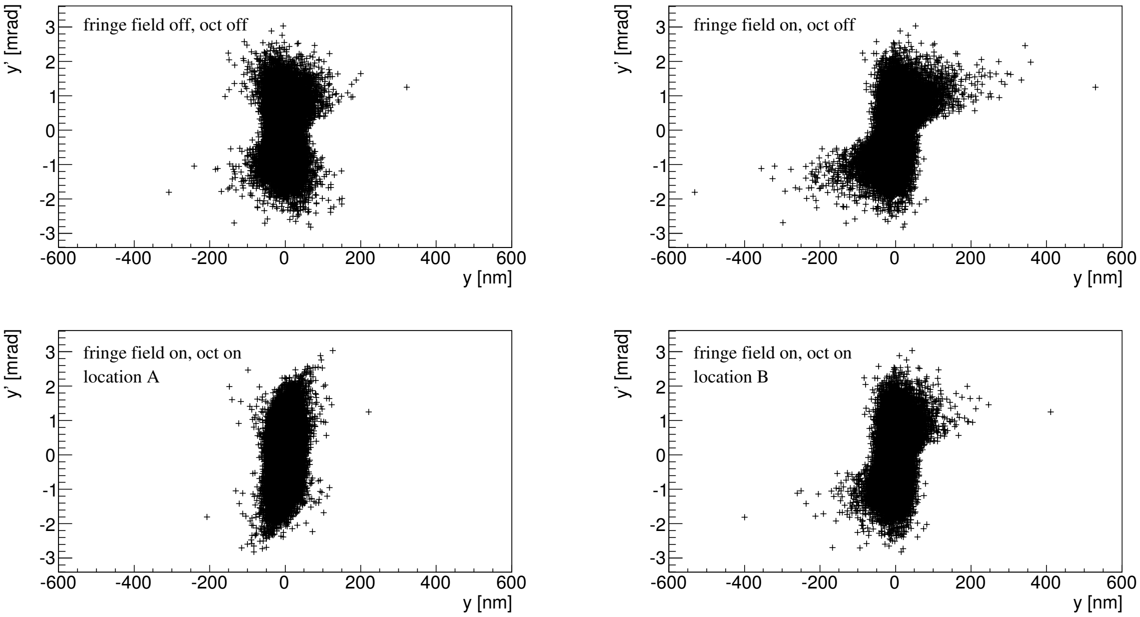

Figure 4.10: The vertical phase space distributions in IP for the case of the ultra-low β^* lattice. The upper left plot corresponds to the case without fringe fields and without octupoles. The upper right plot corresponds to the case with fringe fields but without octupoles. Both bottom plots correspond to the case with fringe fields and octupoles included.

Another possibility (also explored in [70]) for the fringe field effect mitigation is the increase of β_x^*, as can be seen in Figure 4.15. The reason is that a higher value of β_x^* causes the decrease of β_x in the final doublet and therefore the fringe field effect is weaker. The increase of β_x^* from 4 mm to 40 mm causes the fringe fields to be negligible.

Conclusions

Magnetic fringe fields give an unavoidable contribution to the particle transport through a beamline which can be a source of aberrations, especially for magnets in high β regions. Understanding their impact and mitigation methods is therefore fundamental in order to avoid unwanted beam size growth.

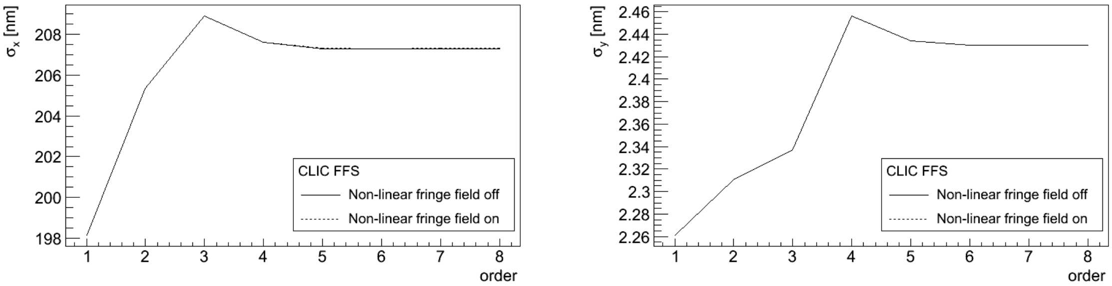

Figure 4.11: Nonlinear fringe field impact on the horizontal (left) and vertical (right) beam size in the CLIC BDS lattice.

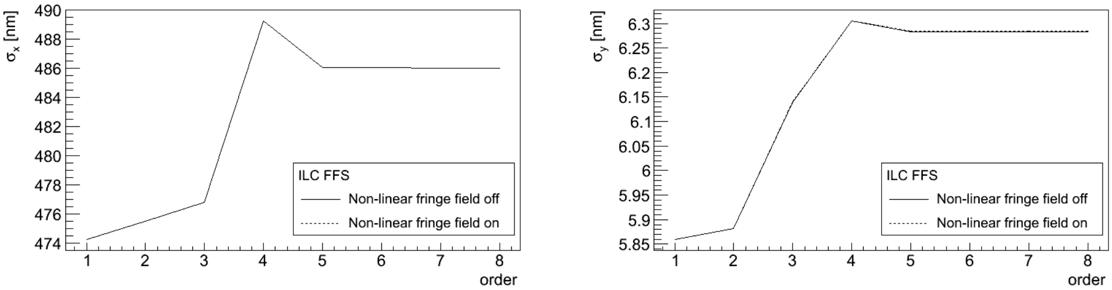

Figure 4.12: Nonlinear fringe field impact on the horizontal (left) and vertical (right) beam size in the ILC BDS lattice.

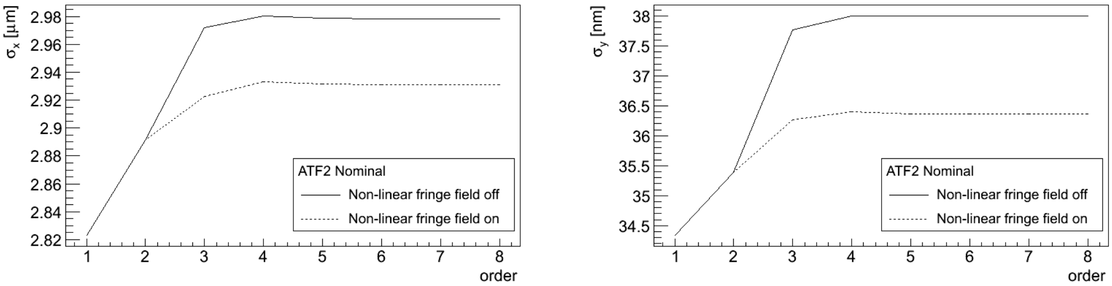

Figure 4.13: Nonlinear fringe field impact on the horizontal (left) and vertical (right) beam size in the ATF2 nominal lattice.

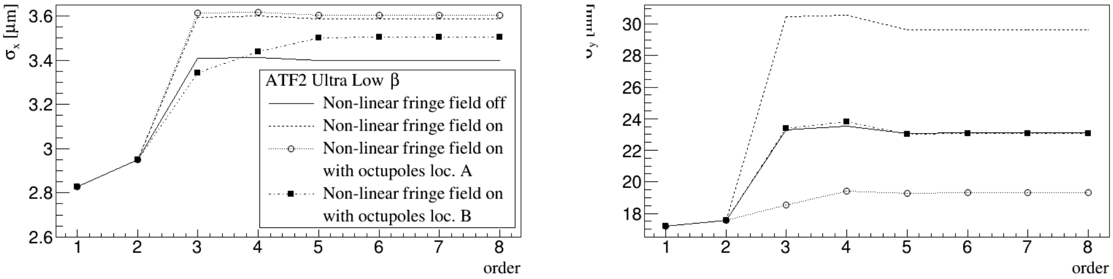

Figure 4.14: Nonlinear fringe field impact on the horizontal (left) and vertical (right) beam size in the ATF2 ultra-low β_y^* lattice.

The linearly modeled fringe fields cause a negligible increase of the transverse beam size in CLIC and the ILC FFS lattices. On the other hand, for the ATF2 lattices the beam size increase

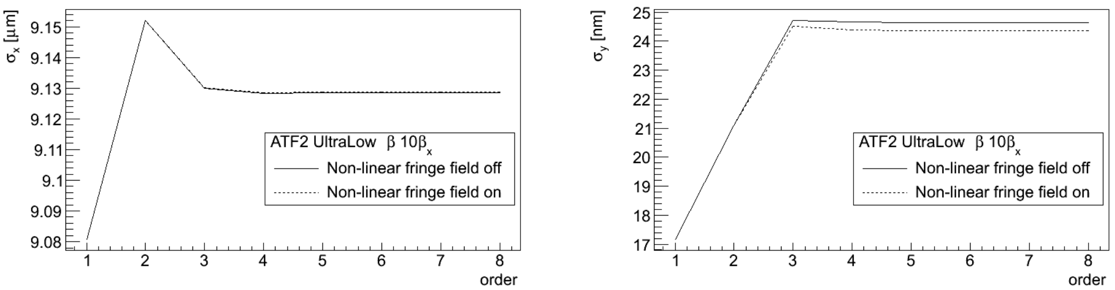

Figure 4.15: Nonlinear fringe field impact on the horizontal (left) and vertical (right) beam size in the ATF2 ultra-low β_y^* , $10\beta_x$ *lattice.*

is significant and a correction of the final doublet magnet strength is needed.

The non-linear model of fringe fields results in third order aberrations which are negligibly small for CLIC and the ILC FFS, but are important for the ATF2 ultra-low β_y^* and require corrections. The same two methods proposed in [70] to mitigate multipolar errors are verified to correct the fringe field aberrations. The first method uses the two octupole magnets to cancel the non-linear aberrations. The second method consists of increasing β_x^* to reduce the effect of fringe fields in the final doublet.

4.3. Contribution of optical aberrations to spot size increase with bunch intensity

Measurements over the past years indicate that the ATF2 vertical beam size, achieved after tuning, strongly rises with bunch intensity [82]. This increase could have several different origins. For example, it could be due to wakefields occurring between the ATF damping ring and the IP, and/or be due to changes in the transverse emittances and energy spread in the damping ring, which are known to increase with intensity as a result of intra-beam scattering (IBS). In this section we address the second possibility. Past measurements and simulations of the IBS effects in the ATF damping ring and in the extraction line are used to model the intensity-dependent initial emittances and energy spread at the entrance of the final focus. Using this model, particle tracking simulations predict the IP vertical beam size growth expected from the known optical aberrations for initial beam parameters corresponding to varying bunch intensities. Comparing simulation results with emittance measurements at different locations allows us to draw some conclusions about the impact of IBS in the damping ring on the IP spot size, and about possible single-bunch wakefields in the ATF2.

In 2003 the dependence of the ATF damping ring emittance and momentum spread on the beam intensity was measured [62, 63]. Figures 4.17a and 4.17b summarize the emittance measurements (grey bands). The measured growth of the momentum spread with rising bunch intensity [62], shown in Fig. 4.16 (upper curve), is included in all the simulations reported in this section. The strong intensity dependence of the emittance, and, especially, of the momentum spread, is due to the intra-beam scattering (IBS) [62].

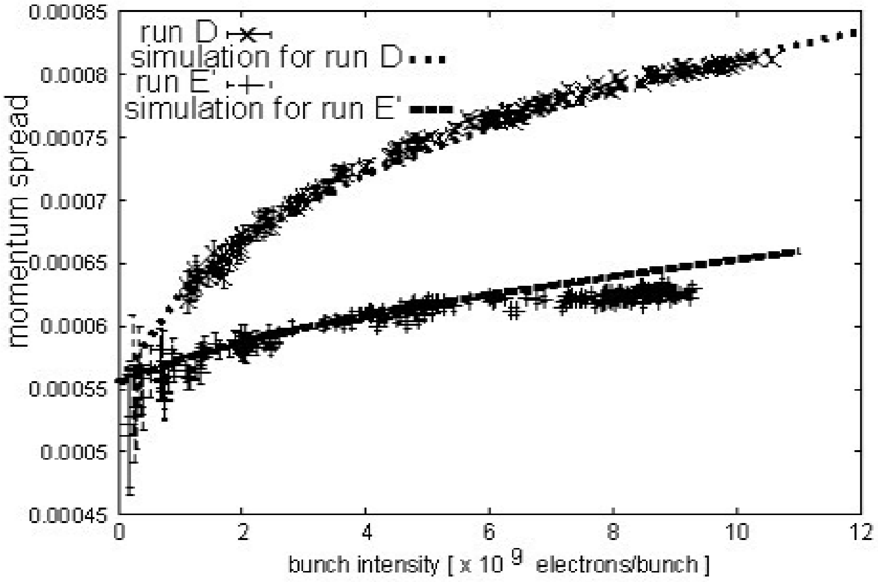

Figure 4.16: Measured rms momentum spread in the damping ring as a function of the bunch charge compared with IBS simulations (graphics from [62]). The upper curve was obtained in standard operation, far from the coupling resonance, and it is used for our simulations.

We next examine how this beam emittance increase affects the IP vertical beam size. Three cases are considered: The first case assumes the beam emittances measured in the damping ring (DR). In the second case a constant increment is added to model the emittance of the beam extracted from the damping ring to the extraction line (EXT). In the last case, the beam emittance measured in the EXT line is considered.

For all three cases the corresponding IP vertical beam size is calculated in order to study if the intensity dependent growth of emittance and momentum spread could be responsible for the observed intensity-dependent beam size. The results are presented in Figs. 4.17c and 4.17d, and described in the following.

The grey bands in Figs, 4.17c and 4.17d present the IP vertical beam size calculated for the beam parameters in the damping ring and using the nominal β_y^* (Fig. 4.17c) and nominal β_y^*, $10\beta_x^*$ (Fig. 4.17d) optics. The IP vertical beam size increases together with damping ring emittance and momentum spread, but still the computed vertical beam sizes at the IP are lower than the design values. The reason for this is that the vertical emittance plotted as a grey band in Figs. 4.17a and 4.17b is lower than the design value in the final-focus line (12 pm) and significantly lower than some of the values measured in the extraction line. For simplicity

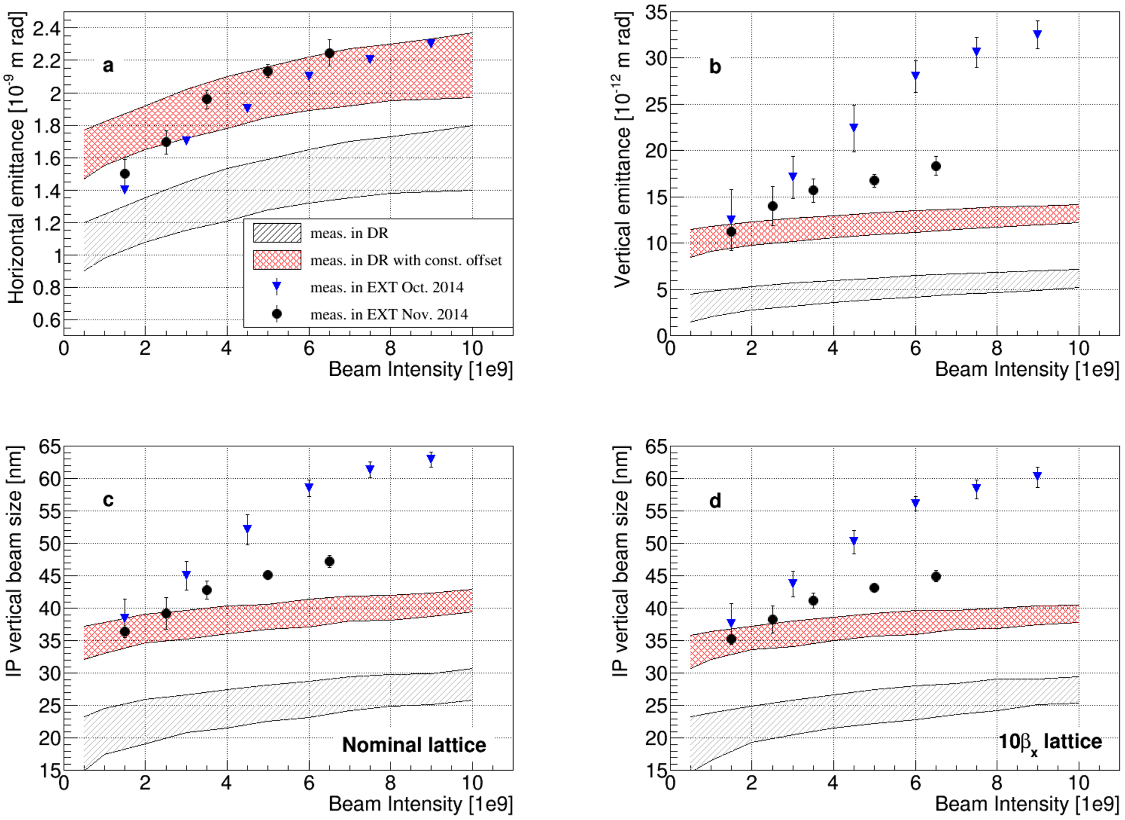

Figure 4.17: Top: Horizontal (a) and vertical (b) emittances versus bunch charge. The grey band represents the beam emittance measured in the damping ring [62, 63], red band accounts for the beam emittance in the EXT line assuming a constant growth term (added to the data in the grey band), and the points correspond to the emittance measured in the EXT line in autumn 2014 [96, 97]. The emittance is plotted as a function of beam intensity. Bottom: Simulated vertical IP beam size as a function of bunch intensity, considering the emittance values from the upper two pictures and the charge-dependent momentum spread of Fig. 4.16), for the nominal (c) and relaxed optics (d).

we assume that during beam extraction from the damping ring the emittance is enlarged by a constant value, independently of the bunch intensity. We set this constant shift to 7 pm in the vertical plane and to 0.57 nm in the horizontal plane, so as to obtain the design emittance values at the nominal bunch intensity N_b of $5 \cdot 10^9$ e$^-$. The corresponding emittance values are shown as red bands in Figs. 4.17a and 4.17b, together with the associated vertical IP beam size in Figs. 4.17c and 4.17d. At nominal bunch intensity N_b of $5 \cdot 10^9$ e$^-$ with the $10\beta_x$ optics the calculated vertical IP beam size roughly equals its design value of 37 nm; with the nominal optics it is at most a few nm larger.

In October and November 2014 the beam emittance in the extraction line was measured as a function of bunch intensity [96, 97]. The measurement data are represented as points in Figs, 4.17a and 4.17b. The emittances (especially the vertical one) measured in the extraction line increase with intensity much faster than those in the damping ring. Possible wakefield effects are being investigated and mitigated [82, 98]. The values of the vertical IP beam sizes simulated for the emittances measured in the extraction line, shown as plotting symbols in Figs. 4.17c and 4.17d, demonstrate that the optical aberrations of the final focus do not prevent ATF2 from reaching the targeted low beam size (e.g. $\sigma_{\mathrm{y}}^* < 40$ nm) at low bunch intensity ($N_b < 1.5 \cdot 10^9\ e^-$). This prediction is consistent with the experimental observations: the lowest measured vertical IP beam sizes for bunch intensities $N_b < 10^9\ e^-$ were 53 nm in May 2014 [99], 44 nm [100] in June 2014, and 42 nm [84] in February 2016. At nominal intensity of $N_b \sim 5 \cdot 10^9\ e^-$ much larger spot sizes were measured, i.e. well above 100 nm. Possible explanations include a degraded beam-orbit stability (compromising the spot-size tuning), wakefields, and less accurate performance of the beam size monitors.

On the other hand, for high beam intensity the simulated IP vertical beam size is already significantly increased, even for our simplified model, if we assume the emittance values measured in the extraction line instead of those in the damping ring. Without improving the latter, a reduction of the beam intensity is necessary for reaching the design vertical spot size at the focal point.

In Figs. 4.17a and 4.17b the horizontal and vertical emittances increase monotonically with beam intensity, both in the damping ring, and even more in the extraction line. A larger vertical emittance has a direct first-order impact on the vertical beam size, but the increased horizontal emittance can also play an important role due to optical aberrations, which ultimately limit the spot size that can be achieved by a final focus system. The relevant aberrations are proportional to terms of the form $\theta_x^{*m}\theta_y^{*n}\delta^p$ where $\theta_x \equiv \sqrt{\varepsilon_x/\beta_x^*}$ and $\theta_y \equiv \sqrt{\varepsilon_y/\beta_y^*}$ denote the horizontal or vertical rms divergence at the focal point and δ the rms momentum spread, with m, n, and p being integers between 0 and 5. All three terms entering in the strength of the aberrations increase with beam intensity. In addition, the aberrations involving the horizontal emittance get weaker for a larger horizontal IP beta function.

The dependence on the horizontal emittance was investigated in simulations, by keeping the vertical emittance constant (at 12 pm) and by varying the horizontal emittance. The results are presented in Fig. 4.18. In case of the nominal optics, the vertical IP beam size increases by nearly 10% if the horizontal emittance is raised from 0.8 to 3 nm. By contrast, for the $10\beta_{\mathrm{x}}$ optics, this effect is much weaker, as expected.

An analysis of the intensity dependence was also performed for the ultra-low β_{y}^* optics. As the optical aberrations of the final focus scale with powers of the IP divergences, they should also be strong for this new optics. Lowering β_{y}^* by a factor 4 reduces the ideal minimum vertical beam size by a factor 2. In the absence of aberrations the rms spot size should be well below 20 nm (for the ATF2 vertical design emittance of 12 pm). Simulation results for the ultra-low β^* optics, shown in Fig. 4.19, indicate that even at low intensity the beam size will be much larger, and that, indeed, the intensity dependence will be significant.

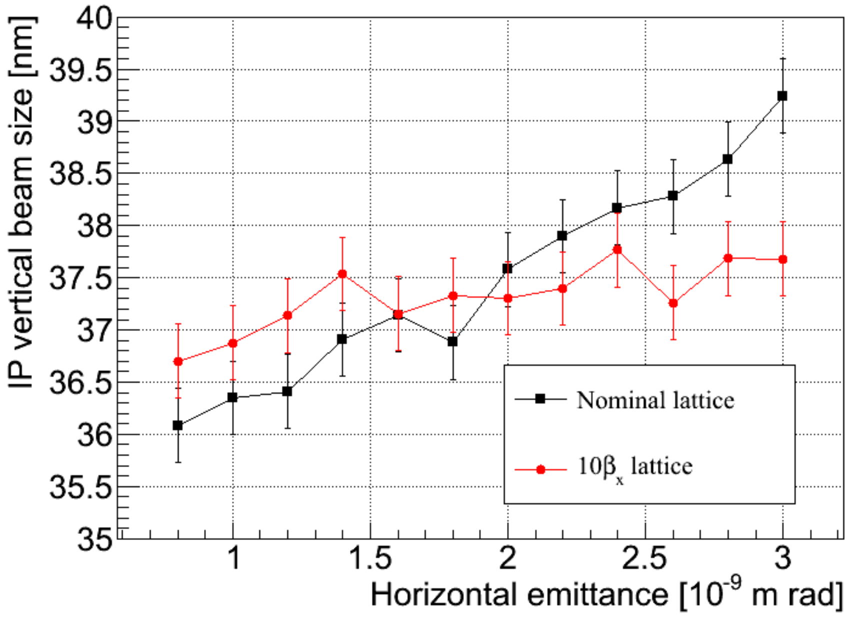

Figure 4.18: Vertical spot size vs. horizontal emittance.

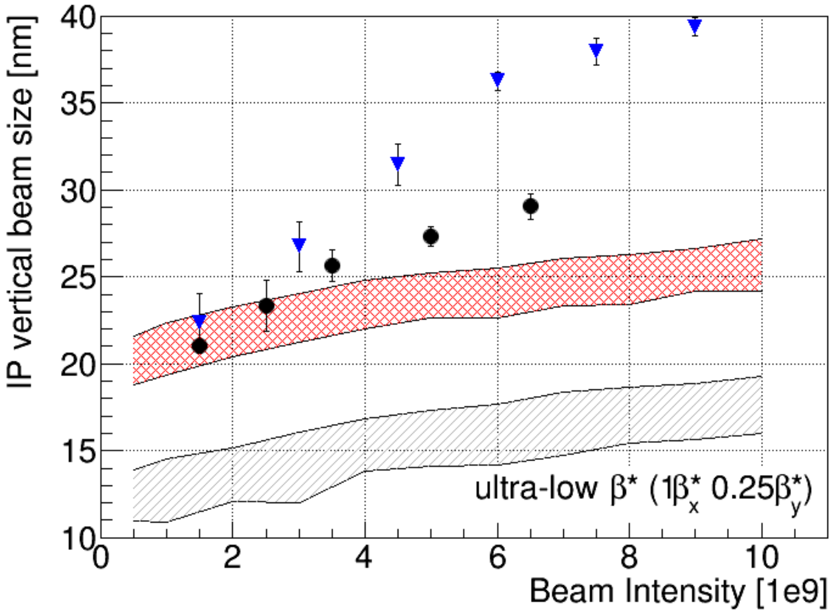

Figure 4.19: Vertical IP beam size for the ultra-low β^* optics in the beam intensity dependence. The points and bands convention is the same as in Fig. 4.17.

Conclusions

The increase of damping ring beam emittance and momentum spread due to IBS should not prevent one from reaching the design vertical beam size at the IP, even for the nominal beam intensity. The emittances measured in the extraction line, i.e. between the damping ring and the

ATF2 final focus, are much larger than those in the damping ring, by up to a factor 2 in both planes, and these show an even stronger dependence on the bunch intensity. This intensity-dependent emittance blow up could be due to nonlinear fields during extraction which would amplify the emittance growth and, especially, momentum-spread increase with intensity generated in the damping ring. Other possible explanations include the persistent presence of strong wakefields in this region of the machine and, perhaps, an insufficient control of spurious dispersion and coupling in the extraction line. Our simulations suggest that curing this emittance blow up is mandatory for reaching the ATF2 design vertical IP beam size at the design bunch intensity.

4.4. Tuning simulations with $10\beta_x^* 1\beta_y^*$ optics

In this section we describe the developed numerical tools based on MAD-X environment used to simulate the tuning of the ATF2 FFS considering the realistic machine errors applied to the machine model. The $10\beta_x^* 1\beta_y^*$ optics is used in this analysis in order to cross-check the results with the analogous study performed in SAD [101] environment and described in [74] and therefore prove that the developed tools are correctly implemented. The rms vertical beam size at the IP reported in [74] is 36.5 ± 0.9 nm.

The machine errors considered in this study concern the measured multipolar components and realistic errors of the transverse alignment, roll angle and strength of the ATF2 quadrupoles and sextupoles, see Table 4.6. These errors are randomly allocated to the ATF2 magnets following a Gaussian distribution. The analysis was performed using at least 100 random seeds for each simulation case. The rms vertical beam size at the IP, averaged over all simulation seeds, was a figure of merit in this study.

Table 4.6: List of the random machine errors included in the tuning simulations.

Horizontal misalignment	Δx [μm]	100
Vertical misalignment	Δy [μm]	100
Roll angle	$\Delta\theta$ [μrad]	200
Strength error	ΔK [%]	0.1
Multipolar field errors		according to [77, 78]

Machine tuning with the linear knobs

At the beginning of the machine tuning, the IP vertical beam size is dominated by the linear aberrations of beam waist longitudinal position shift, vertical dispersion, xy coupling and $p_x y$

coupling. These aberrations are graphically illustrated in Fig. 4.20 where phase space diagrams at the IP for lattices with and without errors are compared. For three of these aberrations, namely beam waist shift, vertical dispersion and $p_x y$ coupling, dedicated knobs can be constructed based on the deliberate horizontal and vertical displacements of the normal sextupole magnets. These knobs, referred to as Ay, Ey and C2, were calculated following the methods described in [102] and implemented into the simulation code. For the xy coupling the knob based on sextupole movements cannot be constructed due to the phase relations between the FFS and the IP. However, as it will be shown later, another method for correcting the xy coupling can be introduced.

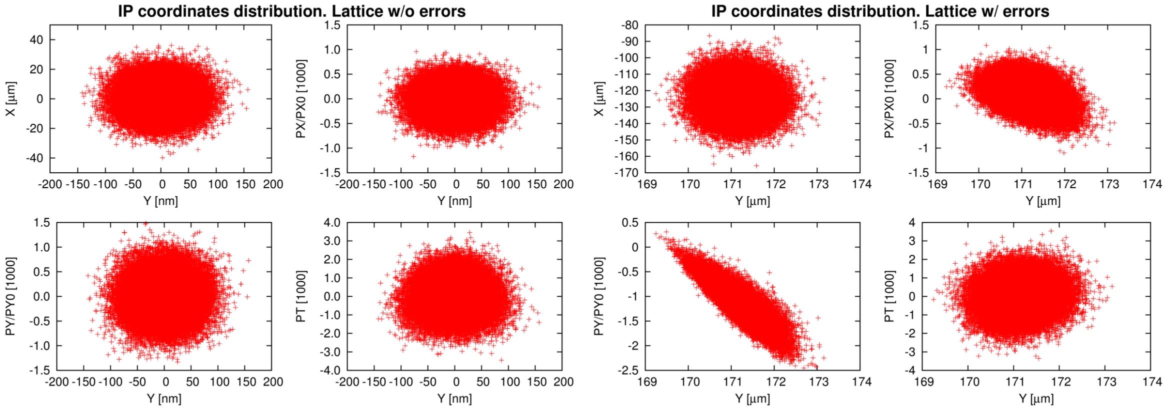

Figure 4.20: Phase space diagrams at the IP for lattices with (four plots on the right) and without (four plots on the left) errors. Please note the different units of the horizontal axes.

The histogram in the Fig. 4.21 summarizes the achieved vertical beam sizes at the IP after tuning the machines with the linear knobs only. The achieved average vertical beam size of 43.6 ± 8.3 nm is in good agreement with 43.5 ± 1.6 nm reported in [74].

Machine tuning with the linear and nonlinear knobs

Further beam size improvement can be obtained if the nonlinear knobs are applied. The vertical position of an electron at the IP can be expressed as a sum of the ideal beam transport term and the effects of aberrations represented as correlations between the vertical particle coordinate (y) and the other coordinates of this electron (x, p_x, p_y, δ_p):

$$\begin{aligned} y_i = \; & y_{i,0} + Y_1 x_i + Y_2 p_{x,i} + Y_4 p_{y,i} + Y_6 \delta_{p,i} + \\ & Y_{11} x_i^2 + Y_{12} x_i p_{x,i} + Y_{14} x_i p_{y,i} + Y_{16} x_i \delta_{p,i} + Y_{22} p_{x,i}^2 + \\ & Y_{24} p_{x,i} p_{y,i} + Y_{26} p_{y,i} \delta_{p,i} + Y_{44} p_{y,i}^2 + Y_{46} p_{y,i} \delta_{p,i} + Y_{66} \delta_{p,i}^2 + .., \end{aligned} \tag{4.3}$$

where Y_j, Y_{jk}, ... are the correlation coefficients of the first, second and higher orders representing the strength of a given aberration. The indexes j, k,... relate to coordinate indexes

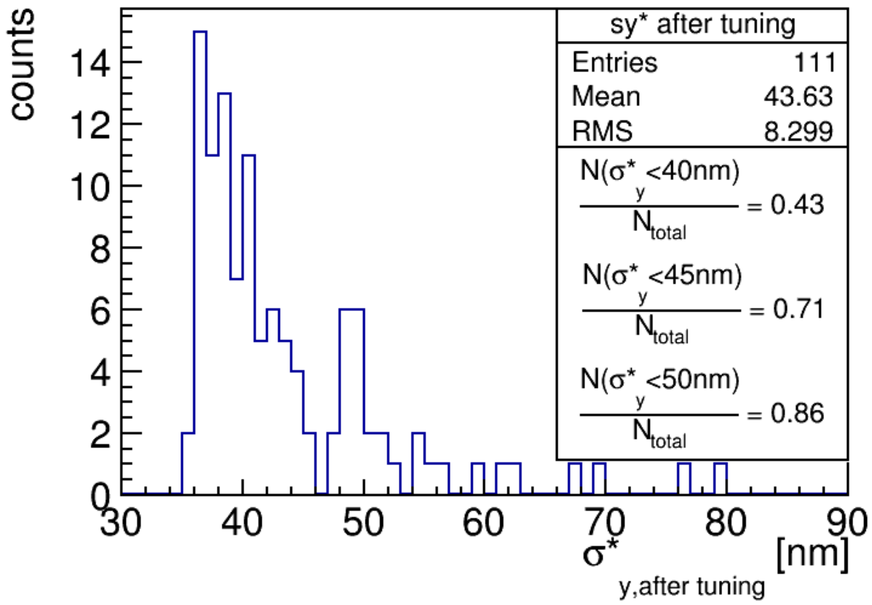

Figure 4.21: Distribution of the rms vertical beam sizes at the IP achieved after the machine tuning with linear knobs only.

(x, x', y, y', ct, δ), for instance:

$$\mathrm{Y26} = \frac{\langle (\mathrm{y} - \langle \mathrm{y} \rangle)\,(\mathrm{x}' - \langle \mathrm{x}' \rangle)\,(\delta - \langle \delta \rangle) \rangle}{\sqrt{\langle (\mathrm{x}' - \langle \mathrm{x}' \rangle)^2\,(\delta - \langle \delta \rangle)^2 \rangle}} \tag{4.4}$$

is the aberration coming from the correlation between vertical position (y), horizontal angle (x') and relative momentum deviation (δ) of the electrons at the IP. The most significant nonlinear aberrations were identified by calculating the beam size increase related to the given aberration averaged over 100 random simulation seeds, see Fig. 4.22. The following nonlinear knobs were calculated following the methods described in [74]: Y22, Y24, Y26, Y44, Y46, Y66. Figure 4.23 shows the results of tuning when the nonlinear knobs were included in the simulations. An IP vertical beam size improvement is observed, but the obtained value of 40.2 ± 5.4 nm does not meet the goal. A detailed investigation of beam size growth sources revealed a strong impact of xy correlation on the IP vertical beam size. This was solved by scanning the strength of QK3X skew quadrupole in the extraction line which is in good betatron phase with respect to the IP. After adding a routine for correcting the xy correlation, the average vertical beam size at the IP reached 36.8 ± 2.3 nm which agrees well with 36.5 ± 0.9 nm coming from [74], see Fig. 4.24. Therefore, we prove that the developed tools for simulating the machine tuning are working properly and can be used for studying the low β_y^* optics.

It is worth mentioning that the xy coupling correction method described in this section was later implemented in the operation of the ATF2 machine.

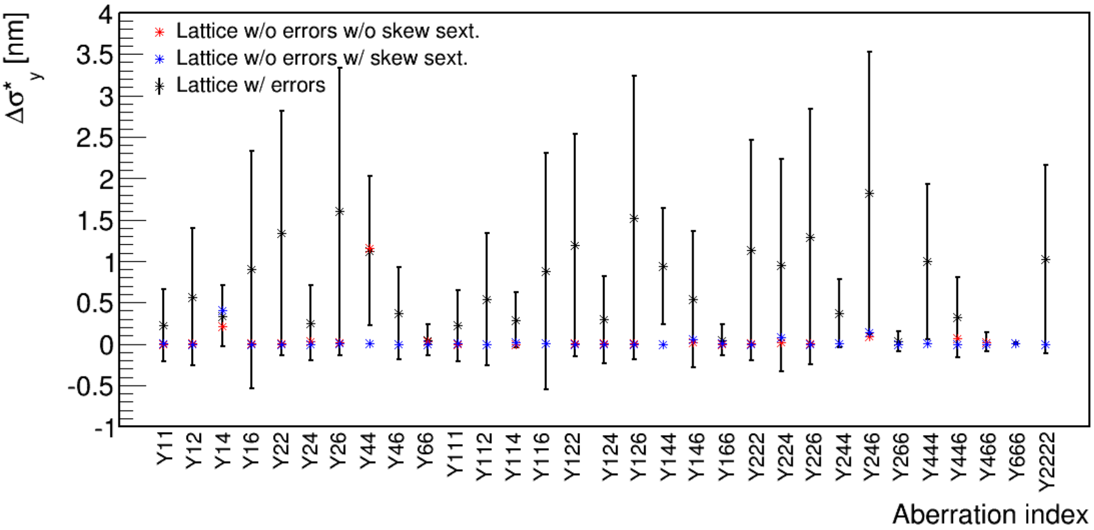

Figure 4.22: Effect of the nonlinear aberrations on the vertical beam size at the IP averaged over 100 random simulation seeds (black). The same calculation was also done for a design lattice without the alignment errors with the skew sextupoles turned on (blue) and off (red) which shows that the nonlinear aberrations are well corrected in the design setup.

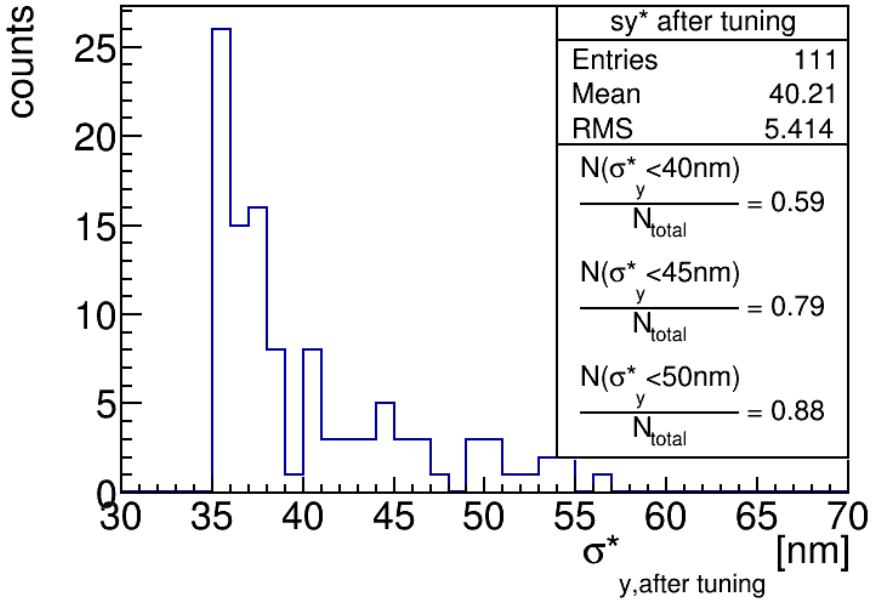

Figure 4.23: Distribution of the rms vertical beam sizes at the IP achieved after the machine tuning with linear and nonlinear knobs.

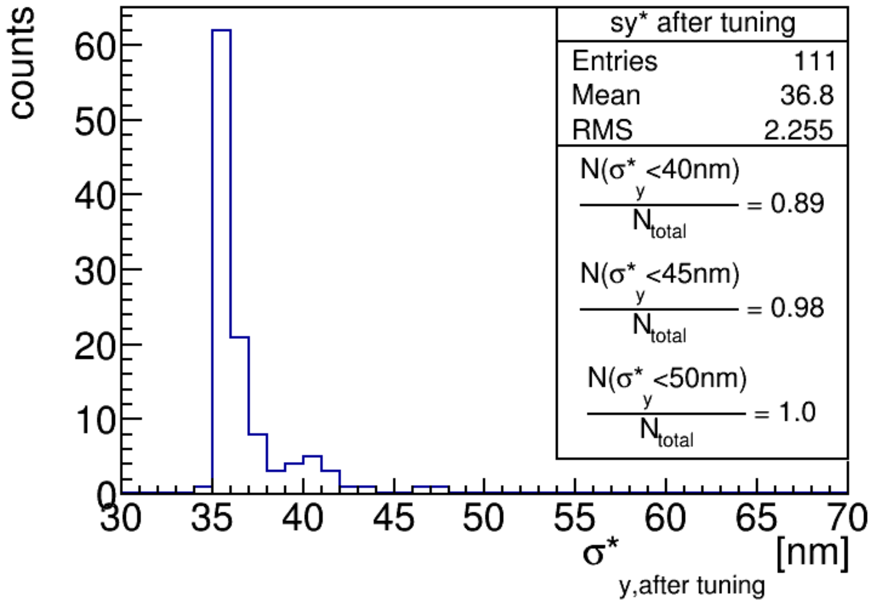

Figure 4.24: Distribution of the rms vertical beam sizes at the IP achieved after the machine tuning with linear and nonlinear knobs and $\mathrm{p_x y}$ *coupling corrections.*

Chapter 5

Half β_y^* experiment in the ATF2

One of the ATF2 goals is to reach the IP vertical beam size of 37 nm for the nominal β_y^* value of 100 μm. This goal was nearly reached in June 2014 and later in February 2016 when IP vertical beam sizes of 44 nm [84, 100] and 43 nm [84] were measured. These values represent the upper limit of the measured beam sizes as the systematic effect of the Shintake monitor was not estimated [103]. The β_x^* values for these measurements were about 100 mm (25 times the nominal β_x^*) and about 53 mm (13 times the nominal β_x^*), respectively. Moreover, the bunch intensity was 10^9 e^- (5 times lower than nominal) in order to weaken the effects of wakefields and to reduce the beam emittance and the momentum spread.

In December 2014 we started the experimental works towards lowering the β_y^* value by a factor 2 (half β_y^*) in the ATF2. The objectives of the initial low β_y^* experiments were to gain the experience with the beam operation in the machine, the optics implementation and control, and to identify potential obstacles and address them. Achieving this, the complete IP beam tuning with half β_y^* optics was performed in February 2016. The applied β_x^* values were 40 mm ($10\beta_x^*$) and 100 mm ($25\beta_x^*$) and the bunch intensity was 10^9 e^-. The goal of this experiment was to explore the limiting factors in the beam focusing at the IP and to test the performance of more chromatic FFS. Reaching a lower vertical beam size at the IP than for the nominal β_y^* optics would prove that the FFS effects are well understood and controlled. In the opposite case a further investigation will be required in order to find and mitigate the sources of the IP beam size growth.

In the following sections we describe in detail the machine tuning with the half β_y^* optics done over 8 machine-shifts (8 hours each) in the last week of February 2016 operation. The measured beam sizes are compared with the results of the tuning simulations. The results presented in this chapter were also published in [104].

5.1. Machine tuning

Machine tuning is a process of adjusting the beamline parameters in order to obtain beam parameters as close as possible to the design. It starts with the beam steering, a procedure of finding the beam trajectory that minimises the offset at the BPMs and brings the beam to the IP. This is achieved using the steering dipoles and by deliberate quadrupole movements in the transverse plane. The following tuning procedures, namely the dispersion matching, coupling correction, optics matching and IP beam tuning are described in detail in the following sections.

5.1.1. Dispersion matching

Dispersion is measured in the ATF2 beamline by changing the beam energy in the damping ring and observing the orbit change at the BPMs. The energy change is introduced by shifting the damping ring RF frequency by ± 3 kHz (714 MHz is the nomonal RF frequency). For the DR momentum compaction factor of 0.00214, a relative beam energy change is then of about $\pm 0.2\%$. Such a generated orbit change is proportional to the dispersion at a given location (see Eq. 2.1) and can be reconstructed by fitting a betatron oscillation to the observed BPM responses.

Horizontal dispersion is corrected by adjusting the strength of two inflector quadrupoles (QF1X and QF6X). Figure 5.1 shows the measured and fitted horizontal dispersion, before and after correction, compared with a design dispersion.

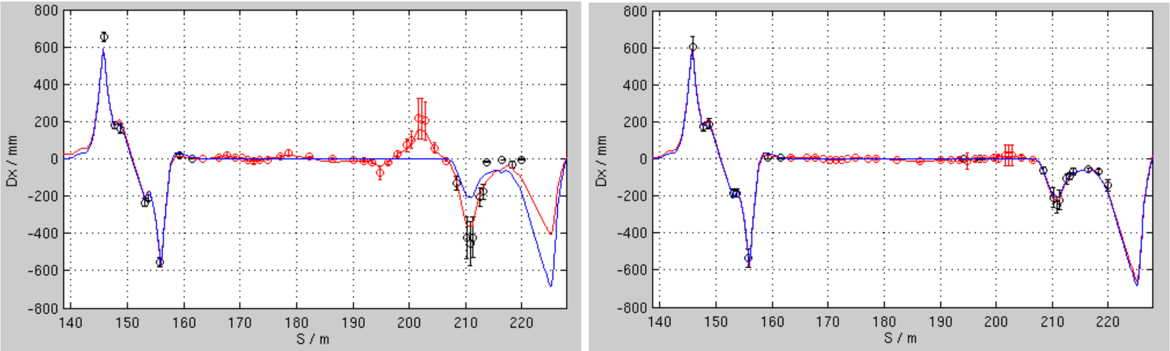

Figure 5.1: Measured (black cicrcles), fitted (red) and design (blue) horizontal dispersion in the ATF2 before (lef) and after (right) correction.

The ATF2 line is by design free of vertical dispersion, so any observed vertical dispersion is anomalous and requires correction. The observed vertical dispersion is either in the final doublet phase or in the IP phase, and only one can be corrected at a time using the Σ-knob. The usual practice is that the vertical dispersion is initially corrected at the mOTR location in order to perform reliable emittance measurements and later the FFS dispersion is minimised, see Fig. 5.2.

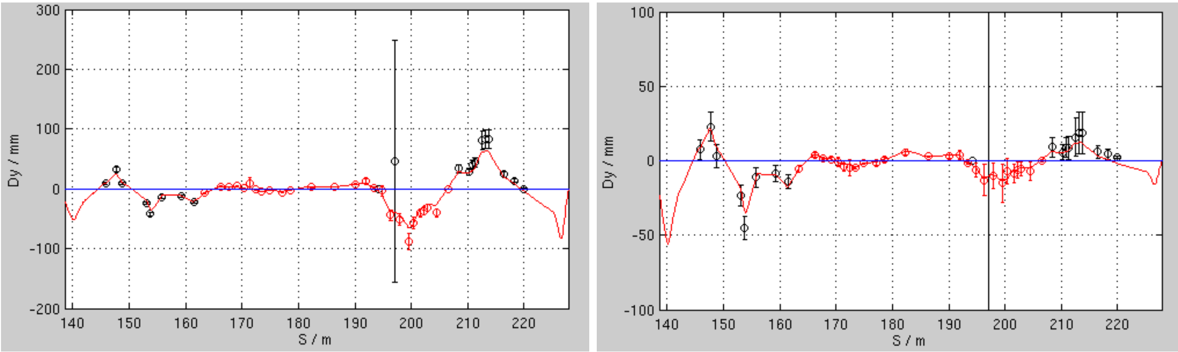

Figure 5.2: Measured (black cicrcles), fitted (red) and design (blue) vertical dispersion in the ATF2 corrected in the OTRs region (lef) and in the FFS region (right). Please mind the different vertical scales.

5.1.2. Coupling correction

The xy coupling correction is performed by scanning the strength of four skew quadrupoles in the extraction line and by applying the Δ-knob with the vertical emittance measured by the mOTR system being a figure of merit. Figure 5.3 shows the scans performed to correct the coupling.

5.1.3. Emittance measurement

In the last week of February 2016 operation the vertical emittance was measured in the damping ring using the X-ray Synchrotron Radiation (XSR) monitor and in the extraction line using the mOTR system. Table 5.1 contains the measured values of the emittance. According to the known issues of the OTR monitors in the ATF2 [105], the large difference in the vertical emittance might imply that the mOTR measurement is biased with a large unknown systematic error and cannot provide a reliable estimate of the emittance [105, 106]. On the other hand the XSR measurement does not represent the extraction line emittance as some emittance growth is expected after beam extraction from the damping ring [107]. A new method for IP vertical emittance evaluation was therefore introduced and is described in the next section.

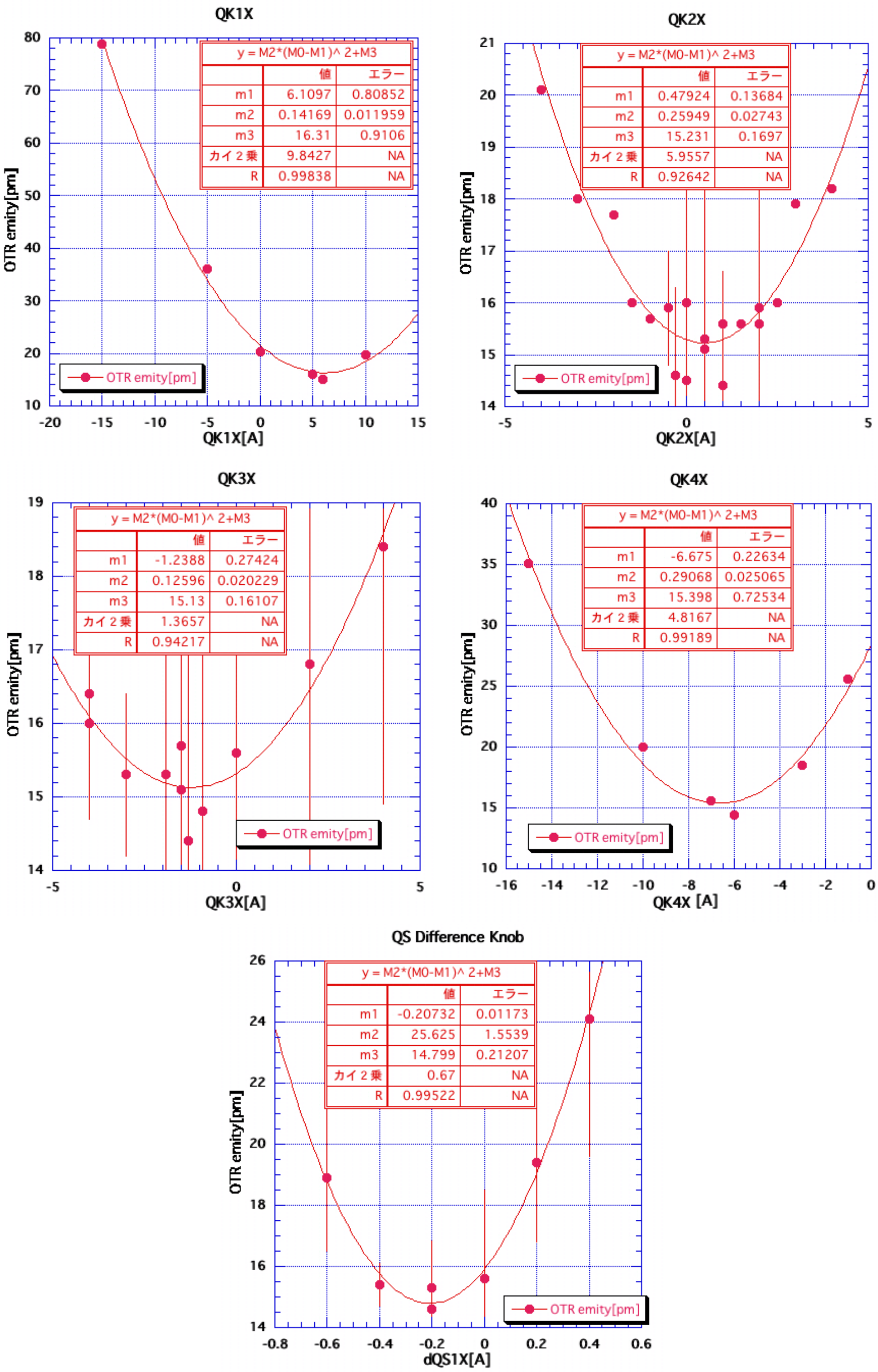

Figure 5.3: Coupling correction in the extraction line. Top left: QK1X scan, top right: QK2X scan, middle left: QK3X scan, middle right: QK4X scan, bottom: Δ-knob scan.

5.1.4. Optics matching

Six quadrupole magnets located at the entrance of the final focus line are used to match the beam parameters at the IP. The required quadrupole strengths are calculated using the machine

Table 5.1: Vertical beam emittance measured in the damping ring (XSR) and in the extraction line (mOTR) in the last week of February 2016 operation.

	ε_{y} [pm]
damping ring (XSR)	4.4 ± 0.4
extraction line (mOTR)	15.3 ± 1.5

model. However, for every beam operation the initial beam parameters at the extraction from the damping ring are slightly different which then affects the matching solution. Therefore, the precise matching of the beam parameters at the IP is done in two iterations. In the first iteration it is assumed that the initial beam parameters are exactly the same as in the model and the calculated solution is applied to the machine. Then the beam parameters at the IP are measured. If the measured values do not meet the matching target, the matching solution is recalculated taking into account the observed discrepancy. The procedures for precise measurement of the beam parameters at the IP are described below.

Beam diagnostics at the IP

Quadrupole scanning is a widely used method (also in ATF2 [108]) for measuring the transverse beam parameters. Since we are interested in the beam parameters at the IP, the FD quadrupoles strength is varied and both horizontal and vertical beam sizes are measured using the IP wire scanner. An increase of the transverse beam size due to the beam waist shift is defined by the beam divergence, so the beam parameters can be resolved by fitting Eq. (5.1) to the square of the measured beam size $\sigma^2_{x,y}$, where $\varepsilon_{x,y}$ stands for the transverse emittance, $\beta^*_{x,y}$ for the IP β value and $\Delta f_{x,y}$ for the longitudinal distance between the wire position and actual beam waist position:

$$\sigma^2_{x,y} = \varepsilon_{x,y}\beta^*_{x,y} + \frac{\varepsilon_{x,y}}{\beta^*_{x,y}}(\Delta f_{x,y})^2. \tag{5.1}$$

Similar to the method described in [108] the measured beam size has to be corrected for residual dispersion at the IP and for the geometric properties of the wire, as given in Eq. (5.2):

$$\sigma^2_{\mathrm{x,y}} = \sigma^2_{\mathrm{x,y,\ measured}} - \left(\frac{\sigma_{\mathrm{E}}}{\mathrm{E}}\right)^2 \eta^2_{\mathrm{x,y}} - \left(\frac{\mathrm{d}}{4}\right)^2, \tag{5.2}$$

where $\frac{\sigma_{\mathrm{E}}}{\mathrm{E}}$ is the relative energy spread (equal to 0.0006 for low beam intensity of 10^9 e^-/bunch) and $\mathrm{d} = 5$ μm is the carbon wire diameter.

The minimum measurable beam size with the wire scanner is about half of the wire diameter, which is not an obstacle for horizontal beam size measurement (between 6 μm and 10 μm is the usual value in recent operation). However, the vertical beam size is expected to be smaller than 1 μm even for the beginning of the operation and it cannot be precisely measured when the beam waist is at the wire location. Instead, the beam waist is shifted out of the the wire location so that the beam divergence can be resolved using Eq. (5.3):

$$\sigma_y^2 \approx \frac{\varepsilon_y}{\beta_y^*}(\Delta f_y)^2. \tag{5.3}$$

The evaluation of the vertical beam divergence is presented in Fig. 5.4.

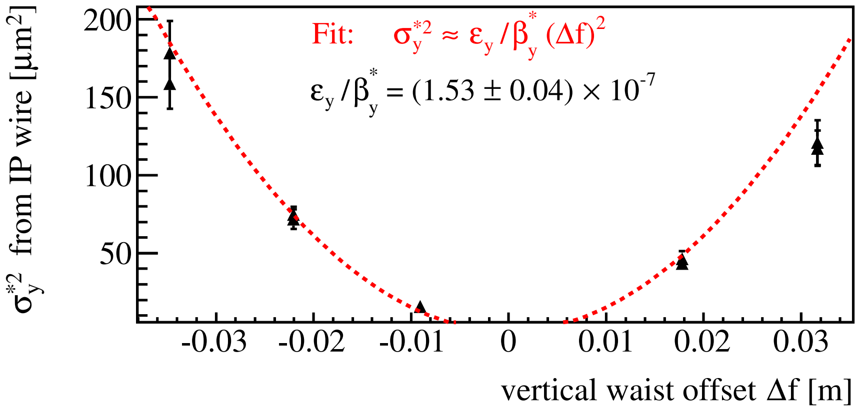

Figure 5.4: QD0FF scan for vertical beam parameters evaluation at the IP from the last week of February 2016 operation. Lower cut for the beam size measurement was set to 3 μm. Only the ratio ε_y/β_y^* can be resolved. The effects of dispersion and wire properties are subtracted. Change of the β_y^* value for the maximum waist offset is less than 5%.

Knowledge of β^* values is necessary for judging if the desired optics was correctly implemented. For the horizontal plane both emittance and β^* can be resolved but in the vertical plane the β^* value can be calculated only if the vertical emittance is known. Table 5.2 contains the measured values of emittance (see Table 5.1) and corresponding values of β_y^*. The large difference in the β_y^* values comes from the difference in the emittance values. This issue was solved by introducing a new method for the vertical emittance evaluation.

Table 5.2: β_y^* evaluation based on two emittance measurements and QD0FF scan performed in the last week of February 2016 operation. The matching target was $\beta_y^* = 50$ μm.

	ε_y [pm]	β_y^* [μm]
DR (XSR)	4.4 ± 0.4	29.0 ± 3.0
EXT (mOTR)	15.3 ± 1.5	100.0 ± 10.1

New method for IP vertical emittance measurement

The quadrupole scan method cannot be applied in the vertical plane to resolve both the emittance and β^* value since the vertical beam size at the waist is too small to be measured by the wire scanner. This obstacle can be overcome by using the Shintake monitor (see Section 3.5) located at the IP for measuring the vertical beam size. From the available laser crossing angle modes the 30 degree mode with a dynamic range of 85 nm to 340 nm is the most precise and its systematic errors can be accurately measured, so this mode should be chosen to perform the scan. Such a narrow dynamic range requires very fine, well controlled beam waist shifts of less than 5 mm. This cannot be achieved by varying the strength of the QD0FF magnet, so the vertical beam waist position knob (the Ay knob) is used instead. The relation between Ay knob amplitude and beam waist offset is depicted on Fig. 5.5.

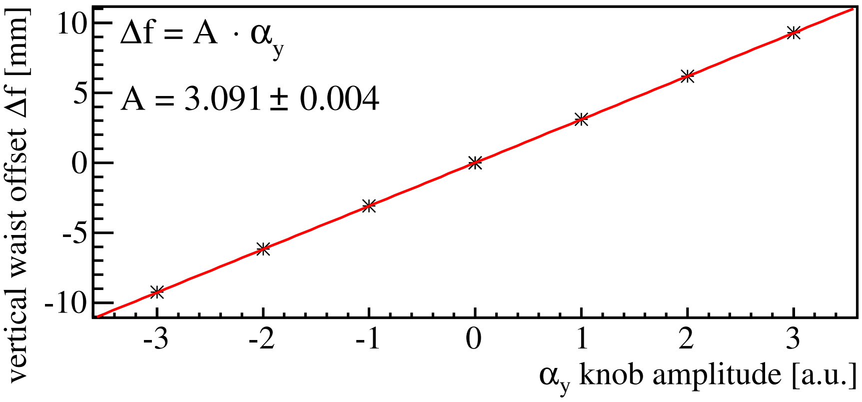

Figure 5.5: The relation between Ay knob amplitude and beam waist offset derived from the simulations. A is the proportionality coefficient.

To perform a scan the optics were rematched with target β^* values of $\beta_x^* = 40$ mm and $\beta_y^* = 2.5$ mm (β_y^* being 25 times larger than nominal) in order to increase the vertical beam size at the IP such that it can be measured with the 30 degree mode of the Shintake monitor. The measured vertical beam size data were fitted (see Fig. 5.6) with the formula (Eq. (5.4)) coming from combining Eq. (5.1) with Eq. (3.2):

$$M = C_{30} \cos(30^\circ) \exp\left[-2k_y^2 \left(\varepsilon_y \beta_y^* + \frac{\varepsilon_y}{\beta_y^*} (A\Delta\alpha_y)^2\right)\right]. \tag{5.4}$$

The modulation reduction factor in 30 degree mode (C_{30}) was estimated in the same beam operation in the following way. The optics was rematched with target β^* values of $\beta_x^* = 40$ mm and $\beta_y^* = 50\ \mu$m in order to decrease the vertical beam size such that it can be measured both in 30 and 174 degree mode. The modulation was then measured by taking 10 consecutive Shintake

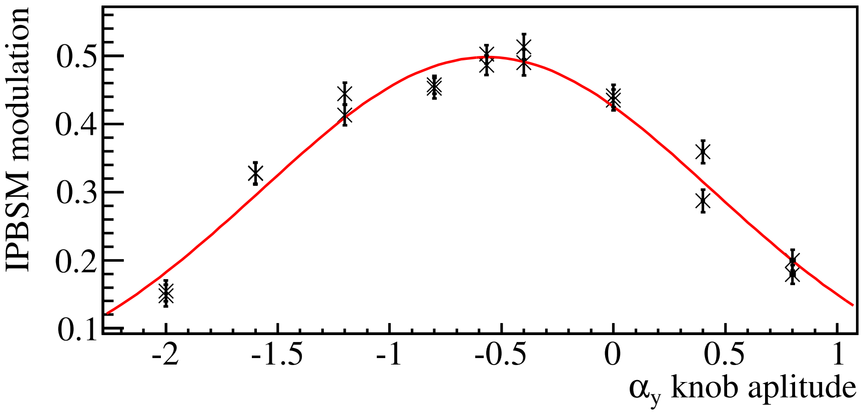

Figure 5.6: Measured modulation during the Ay scan to resolve the vertical emittance at the IP and the β_y^* *value using the Shintake monitor in 30 degree mode.*

monitor scans, first in 174 degree mode: $M_{174,\text{meas.}} = 0.374 \pm 0.016$ (stat.); and immediately after in 30 degree mode: $M_{30,\text{meas.}} = 0.709 \pm 0.016$ (stat.). Using the modulation in 174 degree mode ($M_{174,\text{meas.}}$) the corresponding beam size (σ_{174}) was calculated according to:

$$\sigma_{174} = \frac{1}{2k_y}\sqrt{2\ln\left(\frac{C_{174}\left|\cos\left(174^\circ\right)\right|}{M_{174,\text{meas.}}}\right)}, \tag{5.5}$$

where C_{174} is the modulation reduction factor in 174 degree mode. The uncertainty of the beam size evaluation is given by:

$$\Delta\sigma_{174} = \frac{1}{4k_y^2\,\sigma_{174}}\sqrt{\left(\frac{\Delta M_{174,\text{meas.}}}{M_{174,\text{meas.}}}\right)^2 + \left(\frac{\Delta C_{174}}{C_{174}}\right)^2}, \tag{5.6}$$

where $\Delta M_{174,\text{meas.}}$ and ΔC_{174} stand for the uncertainties of $M_{174,\text{meas.}}$ and C_{174} respectively. The modulation reduction factor of the Shintake monitor in 174 degree mode (C_{174}) cannot be directly measured and its estimation requires a complex offline analysis. An attempt at estimating C_{174} is described in the PhD thesis of J. Yan [53], but in our study we assume $C_{174} = 1^{+0.0}_{-0.1}$ which allows us to calculate the upper limit of the measured beam size and accounts for possible hardware imperfections of the Shintake monitor causing a decrease of the measured modulation. Such an approach is applied to all beam size calculations (in 174 degree mode) shown in this chapter.

The expected modulation in 30 degree mode was calculated in the following way:

$$\begin{aligned} M_{30,\text{exp}}(\sigma_{174}) &= \cos\left(30^\circ\right)\exp\left[-2\left(k_y\sigma_{174}\right)^2\right] \\ &= 0.81 \pm 0.01 \end{aligned} \tag{5.7}$$

and compared with a measured value ($M_{30,\text{meas}}$). The ratio of these two is the modulation reduction factor in 30 degree mode:

$$C_{30} = \frac{M_{30,\text{meas}}}{M_{30,\text{exp}}(\sigma_{174})} = 0.87 \pm 0.02. \tag{5.8}$$

The vertical beam parameters at the IP, namely vertical emittance and β_y^* value, were resolved from fitting α_y scan data with the formula given in Eq. (5.4), as presented in Fig. 5.6. In our case the results are: $\varepsilon_y = 7.7 \pm 0.3$ pm and $\beta_y^* = 2.81 \pm 0.12$ mm (matching target was $\beta_y^* = 2.5$ mm). The vertical emittance measured with this method is compared to the XSR measurements in the DR and mOTR measurements in the EXT line during the same week of operation; see Fig. 5.7. A vertical emittance growth between the DR and the IP nearly by a factor 2 is observed. These data also confirm that there might be some issues with the mOTR system.

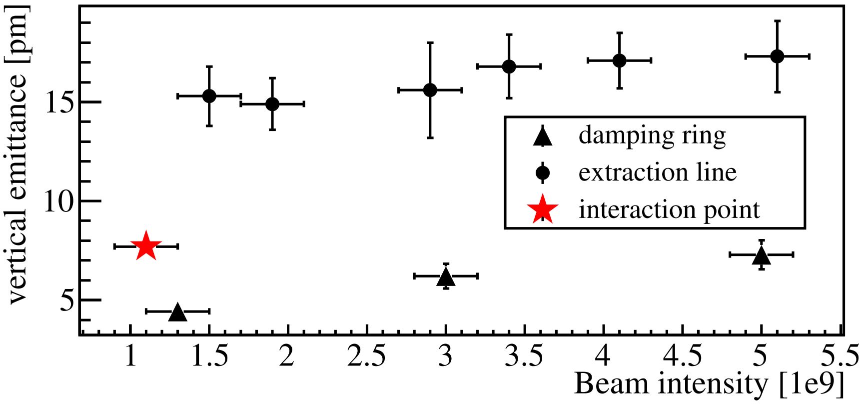

Figure 5.7: Comparison of measured vertical emittance at 3 locations using different methods versus beam intensity. Emittance at the IP was measured only for one beam intensity but this study is ongoing.

This vertical emittance was then used to verify if the half β_y^* optics were correctly applied. The vertical beam divergence squared measured by scanning QD0FF (Fig. 5.4) was $\varepsilon_y/\beta_y^* = (1.53 \pm 0.04) \cdot 10^{-7}$ which gives $\beta_y^* = 50 \pm 2\ \mu$m. The β_y^* value agrees with the matching target (50 μm) proving that the desired optics were correctly applied to the machine.

5.1.5. Beam tuning at the IP

Knowing that the applied optics (half β_y^*, $10\beta_x^*$) is correct, the IP beam tuning was performed according to procedures described in Section 3.4. The beam size improvement versus the applied knob is depicted in Fig. 5.8. One can see that the tuning efficiency is low which probably means that the initial knob settings were close to optimum and any possible further beam size improvement was spoiled by other sources of IP beam size growth. The IP beam size increase

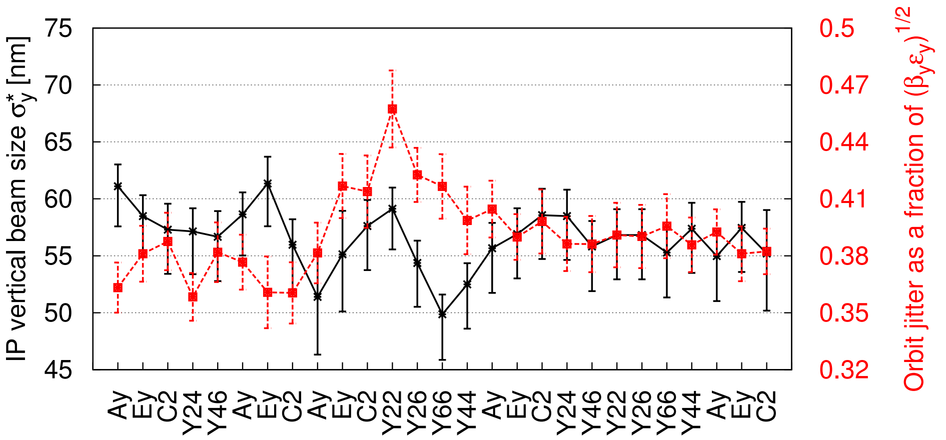

Figure 5.8: IP vertical beam size (black) and the orbit jitter (red) versus the beam tuning in half β_y^*, $10\beta_x^*$ optics. Points representing the beam size correspond to the optimum knob setting and error bars account for the uncertainty of finding the optimum knob setting by fitting the knob scan data (as in Fig. 5.6) and for the systematic error of the Shintake monitor as described in Section 5.1.4.

coincides with large orbit position jitter in the final focus line (also shown in Fig. 5.8) suggesting that the orbit position jitter in the final focus line affects the IP beam size and tuning efficiency. Other possible reasons for low tuning efficiency are: Shintake monitor fluctuations, beam intensity fluctuations and wakefields. Shintake monitor fluctuations are included in the uncertainty of the beam size measurement (an error of the modulation reduction factor as described in Section 5.1.4). Beam intensity fluctuations increase the errors of the Shintake monitor and contribute to the wakefield effect on the beam size. The effect of beam intensity fluctuations are minimised by selecting only the bunches with an intensity of $(0.8, 1.2) \cdot 10^9\ \mathrm{e}^-$ to be measured by the Shintake monitor. We express the wakefield contribution to the IP vertical beam size as

$$\sigma_y^* = \sqrt{\sigma_y^*(0)^2 + \mathrm{w}^2 \mathrm{N}_\mathrm{b}^2}, \tag{5.9}$$

where $\sigma_y^*(0)$ is the zero-intensity (no wakefield effect) IP vertical beam size, w the wakefield contribution, and $\mathrm{N_b}$ the bunch intensity [69]. The contribution of wakefields on the IP vertical beam size for half $\beta_y^*, 10\beta_x^*$ optics was investigated by measuring the IP vertical beam size for 3 bunch intensities: $1 \cdot 10^9\ \mathrm{e}^-$, $2 \cdot 10^9\ \mathrm{e}^-$ and $3 \cdot 10^9\ \mathrm{e}^-$, see Fig. 5.9. The obtained value of $\mathrm{w} = 22 \pm 1 \frac{\mathrm{nm}}{10^9\ \mathrm{e}^-}$ corresponds well with the simulations described in [84]. In that study the known wake potentials of beamline cavities, flanges and bellows were combined with the beam orbit jitter in the final focus line in order to investigate their impact on the IP beam sizes. For a beam orbit jitter of 40% of the beam size and half $\beta_y^*, 10\beta_x^*$ optics the estimated value of w is $18 \frac{\mathrm{nm}}{10^9\ \mathrm{e}^-}$ [84]. Small discrepancy with respect to the measured value suggests that some wakefield sources were not implemented in the simulation. The wakefield contribution for bunch intensity in the range $(0.8, 1.2) \cdot 10^9$ e^- does not explain the discrepancy between the measured and expected IP vertical beam sizes. Moreover, in consequence of reducing the bunch intensity the BPMs resolution is worsened and the signal-to-noise ratio of the Shintake monitor is increased. For the nominal β_y^* the IP vertical beam size increase due to wakefields combined with the final focus line beam jitter of 40% of the beam size is $15\frac{\mathrm{nm}}{10^9\,\mathrm{e}^-}$ [84] showing that the wakefield contribution is enhanced when the β_y^* value is lowered. More systematic measurements of the wakefield contribution to the IP vertical beam size for different optics is foreseen for autumn 2016 operation in the ATF2. After the tuning, the final beam size was measured by taking 10 consecutive beam size measurements, the result is given in Table 5.3.

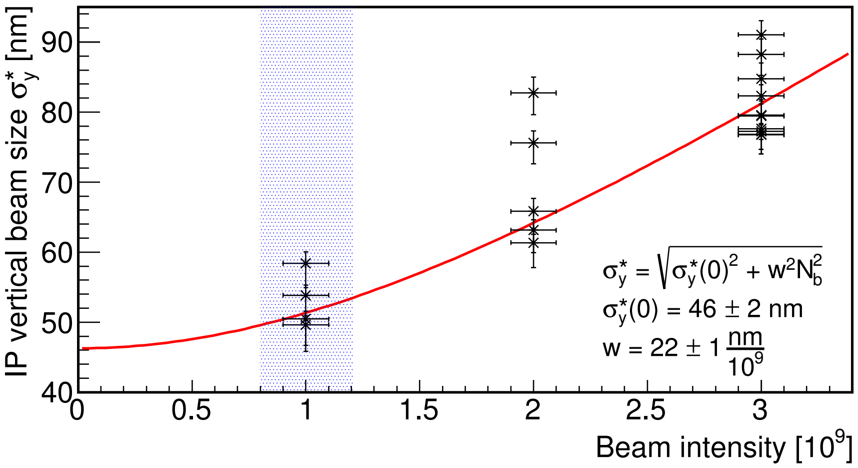

Figure 5.9: Intensity dependence of the IP vertical beam size for half β_y^*, $10\beta_x^*$ optics. Black points stand for the measured beam size, red curve for the fit according to Eq. (5.9) and blue band for the bunch intensity restriction of the tuning and final beam size measurement.

In the next step, the horizontal β_x^* was relaxed to $25\beta_x^*$. The beam tuning was again performed (see Fig. 5.10) and the final beam size was measured as in the previous case (see Table 5.3). For these optics we have observed an increased tuning efficiency and the measured IP vertical beam size is lower by 12% with respect to the IP vertical beam size for half β_y^*, $10\beta_x^*$ optics. Relaxing the horizontal optics reduces the sensitivity to nonlinear aberrations but does not help with the other beam size growth sources. Moreover, for for larger β_x^* value the larger IP horizontal beam size stronger affects the IP vertical beam size in the case of xy coupling.

5.2. Beam tuning simulations

Tuning simulations using the MAD-X [76] model of the ATF2 beamline were performed in order to understand the measured beam sizes (see Table 5.3). The errors applied to the magnets

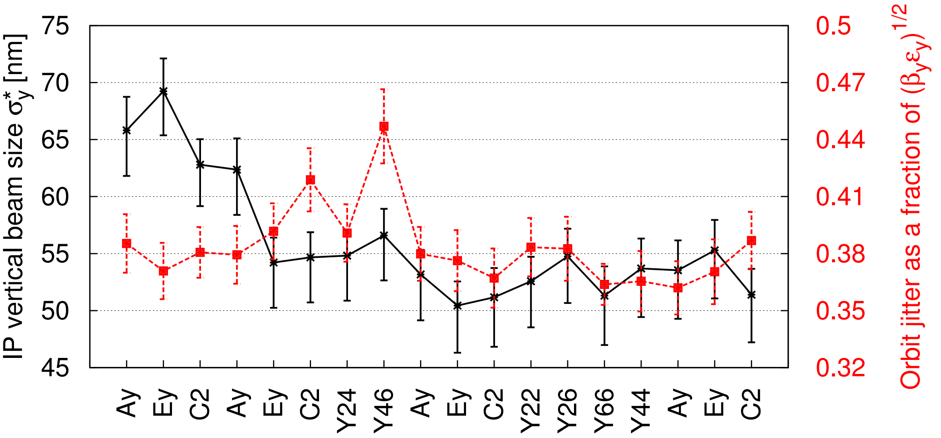

Figure 5.10: IP vertical beam size (black) and the orbit jitter (red) versus the beam tuning in half β_y^*, $25\beta_x^*$ optics. Points representing the beam size correspond to the optimum knob setting and error bars account for the uncertainty of finding the optimum knob setting by fitting the knob scan data (as on Fig. 5.6) and for the systematic error of Shintake monitor as described in Section 5.1.4.

Table 5.3: Measured IP vertical beam size after the tuning for half β_y^*, $10\beta_x^*$ optics and half β_y^*, $25\beta_x^*$ optics compared with the design values assuming the measured vertical emittance.

optics	$\sigma^*_{\mathrm{y,meas.}}$ [nm]	$\sigma^*_{\mathrm{y,design}}$ [nm] (for $\varepsilon_y = 7.7$ pm)
half β_y^*, $10\beta_x^*$	58^{+4}_{-5}	21
half β_y^*, $25\beta_x^*$	51^{+5}_{-6}	20

in the ATF2 model concern the measured multipolar components and realistic random errors on the transverse alignment, roll angle and strength of the ATF2 magnets. The usually assumed values of errors [74] are 100 μm for transverse alignment, 200 μrad for roll angle and 0.1% for strength. In our simulations we also consider misalignments larger by 50% and 100% and multipolar errors larger by factors of 3 and 5. We performed the simulations in two cases in terms of the orbit correction: with orbit correction given by the MAD-X `CORRECT` [76] command, which uses the beamline BPMs and correctors, and without any simulated orbit correction. The BPMs used for the orbit correction are centered with the adjacent magnets with additional position error of 10 μm which accounts for the mounting precision and readout errors. The orbit correction is applied only once just after misaligning the magnets as the machine drifts are not simulated. The knobs used for the tuning simulations are defined in the same way as for the actual machine and applied in the same order and number.

The IP beam size is calculated from the electron distribution at the IP convoluted with the Shintake monitor fringe pattern. Additionally, the beam size growth coming from the effect of wakefields combined with the beam angular jitter at the IP and the Shintake monitor performance is included by adding in quadrature the corresponding random errors of 18 ± 4 nm (Gaussian distribution) [84] and ±8 nm (uniform distribution) [74] respectively. 100 seeds were used for every considered machine setup. The results are summarized in Table 5.4 where IP vertical beam size is represented by the mean value over all seeds ($\sigma^*_{\mathrm{y,sim.}}$) and the spread of the results is given by the standard deviation of the beam size data.

Table 5.4: Mean and standard deviation of the IP vertical beam size obtained from the tuning simulations for half β^*_{y}, $10\beta^*_{\mathrm{x}}$ (10x0.5) and half β^*_{y}, $25\beta^*_{\mathrm{x}}$ (25x0.5) optics for various sets of machine errors.

	misalignments			multipolar	$\sigma^*_{\mathrm{y,sim}}$ w/o orbit corr.		$\sigma^*_{\mathrm{y,sim}}$ w/ orbit corr.	
	Δx	Δy	$\Delta\theta$	errors	half β^*_{y}, $10\beta^*_{\mathrm{x}}$	half β^*_{y}, $25\beta^*_{\mathrm{x}}$	half β^*_{y}, $10\beta^*_{\mathrm{x}}$	half β^*_{y}, $25\beta^*_{\mathrm{x}}$
case	[μm]	[μm]	[μrad]		[nm]	[nm]	[nm]	[nm]
nominal errors	100	100	200	x1	39 ± 10	38 ± 7	32 ± 3	32 ± 3
misalign. x1.5	150	150	300	x1	52 ± 22	49 ± 13	36 ± 8	35 ± 5
misalign. x2.0	200	200	400	x1	67 ± 30	62 ± 20	39 ± 10	40 ± 8
mults x3	100	100	200	x3	44 ± 10	46 ± 10	38 ± 6	37 ± 5
mults x5	100	100	200	x5	61 ± 14	54 ± 11	45 ± 8	44 ± 7
misalign. x1.5, mults x3	150	150	300	x3	62 ± 24	55 ± 16	42 ± 7	42 ± 8
misalign. x2.0, mults x5	200	200	400	x5	85 ± 33	74 ± 22	54 ± 12	55 ± 11
experiment	-	-	-	-	-	-	$(58^{+4}_{-5})^{a}$	$(51^{+5}_{-6})^{\mathrm{a}}$

---

[a] Orbit correction in the experiment is different than in the simulation.

5.3. Discussion of the results

In the case with the orbit correction included in the simulations the obtained beam sizes (last two columns of Table 5.4) are always lower than in the experiment. If the ATF2 orbit correction was as good as in the simulations, the multipolar errors would require a considerably larger factor which would be unrealistic. This suggests that the orbit correction applied at the ATF2 might not be very efficient and its improvement could help to reach low beam sizes. In the ATF2 the orbit correction is done manually, first (at the beginning of beam operation) to minimise the beam offset at the BPMs and later during the beam tuning individual correctors are scanned to minimise the IP beam size. Performance of the initial orbit steering depends on the beamline elements alignment and BPMs calibration. The mechanical alignment of the final focus system magnets was done in October 2015 and the BPMs calibration was done in December 2015. The initial steering degrades with time due to machine drifts and jitters. Some sources of machine drifts and jitters are related to the water cooling system and air temperature in the damping ring [84]. In the ATF2 there is also an orbit feedback system that keeps the constant beam position at the selected BPM. However, this system is slow and sensitive to the optics match constraints and its performance is spoiled when the beam is operated at low intensity.

The simulated beam sizes better correspond to the experiment when the orbit correction is not applied (see Fig. 5.11) which may reflect limitations of the ATF2 orbit correction methods. For the nominal machine errors the simulated beam sizes are 33% lower than in reality for half β_y^*, $10\beta_x^*$ optics and 25% lower for half β_y^*, $25\beta_x^*$ optics. As the machine errors increase, the simulated beam sizes get closer to the measured values, especially for the following cases: misalign. x1.5; mults x5; misalign. x1.5, mults x3 (see Fig. 5.11). The combined effect of larger magnet misalignments and stronger multipolar errors is a possible explanation of the beam sizes measured in ATF2.

The strong effect of the nonlinear aberrations was observed in the experiment by switching off the skew sextupole magnets. When the skew sextupoles (used for the following nonlinear knobs: Y22, Y26, Y44, Y66) were turned off after the tuning, the measured beam sizes increased by about 20 nm for both optics [109, 110]. Some of this beam size increase can come from the magnetic feeddown effect due to the horizontal and vertical offsets at the skew sextupoles. However, the beam based alignment of the skew sextupoles was done shortly before these beam operations and the linear knobs correction was usually small after these nonlinear knobs which suggest that most of this beam size increase comes from the nonlinear aberrations that seem to be stronger than anticipated in the ATF2. The source of possible larger multipolar errors is unknown since careful magnetic measurements were carried out. We suspect that some additional multipolar fields can be induced due to the crosstalk of the quadrupoles, normal sextupoles and skew sextupoles being very close to each other in the final doublet region. Further experimental tests with and without the octupoles should be carried out in the future to shed light on this matter. Moreover, the strong nonlinear aberrations strengthen the role of the octupole magnets, not only for ultra-low β_y^* optics, but also for the nominal optics with $1\beta_x^*$.

We identify the main reasons for observing larger beam sizes than expected: insufficient orbit control and sensitivity to machine drifts, contribution of wakefields combined with the beam orbit jitter, larger multipolar fields, larger magnet alignment errors, instrumentation errors and stability (especially Shintake monitor and BPMs). All these factors are strongly related as large orbit offsets can be interpreted as larger misalignments causing a stronger effect due to multipolar errors and stronger wakefields contribution. Addressing these issues is recommended for future experiment with low β_y^* optics.

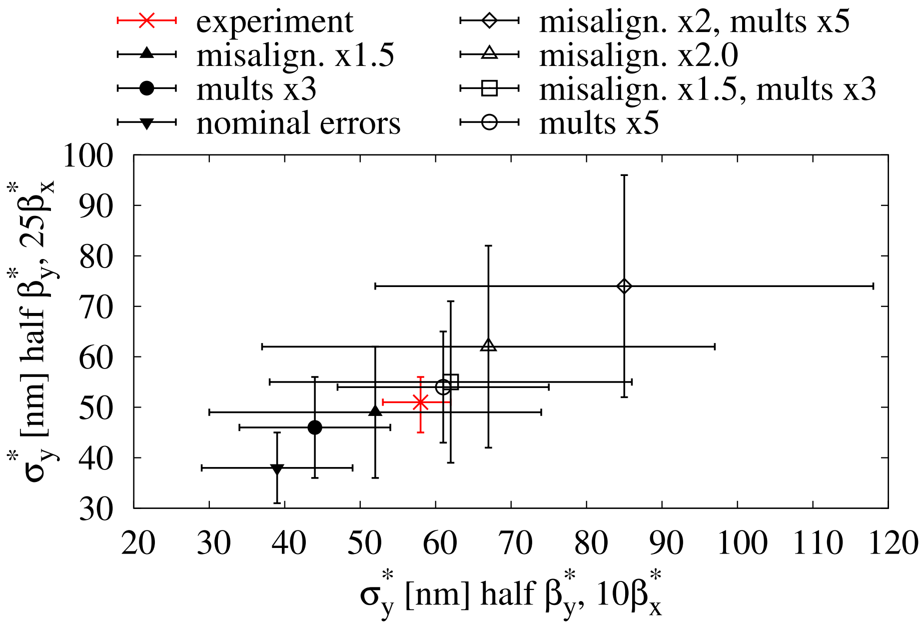

Figure 5.11: The IP beam sizes measured in ATF2 (red) and obtained with simulations without the orbit correction (black) for half β_y^*, $10\beta_x^*$ and half β_y^*, $25\beta_x^*$ optics.

5.4. Conclusions

The half β_y^* optics has been studied at the ATF2 as a first experimental step towards the ultra-low β_y^*. The optics control and implementation was achieved by introducing a new method of beam diagnostics at the IP based on precise beam size measurements and fine, well-controlled changes of the vertical beam waist position. Two complete tuning sessions were performed followed by the beam size measurements. The measured beam sizes were almost a factor three larger than the design values (assuming measured vertical emittance). It was observed that the IP beam size increase coincides with large orbit position jitter in the final focus line. On the other hand, the machine operated with the nominal β_y^*, $10\beta_x^*$ optics is close to reaching the design performance in terms of IP vertical beam size as was demonstrated in early 2016 ATF2 operation [84]. This suggests that the beam size growth due to machine imperfections for lower β_y^* values is much stronger than expected in the design. The realistic errors applied to the machine model are not sufficient to reproduce the experimental results. Simulation results get closer to the experiment for larger machine errors, especially for the following cases: misalign. x1.5; mults x5; misalign. x1.5, mults x3. It is also possible that there are other sources of beam size growth which are not included in the simulations.

Simulations also show that an accurate orbit correction can help in lowering the IP beam size. A large effect of the beam orbit on the IP beam size is observed in the ATF2. Therefore, improving the existing orbit control in the ATF2 might be of crucial importance for the future ultra-low β_y^* study.

Chapter 6

Conclusions

This thesis reports on the conceptual and experimental studies performed towards the implementation of the ultra-low β_y^* optics in the Accelerator Test Facility 2. Lowering the β^* value is of special importance for future linear colliders as it allows us to increase the luminosity and therefore improve the collisions efficiency.

New sets of optics for the ATF2 with β_y^* value decreased by factors 2 (half β_y^*) and 4 (ultra-low β_y^*) have been designed and optimised towards achieving the minimum vertical beam size at the IP which requires an efficient correction of the nonlinear transport aberrations. The two proposed methods for lowering the IP vertical beam size were developed using computer simulations: an increase of the β_x^* value by a factor 10 or an installation of two octupole magnets. Both methods are efficient in decreasing the IP vertical beam sizes close to their limits. The solution with the octupole magnets is preferred as it does not involve the IP horizontal beam size growth. As a result of this study, the installation of two octupole magnets in the ATF2 is scheduled for autumn 2016 in order to support the ultra-low β_y^* experiment.

The effect of the quadrupole fringe fields on the IP vertical beam size in the ATF2 nominal β_y^* and ultra-low β_y^* cases was investigated. The same analysis was also performed for the design optics of CLIC and the ILC. It turns out that the fringe fields are negligible for CLIC and the ILC, but are important for the ATF2 ultra-low β_y^* and require corrections. The proposed correction methods are again either increasing the β_x^* value or installing two octupole magnets.

The IP beam size growth with increasing bunch intensity, mainly due to wakefields, forces us to operate the ATF2 beam at the lowest possible intensity of about 10^9 electrons per bunch (a factor 5 lower than nominal). The contribution of optical aberrations to spot size increase with bunch intensity for the ATF2 nominal β_y^* and ultra-low β_y^* optics have been studied. It was found that the increase of damping ring beam emittance and momentum spread due to

IBS should not prevent one from reaching the design vertical beam size at the IP, even for the nominal beam intensity.

The main result of this thesis concerns the implementation of the half β_y^* optics in the ATF2, performing the IP beam tuning and measurement of the IP beam sizes after the tuning. The optics control was achieved by applying a new method of beam diagnostics at the IP based on precise beam size measurements and fine, well-controlled changes of the vertical beam waist position. Two complete tuning sessions were performed followed by the IP beam size measurements. The measured beam sizes were almost a factor three larger than the design values. Comparison with the nominal β_y^* optics suggests that the beam size growth due to machine imperfections for lower β_y^* values is much stronger than expected in the design. By comparing the experimental results with the tuning simulations it turns out that the realistic errors applied to the machine model are not sufficient to reproduce the experimental results. Simulation results get closer to the experiment for larger machine errors, namely for the alignment errors increased by a factor 1.5, multipolar errors increased by a factor 5, or by simultaneously increasing alignment errors by a factor 1.5 and multipolar errors by a factor 3. Simulations also show that an accurate orbit correction helps in lowering the IP beam size. Larger alignment errors can be explained with the known limitations of the ATF2 orbit correction methods. The source of possible larger multipolar errors is unknown since careful magnetic measurements were carried out. However, it is suspected that some additional multipolar fields can be induced due to the crosstalk of the quadrupoles, normal sextupoles and skew sextupoles being very close to each other in the final doublet region. Moreover, the strong nonlinear aberrations strengthen the role of the octupole magnets, not only for the ultra-low β_y^* optics, but also for the nominal optics with $1\beta_x^*$.

Bibliography

[1] H. K. Quang and P. X. Yem, *Elementary Particles and Their Interactions: Concepts and Phenomena*. Springer, Berlin, 1998. `http://cds.cern.ch/record/369742`.

[2] Graphics taken from: `https://commons.wikimedia.org/wiki/File:Standard_Model_of_Elementary_Particles.svg`.

[3] F. Englert and R. Brout, "Broken symmetry and the mass of gauge vector mesons," *Phys. Rev. Lett.* **13** (Aug, 1964) 321–323. `http://link.aps.org/doi/10.1103/PhysRevLett.13.321`.

[4] P. W. Higgs, "Broken symmetries and the masses of gauge bosons," *Phys. Rev. Lett.* **13** (Oct, 1964) 508–509. `http://link.aps.org/doi/10.1103/PhysRevLett.13.508`.

[5] **ATLAS** Collaboration, G. Aad *et al.*, "Observation of a new particle in the search for the Standard Model Higgs boson with the ATLAS detector at the LHC," *Phys. Lett.* **B716** (2012) 1–29, `arXiv:1207.7214 [hep-ex]`.

[6] **CMS** Collaboration, S. Chatrchyan *et al.*, "Observation of a new boson at a mass of 125 GeV with the CMS experiment at the LHC," *Phys. Lett.* **B716** (2012) 30–61, `arXiv:1207.7235 [hep-ex]`.

[7] K.A. Olive, et al. (Particle Data Group), Chinese Physics C38 (2014) 090001.

[8] P. Bechtle, T. Plehn, and C. Sander, "Supersymmetry," in *The Large Hadron Collider: Harvest of Run 1*, T. Schorner-Sadenius, ed., pp. 421–462. 2015. `arXiv:1506.03091 [hep-ex]`. `https://inspirehep.net/record/1375491/files/arXiv:1506.03091.pdf`.

[9] Standard Model Production Cross section Measurements in the ATLAS experiment `https://atlas.web.cern.ch/Atlas/GROUPS/PHYSICS/CombinedSummaryPlots/SM/index.html` and in the CMS experiment `https://twiki.cern.ch/twiki/bin/view/CMSPublic/PhysicsResultsCombined`.

[10] C. Rovelli, "Zakopane lectures on loop gravity," *PoS* **QGQGS2011** (2011) 003, `arXiv:1102.3660 [gr-qc]`.

[11] G. Bertone, D. Hooper, and J. Silk, “Particle dark matter: Evidence, candidates and constraints,” *Phys. Rept.* **405** (2005) 279–390, `arXiv:hep-ph/0404175 [hep-ph]`.

[12] W. Bernreuther, “CP violation and baryogenesis,” *Lect. Notes Phys.* **591** (2002) 237–293, `arXiv:hep-ph/0205279 [hep-ph]`. [,237(2002)].

[13] M. C. Gonzalez-Garcia, M. Maltoni, and T. Schwetz, “Global Analyses of Neutrino Oscillation Experiments,” *Nucl. Phys.* **B908** (2016) 199–217, `arXiv:1512.06856 [hep-ph]`.

[14] R. Haag, J. T. Lopuszanski, and M. Sohnius, “All Possible Generators of Supersymmetries of the s Matrix,” *Nucl. Phys.* **B88** (1975) 257.

[15] O. S. Bruning, P. Collier, P. Lebrun, S. Myers, R. Ostojic, J. Poole, and P. Proudlock, *LHC Design Report*. CERN, Geneva, 2004. `http://cds.cern.ch/record/782076`.

[16] F. Zimmermann, *Accelerator Physics and Technologies for Linear Collider, Lecture Note on the Beam delivery System*. University of Chicago, Chicago, Illinois, 2002.

[17] M. E. Peskin, “PHYSICS OF (VERY) HIGH-ENERGY e+ e- COLLIDERS,” *Conf. Proc.* **C840822** (1984) 387–410.

[18] E. Marin Lacoma, R. Tomas, and Y. Koubychine, *Design and higher order optimisation of Final Focus Systems for Linear Colliders*. PhD thesis, Barcelona, IEEC, Nov, 2012. `https://cds.cern.ch/record/1504285`. Presented 21 Dec 2012.

[19] **CLICdp, CLIC** Collaboration, M. J. Boland *et al.*, “Updated baseline for a staged Compact Linear Collider,” `arXiv:1608.07537 [physics.acc-ph]`.

[20] **ATLAS, CDF, CMS, D0** Collaboration, “First combination of Tevatron and LHC measurements of the top-quark mass,” `arXiv:1403.4427 [hep-ex]`.

[21] G. Aad *et al.*, “Measurement of the top quark mass in the $t\bar{t} \to$ lepton+jets and $t\bar{t} \to$ dilepton channels using $\sqrt{s} = 7$ TeV ATLAS data,” *Eur. Phys. J.* **C75** no. 7, (2015) 330.

[22] **ATLAS** Collaboration, M. Aaboud *et al.*, “Measurement of the top quark mass in the $t\bar{t} \to$ dilepton channel from $\sqrt{s} = 8$ TeV ATLAS data,” `arXiv:1606.02179 [hep-ex]`.

[23] “Combination of the CMS top-quark mass measurements from Run 1 of the LHC,” 2014. `http://cds.cern.ch/record/1951019`.

[24] V. Khachatryan *et al.*, “Measurement of the top quark mass using proton-proton data at $\sqrt{s}$ = 7 and 8 TeV,” *Phys. Rev.* **D93** no. 7, (2016) 072004.

[25] K. Seidel, F. Simon, M. Tesar, and S. Poss, “Top quark mass measurements at and above threshold at CLIC,” *Eur. Phys. J.* **C73** no. 8, (2013) 2530.

[26] B. Allanach, J. Blaising, K. Desch, J. Ellis, G. Giudice, C. Grefe, S. Kraml, T. Lastovicka, L. Linssen, J. Marschall, S. Martin, A. Muennich, S. Poss, P. Roloff, F. Simon, J. Strube, M. Thomson, and J. Wells, “The physics benchmark processes for the detector performance studies used in CLIC CDR Volume 3,”. `https://cds.cern.ch/record/1463554`.

[27] P. Lebrun, L. Linssen, A. Lucaci-Timoce, D. Schulte, F. Simon, S. Stapnes, N. Toge, H. Weerts, and J. Wells, “The CLIC Programme: Towards a Staged e+e- Linear Collider Exploring the Terascale : CLIC Conceptual Design Report,” `arXiv:1209.2543 [physics.ins-det]`.

[28] E. Courant and H. Snyder, “Theory of the alternating-gradient synchrotron,” *Annals of Physics* **3** no. 1, (1958) 1 – 48. `http://www.sciencedirect.com/science/article/pii/0003491658900125`.

[29] K. L. Brown, “A First and Second Order Matrix Theory for the Design of Beam Transport Systems and Charged Particle Spectrometers,” *Adv. Part. Phys.* **1** (1968) 71–134.

[30] E. Forest, *Beam dynamics: a new attitude and framework*. Phys. Technol. Part. Phot. Beams. Harwood, Sidney, 1998. `https://cds.cern.ch/record/367626`.

[31] A. J. Dragt, *Lie methods for nonlinear dynamics with applications to accelerator physics*. 2016. `www.physics.umd.edu/dsat/dsatliemethods.html`.

[32] R. Tomás, “Nonlinear optimization of beam lines,” *Phys. Rev. ST Accel. Beams* **9** (Aug, 2006) 081001. `http://link.aps.org/doi/10.1103/PhysRevSTAB.9.081001`.

[33] J. Irwin, “The application of lie algebra techniques to beam transport design,” *Nuclear Instruments and Methods in Physics Research Section A: Accelerators, Spectrometers, Detectors and Associated Equipment* **298** no. 1, (1990) 460 – 472. `http://www.sciencedirect.com/science/article/pii/016890029090648P`.

[34] H. Garcia Morales, R. Tomas Garcia, and Y. Kubyshin, *Comparative study of Final Focus Systems for CLIC and other luminosity ehancement studies for future linear colliders*. PhD thesis, Barcelona, Polytechnic U., 2014. `https://cds.cern.ch/record/1982827`. Presented 16 Jan 2015.

[35] A. Chao, “Lie Algebra Techniques for Nonlinear Dynamics.” USPAS lecture notes (2012).

[36] T. Behnke, J. E. Brau, B. Foster, J. Fuster, M. Harrison, J. M. Paterson, M. Peskin, M. Stanitzki, N. Walker, and H. Yamamoto, "The International Linear Collider Technical Design Report - Volume 1: Executive Summary," `arXiv:1306.6327 [physics.acc-ph]`.

[37] M. Aicheler, P. Burrows, M. Draper, T. Garvey, P. Lebrun, K. Peach, N. Phinney, H. Schmickler, D. Schulte, and N. Toge, "A Multi-TeV Linear Collider Based on CLIC Technology: CLIC Conceptual Design Report," Tech. Rep. CERN-2012-007. SLAC-R-985. KEK-Report-2012-1. PSI-12-01. JAI-2012-001, Geneva, 2012. `https://cds.cern.ch/record/1500095`.

[38] F. Stulle, "Ring to main linac transport, discussion on status and cdr preparation." Presentation at the CLIC Beam Physics Meeting, 07.07.2010.

[39] Linear collider collaboration: `http://www.linearcollider.org/images/`.

[40] F. Zimmermann, R. Helm, and J. Irwin, "Optimization of the NLC final focus system,". `https://cds.cern.ch/record/285060`.

[41] T. O. Raubenheimer and F. Zimmermann, "Final-focus systems in linear colliders," *Rev. Mod. Phys.* **72** (Jan, 2000) 95–107. `http://link.aps.org/doi/10.1103/RevModPhys.72.95`.

[42] K. Oide, "Design of optics for the final focus test beam at SLAC,". `https://cds.cern.ch/record/198528`.

[43] P. Raimondi and A. Seryi, "Novel final focus design for future linear colliders," *Phys. Rev. Lett.* **86** (Apr, 2001) 3779–3782. `http://link.aps.org/doi/10.1103/PhysRevLett.86.3779`.

[44] A. Seryi, M. Woodley, and P. Raimondi, "A Recipe for linear collider final focus system design," *Conf. Proc.* **C030512** (2003) 2766.

[45] K. Yokoya and P. Chen, "Beam-beam phenomena in linear colliders," *Lect. Notes Phys.* **400** (1992) 415–445.

[46] O. Blanco, P. Bambade, and R. Tomas, "CLIC 3TeV Beamsize Optimization with Radiation Effects,". `https://cds.cern.ch/record/1588132`.

[47] A. W. Chao and M. Tigner, *Handbook of Accelerator Physics and Engineering*. World Scientific, Singapore, 1999. `https://cds.cern.ch/record/384825`.

[48] K. Oide, "Synchrotron-radiation limit on the focusing of electron beams," *Phys. Rev. Lett.* **61** (Oct, 1988) 1713–1715. `http://link.aps.org/doi/10.1103/PhysRevLett.61.1713`.

[49] O. R. Blanco, R. Tomás, and P. Bambade, “Beam focusing limitation from synchrotron radiation in two dimensions,” *Phys. Rev. Accel. Beams* **19** (Feb, 2016) 021002. `http://link.aps.org/doi/10.1103/PhysRevAccelBeams.19.021002`.

[50] O. Napoly, “The luminosity for beam distributions with error and wakefield effects in linear colliders,”. `https://cds.cern.ch/record/240071`.

[51] J. Barranco García, E. Marín Lacoma, and R. Tomás García, “Luminosity studies in a traveling waist regime in the compact linear collider,” *Phys. Rev. ST Accel. Beams* **16** (Apr, 2013) 041001. `http://link.aps.org/doi/10.1103/PhysRevSTAB.16.041001`.

[52] T. Shintake, H. Hayano, A. Hayakawa, Y. Ozaki, M. Ohashi, K. Yasuda, D. Waltz, S. Wagner, and D. Burke, “Design of laser-Compton spot size monitor,”. `https://cds.cern.ch/record/242239`.

[53] J. Yan, *Precise Measurement of Nanometer Scale Electron Beam Sizes Using Laser Interference by Shintake Monitor*. Ph.D. thesis, 2015.

[54] J. Ellis, “The Physics Prospects for CLIC,” *Balk. Phys. Lett.* **17** (2009) 270–288, `arXiv:0811.1366 [hep-ph]`.

[55] R. Tomás, “Overview of the compact linear collider,” *Phys. Rev. ST Accel. Beams* **13** (Jan, 2010) 014801. `http://link.aps.org/doi/10.1103/PhysRevSTAB.13.014801`.

[56] V. Balakin, V. A. Alexandrov, A. Mikhailichenko, K. Flöttmann, F. Peters, G.-A. Voss, V. Bharadwaj, M. Halling, J. A. Holt, J. Buon, J. Jeanjean, F. LeDiberder, V. Lepeltier, P. Puzo, G. Heimlinger, R. Settles, U. Stierlin, H. Hayano, N. Ishihara, H. Nakayama, K. Oide, T. Shintake, Y. Takeuchi, N. Yamamoto, F. Bulos, D. Burke, R. Field, S. Hartman, R. Helm, J. Irwin, R. Iverson, S. Rokni, G. Roy, W. Spence, P. Tenenbaum, S. R. Wagner, D. Walz, and S. Williams, “Focusing of submicron beams for tev-scale e^+e^- linear colliders,” *Phys. Rev. Lett.* **74** (Mar, 1995) 2479–2482. `http://link.aps.org/doi/10.1103/PhysRevLett.74.2479`.

[57] D. Burke, “Results from the Final Focus Test Beam,”. `http://www.slac.stanford.edu/cgi-wrap/getdoc/slac-pub-6609.pdf`.

[58] **for the CLIC Collaboration** Collaboration, R. Corsini, “Experimental verification of the CLIC two-beam scheme, status and outlook,” *Conf. Proc.* **C1205201** no. CERN-ATS-2012-180. CLIC-Note-962, (May, 2012) TUOBC01. 3 p. `https://cds.cern.ch/record/1464099`.

[59] R. Ruber, V. Ziemann, T. EkelĂśf, A. Palaia, W. Farabolini, and R. Corsini, "The {CTF3} two-beam test stand," *Nuclear Instruments and Methods in Physics Research Section A: Accelerators, Spectrometers, Detectors and Associated Equipment* **729** (2013) 546 – 553. `http://www.sciencedirect.com/science/article/pii/S0168900213010644`.

[60] S. Kawabata, H. Matsumoto, K. Oide, K. I. Takada, S. Takeda, J. Urakawa, and F. Hinode, *ATF Accelerator Test Facility: design and study report.* KEK, Tsukuba, 1995. `https://cds.cern.ch/record/285466`.

[61] KEK: High Energy Accelerator Research Organisation. `http://www.kek.jp/en/`.

[62] **ATF Collaboration** Collaboration, K. Kubo, M. Akemoto, S. Anderson, T. Aoki, S. Araki, K. L. F. Bane, P. Blum, J. Corlett, K. Dobashi, P. Emma, J. Frisch, M. Fukuda, Z. Guo, K. Hasegawa, H. Hayano, T. Higo, A. Higurashi, Y. Honda, T. Iimura, T. Imai, K. Jobe, S. Kamada, P. Karataev, S. Kashiwagi, E. Kim, T. Kobuki, T. Kotseroglou, Y. Kurihara, M. Kuriki, R. Kuroda, S. Kuroda, T. Lee, X. Luo, D. J. McCormick, B. McKee, T. Mimashi, M. Minty, T. Muto, T. Naito, G. Naumenko, J. Nelson, M. N. Nguyen, K. Oide, T. Okugi, T. Omori, T. Oshima, G. Pei, A. Potylitsyn, Q. Qin, T. Raubenheimer, M. Ross, H. Sakai, I. Sakai, F. Schmidt, T. Slaton, H. Smith, S. Smith, T. Smith, T. Suzuki, M. Takano, S. Takeda, N. Terunuma, N. Toge, J. Turner, J. Urakawa, V. Vogel, M. Woodley, J. Yocky, A. Young, and F. Zimmermann, "Extremely Low Vertical-Emittance Beam in the Accelerator Test Facility at KEK," *Phys. Rev. Lett.* **88** (Apr, 2002) 194801. `http://link.aps.org/doi/10.1103/PhysRevLett.88.194801`.

[63] Y. Honda, K. Kubo, S. Anderson, S. Araki, K. Bane, A. Brachmann, J. Frisch, M. Fukuda, K. Hasegawa, H. Hayano, L. Hendrickson, Y. Higashi, T. Higo, K. Hirano, T. Hirose, K. Iida, T. Imai, Y. Inoue, P. Karataev, M. Kuriki, R. Kuroda, S. Kuroda, X. Luo, D. McCormick, M. Matsuda, T. Muto, K. Nakajima, T. Naito, J. Nelson, M. Nomura, A. Ohashi, T. Omori, T. Okugi, M. Ross, H. Sakai, I. Sakai, N. Sasao, S. Smith, T. Suzuki, M. Takano, T. Taniguchi, N. Terunuma, J. Turner, N. Toge, J. Urakawa, V. Vogel, M. Woodley, A. Wolski, I. Yamazaki, Y. Yamazaki, G. Yocky, A. Young, and F. Zimmermann, "Achievement of Ultralow Emittance Beam in the Accelerator Test Facility Damping Ring," *Phys. Rev. Lett.* **92** (Feb, 2004) 054802. `http://link.aps.org/doi/10.1103/PhysRevLett.92.054802`.

[64] **ATF2(KEK) Group** Collaboration, H. Braun, B. Ivanovich-Grishanov, P. V. Logatchev, F. Podgorny, V. I. Telnov, D. Angal-Kalinin, R. Appleby, J. Jones, A. Kalinin, O. Napoly, J. Payet, H. H. Braun, D. Schulte, F. Zimmermann, R. J. Barlow, I. R. Bailey,

L. Jenner, R. Jones, G. Y. Kourevlev, N. Walker, T. Takahasi, J. Gao, L. W. Bin, P. G. Xi, W. J. Qing, N. Delerue, S. Dixit, D. F. Howell, A. Reichold, I. V. Agapov, G. A. Blair, G. Boorman, J. Carter, C. Driouichi, M. T. Price, S. Araki, H. Hayano, Y. Higashi, Y. Honda, K. I. Kanazawa, K. Kubo, T. Kume, M. Kuriki, S. Kuroda, M. Masuzawa, T. Naito, T. Okugi, R. Sugahara, T. Tauchi, N. Terunuma, N. Toge, J. Urakawa, V. Vogel, H. Yamaoka, K. Yokoya, I. Yoshihisa, T. Mihara, P. Bambade, A. Wolski, J. Gronberg, S. Takashi Boogert, A. Lyapin, S. Malton, D. J. Miller, M. Kumada, S. Danagulyan, E. Torrence, C. J. Yuk, H. J. Yun, S. K. Heung, E. S. Kim, K. S. Wan, S. K. In, P. N. Burrows, G. B. Christian, C. Clarke, A. F. Hartin, H. Dabiri-Khah, S. Molloy, K. L. F. Bane, A. Brachmann, T. Himel, T. W. Markiewicz, J. Nelson, Y. Nosochkov, N. Phinney, M. Torino, F. Pivi, T. O. Raubenheimer, M. Ross, R. E. Ruland, A. Seryi, C. M. Spencer, P. G. Tenenbaum, M. Woodley, S. Komamiya, T. Sanuki, and T. Suehara, "ATF2 Proposal: v.1," Tech. Rep. CERN-AB-2005-035. CLIC-Note-636. DESY-05-148. DESY-2005-148. ILC-ASIA-2005-22. JAI-2005-002. KEK-REPORT-2005-2. SLAC-R-771. UT-ICEPP-2005-02, CERN, Geneva, Aug, 2005. `https://cds.cern.ch/record/855957`.

[65] T. Okugi *et al.*, *ICFA Beam Dynamics Newsline, No 61*. `http://icfa-usa.jlab.org/archive/newsletter/icfa_bd_nl_61.pdf`.

[66] H. Sakai, M. Fujisawa, K. Iida, I. Ito, H. Kudo, N. Nakamura, K. Shinoe, T. Tanaka, H. Hayano, M. Kuriki, and T. Muto, "Improvement of Fresnel zone plate beam-profile monitor and application to ultralow emittance beam profile measurements," *Phys. Rev. ST Accel. Beams* **10** (Apr, 2007) 042801. `http://link.aps.org/doi/10.1103/PhysRevSTAB.10.042801`.

[67] J. Alabau-Gonzalvo *et al.*, "The ATF2 Multi-OTR System: Studies and Design Improvements," in *International Beam Instrumentation Conference*. 2012.

[68] Y. I. Kim *et al.*, "Cavity beam position monitor system for the Accelerator Test Facility 2," *Phys. Rev. ST Accel. Beams* **15** (2012) 042801, `arXiv:1301.5561 [physics.acc-ph]`.

[69] **ATF2 Collaboration** Collaboration, G. R. White, R. Ainsworth, T. Akagi, J. Alabau-Gonzalvo, D. Angal-Kalinin, S. Araki, A. Aryshev, S. Bai, P. Bambade, D. R. Bett, G. Blair, C. Blanch, O. Blanco, N. Blaskovic-Kraljevic, B. Bolzon, S. Boogert, P. N. Burrows, G. Christian, L. Corner, M. R. Davis, A. Faus-Golfe, M. Fukuda, J. Gao, H. García-Morales, N. Geffroy, H. Hayano, A. Y. Heo, M. Hildreth, Y. Honda, J. Y. Huang, W. H. Hwang, Y. Iwashita, S. Jang, A. Jeremie, Y. Kamiya, P. Karataev, E. S. Kim, H. S. Kim, S. H. Kim, Y. I. Kim, S. Komamiya, K. Kubo, T. Kume, S. Kuroda,

B. Lam, K. Lekomtsev, S. Liu, A. Lyapin, E. Marin, M. Masuzawa, D. McCormick, T. Naito, J. Nelson, L. J. Nevay, T. Okugi, T. Omori, M. Oroku, H. Park, Y. J. Park, C. Perry, J. Pfingstner, N. Phinney, A. Rawankar, Y. Renier, J. Resta-López, M. Ross, T. Sanuki, D. Schulte, A. Seryi, M. Shevelev, H. Shimizu, J. Snuverink, C. Spencer, T. Suehara, R. Sugahara, T. Takahashi, R. Tanaka, T. Tauchi, N. Terunuma, R. Tomás, J. Urakawa, D. Wang, M. Warden, M. Wendt, A. Wolski, M. Woodley, Y. Yamaguchi, T. Yamanaka, J. Yan, K. Yokoya, and F. Zimmermann, "Experimental Validation of a Novel Compact Focusing Scheme for Future Energy-Frontier Linear Lepton Colliders," *Phys. Rev. Lett.* **112** (Jan, 2014) 034802. `http://link.aps.org/doi/10.1103/PhysRevLett.112.034802`.

[70] E. Marin, R. Tomás, P. Bambade, K. Kubo, T. Okugi, T. Tauchi, N. Terunuma, J. Urakawa, A. Seryi, G. R. White, and M. Woodley, "Design and high order optimization of the Accelerator Test Facility lattices," *Phys. Rev. ST Accel. Beams* **17** (Feb, 2014) 021002. `http://link.aps.org/doi/10.1103/PhysRevSTAB.17.021002`.

[71] M. Patecki and R. Tomás, "Effects of quadrupole fringe fields in final focus systems for linear colliders," *Phys. Rev. ST Accel. Beams* **17** (Oct, 2014) 101002. `http://link.aps.org/doi/10.1103/PhysRevSTAB.17.101002`.

[72] E. Marin, "Specifications of the octupole magnets required for the ATF2 ultra-low beta* lattice," Tech. Rep. SLAC-TN-14-019, 2014.

[73] M. Modena, "Update on 2 Octupoles Procurement for ATF2 Final Focus Systems." Talk at 18th ATF2 Project meeting, 2015.

[74] T. Okugi, S. Araki, P. Bambade, K. Kubo, S. Kurado, M. Masuzawa, E. Marin, T. Naito, T. Tauchi, N. Terunuma, R. Tomas, J. Urakawa, G. White, and M. Woodley, "Linear and second order optics corrections for the KEK Accelerator Test Facility final focus beam line," *Phys. Rev. ST Accel. Beams* **17** (Feb, 2014) 023501. `http://link.aps.org/doi/10.1103/PhysRevSTAB.17.023501`.

[75] H. Hayano, "Wire scanners for small emittance beam measurement in ATF," *eConf* **C000821** (2000) MOC01, `arXiv:physics/0008084 [physics.acc-ph]`. [,146(2000)].

[76] H. Grote, F. Schmidt, L. Deniau, and G. Roy, *The MAD-X Program (Methodical Accelerator Design) Userâs Reference Manual*. `http://mad.web.cern.ch/`.

[77] M. Masuzawa, "Qea magnet measurements at kek and comparison with ihep results." Talk at 11th ATF2 Project meeting, 2011.

[78] S. Bai, P. Bambade, D. Wang, J. Gao, M. Woodley, and M. Masuzawa, “Mitigating the effects of higher order multipole fields in the magnets of the Accelerator Test Facility 2 at KEK,” *Chinese Physics C* **36** (2012) 756–760. `http://hal.in2p3.fr/in2p3-00732385`.

[79] F. Schmidt, E. Forest, and E. McIntosh, “Introduction to the polymorphic tracking code: Fibre bundles, polymorphic Taylor types and "Exact tracking",” Tech. Rep. CERN-SL-2002-044-AP., CERN, Geneva, Jul, 2002. `http://cds.cern.ch/record/573082`.

[80] D. Martinez, A. Rosam, R. Tomás, and R. De Maria, “Mapclass2: a code to aid the optimisation of lattice design,” Tech. Rep. CERN-ATS-Note-2012-087 TECH, Nov, 2012. `https://cds.cern.ch/record/1491228`.

[81] M. Patecki, D. Bett, F. Plassard, R. Tomas, K. Kubo, S. Kuroda, T. Naito, T. Okugi, T. Tauchi, and N. Terunuma, “Progress in ultra-low beta* study at ATF2,” in *International Particle Accelerators Conference*. 2016. `http://accelconf.web.cern.ch/AccelConf/IPAC2015/papers/mobc1.pdf`.

[82] K. Kubo, “Wakefield issues.” Talk at the European Linear Collider Workshop, 2016.

[83] M. Patecki, R. Tomas, F. Zimmermann, K. Kubo, S. Kuroda, T. Naito, T. Okugi, T. Tauchi, and N. Terunuma, “Contribution of Optical Aberrations to Spot-size Increase with Bunch Intensity at ATF2,” in *International Particle Accelerators Conference*. 2015. `http://accelconf.web.cern.ch/AccelConf/IPAC2015/papers/mopje065.pdf`.

[84] T. Okugi, “Small beam status.” Talk at the European Linear Collider Workshop, 2016.

[85] S. Kelly *et al.*, “Study of the Impact of Fringe Fields of the Large Aperture Triplets on the Linear Optics of the HL-LHC,” in *International Particle Accelerators Conference*. 2013. `http://accelconf.web.cern.ch/AccelConf/IPAC2013/papers/wepea059.pdf`.

[86] H. A. Enge, “Effect of Extended Fringing Fields on IonâFocusing Properties of Deflecting Magnets,” *Review of Scientific Instruments* **35** no. 3, (1964) .

[87] M. Modena, “CLIC QD0 ’Short Prototype’ Status,” in *International Workshop on Future Linear Colliders (LCWS11) Granada, Spain, September 26-30, 2011*. 2012. `arXiv:1202.5952 [physics.acc-ph]`. `https://inspirehep.net/record/1090840/files/arXiv:1202.5952.pdf`.

[88] HiLumi LHC Work Package 3, `http://espace.cern.ch/HiLumi/WP3/SitePages/MQXF.aspx`.

[89] J. Irwin and C.-x. Wang, "Explicit Soft Fringe Maps of a Quadrupole," in *Particle Accelerator Conference, Dallas*. 1995. `http://accelconf.web.cern.ch/AccelConf/p95/ARTICLES/MPC/MPC31.PDF`.

[90] B. D. Muratori, J. K. Jones, and A. Wolski, "Analytical expressions for fringe fields in multipole magnets," *Phys. Rev. ST Accel. Beams* **18** no. 6, (2015) 064001, `arXiv:1404.1762 [physics.acc-ph]`.

[91] K. Oide and H. Koiso, "Dynamic aperture of electron storage rings with noninterleaved sextupoles," *Phys. Rev.* **E47** (1993) 2010–2018.

[92] A. Wolski, J. Gratus, and R. W. Tucker, "Symplectic integrator for s-dependent static magnetic fields based on mixed-variable generating functions," *JINST* **7** (2012) P04013, `arXiv:1206.6654 [physics.acc-ph]`.

[93] M. Venturini and A. J. Dragt, "Accurate computation of transfer maps from magnetic field data," *Nuclear Instruments and Methods in Physics Research Section A: Accelerators, Spectrometers, Detectors and Associated Equipment* **427** no. 1â2, (1999) 387 – 392. `http://www.sciencedirect.com/science/article/pii/S0168900298015186`.

[94] R. Baartman, "Intrinsic Third Order Aberrations in Electrostatic and Magnetic Quadrupoles," `arXiv:1508.00058 [physics.acc-ph]`.

[95] G. H. Hoffstätter and M. Berz, "Symplectic scaling of transfer maps including fringe fields," *Phys. Rev. E* **54** (Nov, 1996) 5664–5672. `http://link.aps.org/doi/10.1103/PhysRevE.54.5664`.

[96] G. White and D. McCormick, "Multi-OTR Status." Presentation at the ATF2 Operation Meeting, 31.10.2014.

[97] Atf2 logbook, `http://atf.kek.jp/twiki/bin/view/ATFlogbook/Log20141117s`.

[98] J. Snuverink, S. Boogert, A. Lyapin, and K. Kubo, "Review and updated studies on Wakefield measurements." Talk at the ATF2 Project Meeting, 2015.

[99] **ATF2** Collaboration, K. Kubo, "Towards an International Linear Collider: Experiments at ATF2," in *Proceedings, 5th International Particle Accelerator Conference (IPAC 2014): Dresden, Germany, June 15-20, 2014*, p. WEZA01. 2014. `http://jacow.org/IPAC2014/papers/weza01.pdf`.

[100] S. Kuroda, "ATF2 for final focus test beam for future linear colliders." Talk at 37th International Conference on High Energy Physics, 2014.

[101] Strategic Accelerator Design, `http://acc-physics.kek.jp/SAD/`.

[102] M. G. Minty and F. Zimmermann, *Measurement and control of charged particle beams*. Particle acceleration and detection. Springer, Berlin, 2003. `https://cds.cern.ch/record/629879`.

[103] T. Okugi, private communication.

[104] M. Patecki, D. Bett, E. Marin, F. Plassard, R. Tomás, K. Kubo, S. Kuroda, T. Naito, T. Okugi, T. Tauchi, and N. Terunuma, "Probing half β_y^* optics in the Accelerator Test Facility 2," *Phys. Rev. Accel. Beams* **19** (Oct, 2016) 101001. `http://link.aps.org/doi/10.1103/PhysRevAccelBeams.19.101001`.

[105] M. Patecki, G. White, and D. McCormick, "Multi-OTR study." Presentation at the ATF2 Operation Meeting, 22.05.2015.

[106] M. Patecki, G. White, D. McCormick, and F. N., "Multi-OTR study." Presentation at the ATF2 Operation Meeting, 29.05.2015.

[107] M. A. Pons *et al.*, "Study of Abnormal Emittance Growth in ATF Extraction Line," Tech. Rep. SLAC-PUB-14684.

[108] S. Bai, A. Aryshev, P. Bambade, D. Mc Cormick, B. Bolzon, J. Gao, T. Tauchi, and F. Zhou, "First beam waist measurements in the final focus beam line at the KEK Accelerator Test Facility," *Phys. Rev. ST Accel. Beams* **13** (Sep, 2010) 092804. `http://link.aps.org/doi/10.1103/PhysRevSTAB.13.092804`.

[109] T. Okugi, "IP beam size tuning in these 2 weeks.." Presentation at the ATF2 Operation Meeting, 05.02.2016.

[110] M. Patecki, "Summary of low beta* experiment in this week." Presentation at the ATF2 Operation Meeting, 26.02.2016.

List of Figures

List of Tables